technische universität
dortmund

Structural Investigations of Biomolecules under Extreme Conditions

---

Dissertation
zur Erlangung des akademischen Grades
Doktor der Naturwissenschaften
(Dr. rer. nat.)

vorgelegt von
M. Sc. Melanie Berghaus
aus Dortmund

eingereicht bei der
Fakultät für Chemie und Chemische Biologie
der Technischen Universität Dortmund

Dortmund
2017

Die vorliegende Arbeit wurde in der Zeit von Juli 2013 bis Dezember 2016 am Lehrstuhl für Physikalische Chemie I (Biophysikalische Chemie) der Technischen Universität Dortmund unter Betreuung von Herrn Prof. Dr. R. Winter angefertigt.

Dissertation eingereicht am: 04.07.2017
Tag der mündlichen Prüfung: 01.09.2017
Amtierender Dekan: Prof. Dr. R. Winter

Prüfungskommission:
Vorsitzender: Prof. Dr. D. Summerer
Erstgutachter: Prof. Dr. R. Winter
Zweitgutachter: Prof. Dr. H. Rehage

When you go through deep waters,

I will be with you.

Isaiah 43:2

Table of contents

Abstract

Scattering methods like small-angle X-ray scattering and X-ray reflectivity enable to perform *in situ* studies on biomolecules under various conditions of temperature and pressure. These methods are employed in this work to shed light on the changes of size and shape as well as on the interactions between biomolecules under extreme conditions. Most of these aim to simulate conditions of temperature and pressures encountered in hydrothermal vents in the deep sea, where life might have evolved. This work includes many examples from all classes of biomolecules, lipids, nucleic acids as well as peptides and proteins, ranging from fairly simple to very complex systems.

The first class investigated was lipids. In an aqueous mixture of prebiotic lipids, temperature and pressure were found to foster the formation of vesicles from micelles, which might have served as envelopes for protocells. Further, the effect of pressure on a disordered bicontinuous microemulsion forming a lamellar phase in proximity to an interface was investigated. The experiments suggest that with rising pressure the bicontinuous and the lamellar phase become more compressed and ordered, but even pressures of 400 MPa were not able to induce a phase transition between the two phases.

The investigations proceeded with nucleotides and nucleic acids, starting with the self-assembly of single nucleotides. It was found that the self-assembly of guanosine monophosphate sodium salt under pressure can be drastically altered by the addition of stabilizing and destabilizing cosolutes, such as divalent ions. Next, a small RNA hairpin was explored; it was found that attached fluorophores can interact with the bases at elevated temperatures. Further studies on RNA molecules, like phenylalanyl transfer RNA, showed that these molecules are surprisingly stable even at very high pressures.

Finally, the effect of temperature and pressure on peptides and proteins was explored, covering a short peptide, a protein and a complex network of proteins. First, the effect of cosolutes on the inverse temperature transition of an elastin-like peptide was investigated. This peptide showed an elongation with rising temperature. In addition, three different variants of the phosphoprotein 32 were analyzed in dependence of temperature and pressure. The measurements revealed that mutations in the capping-motives drastically change the stability and cooperativity of

pressure-induced unfolding of its leucine-rich repeat motif. For the network, measurements showed that actin bundles cross-linked by the fascin establish significantly higher pressure, but lower temperature stability than actin bundles cross-linked by divalent ions. Thus, this native binding protein might suit better the needs of organism living in the deep sea. Taken together, this work provides many new and interesting insights on how life might have evolved under extreme conditions of temperature and pressure and how organisms adapted to the latter.

Kurzfassung

Streumethoden wie Röntgenkleinwinkelstreuung und Röntgenreflektometrie ermöglichen es, *in situ*-Studien an Biomolekülen bei verschiedenen Temperaturen und Drücken durchzuführen. Diese Methoden wurden in dieser Arbeit verwendet, um tiefere Einblicke in die Veränderung der Form und Größe sowie der Wechselwirkungen zwischen Biomoleküle unter extremen Bedingungen zu gewinnen. Die meisten Untersuchungsbedingungen haben zum Ziel, die Bedingungen von Temperatur und Druck in heißen Quellen in der Tiefsee nachzuahmen, wo das Leben entstanden sein könnte. Diese Arbeit beinhaltet viele Beispiele aus allen Klassen von Biomolekülen, Lipide, Nukleinsäuren sowie Peptide und Proteine, die von relativ einfachen zu sehr komplexen Systemen reichen.

Die erste Klasse von Biomolekülen, die untersucht wurde, sind die Lipide. Es wurde herausgefunden, dass hohe Temperaturen und Drücke in einer wässrigen Mischung aus präbiotischen Lipiden die Bildung von Vesikeln aus Mizellen fördern, die als Hülle für Protozellen gedient haben könnten. Ferner wurde die Wirkung von Druck auf eine ungeordnet bikontinuierliche Mikroemulsion untersucht, die in der Nähe von Grenzflächen eine lamellare Phase bildet. Die Experimente zeigen, dass die bikontinuierliche und die lamellare Phase mit steigendem Druck komprimiert und geordnet werden, aber selbst Drücke von 400 MPa nicht ausreichen, um einen Übergang zwischen den zwei Phasen zu induzieren.

Die Untersuchungen gingen mit Nukleotiden und Nukleinsäuren weiter, beginnend mit der Selbstorganisation einzelner Nukleotide. Wie gezeigt wurde, haben Kosolventien einen starken Einfluss auf die Selbstorganisation von Guanosinmonophosphat-Natriumsalz unter Druck. Als nächstes wurde eine kleine Haarnadel-RNA untersucht; es wurde herausgefunden, dass angebrachte Fluorophore bei erhöhten Temperaturen mit den Nucleobasen in Wechselwirkung treten können, was die Temperatur- und Druckstabilität des Moleküls stark beeinflusst. Weitere Studien an größeren RNA-Molekülen, wie der tRNA von Phenylalanin, zeigten eine überraschend hohe Stabilität dieser Moleküle, selbst bei sehr hohen Drücken.

Schließlich wurden die Auswirkungen von Temperatur und Druck auf Peptide und Proteine erforscht; die Untersuchungen umfassen ein kurzes Peptid, ein Protein und ein komplexes Netzwerk von Proteinen. Zuerst wurde die Wirkung von stabilisierenden und destabilisierenden Kosolventien auf den inversen

Temperaturübergang eines Elastin-ähnliches Peptids untersucht. In diesen Untersuchungen zeigte das Peptid eine Verlängerung seiner Form mit steigender Temperatur. Darüber hinaus wurden drei unterschiedliche Varianten des Phosphoprotein 32 in Abhängigkeit von Temperatur und Druck untersucht. Die Messungen ergaben, dass Mutationen in den Capping-Motiven drastisch die Stabilität und Kooperativität bei der Druck-induzierten Entfaltung seines Leucine-rich-repeat Motivs verändern. Schließlich zeigten Messungen, dass Fascin-vernetzte Aktinbündel eine deutlich höhere Druckstabilität, aber geringere Temperaturstabilität haben als Aktinbündel, die durch zweiwertige Magnesium-Ionen vernetzt wurden. Somit erfüllt dieses native Bindungsprotein besser die Anforderungen von Organismen, die in der Tiefsee leben. Zusammengenommen bietet diese Arbeit viele neue und interessante Einblicke, wie das Leben unter extremen Bedingungen von Temperatur und Druck entstanden sein könnte und wie Organismen sich daran angepasst haben.

1 Introduction

Modern scattering methods allow for *in situ* structural investigations of various biomolecules. Two of these methods are small-angle X-ray scattering (SAXS), for measurements in solution, and X-ray reflectivity (XRR) to study the behavior of systems in close proximity to an interface. These scattering methods are the fundamental basis of the work presented here and will be introduced in Chapter 2. Both methods are basically non-destructive and do not require crystallization or labeling of the molecules of interest. In addition, these measurements can be performed at various temperatures and, using Synchrotron radiation, at pressures up to 400 MPa. Stabilizing and destabilizing cosolutes can be added to mimic a cellular environment and investigate their effect on the temperature and pressure stability of the biomolecules.

The motivation to perform such studies and the importance of high pressure habitats, as well as how modern cells adapted to these conditions will be highlighted in Chapter 3. After a general introduction in Subchapter 3.1, the effect of pressure on the three main classes of biomolecules, lipids (Subchapter 3.2), nucleic acids (Subchapter 3.3) and proteins (Subchapter 3.4), will be discussed and the molecules under investigation in this work will be introduced.

Deep sea habitats with extreme conditions of temperature and pressure are also proposed to be the cradle of life.[1] In the evolution of the first protocells, the compartmentalization by lipid envelopes was an important step. Lipids are the most pressure sensitive class of biomolecules.[2] In Chapter 4 of this thesis, the investigations on two different lipid systems are presented. In the first Subchapter 4.1, the effect of temperature and pressure on the micelle-vesicle equilibrium of prebiotic lipids (decanoic acid and decanol) is analyzed. Such vesicles might have been precursors to modern cell membranes. SAXS was applied to estimate the size distribution of the species present in the solution. Besides gaining information about a size distribution within a system, scattering methods can also be used to analyze the different lyotropic phases occurring in aqueous lipid systems by diffraction. Contemporary cell membranes are composed of a high variety of different lipids. Thus, they form disordered lyotropic phases, whose parameters can be tuned by temperature and pressure. Interfaces present within cells might have an effect on the transitions between these phases. To gain a better understanding of this effect, a

microemulsion forming a disordered bicontinuous bulk phase and a lamellar phase in proximity to an interface was chosen as a model system. The influence of pressure on the two coexisting lyotropic phases of the microemulsion was analyzed using SAXS and XRR, respectively (Subchapter 4.2).

Besides the first prebiotic lipids, nucleotides and subsequently nucleic acids might have been present in the primordial soup. This class of biomolecules is investigated in Chapter 5. First, the self assembly of a single nucleotide, guanosine mono phosphate, under pressure in the absence and presence of various cosolutes is investigated using SAXS (Subchapter 5.1). In Subchapter 5.2, a short ribonucleic acid forming a common hairpin motif, the small RNA hairpin, is investigated. The RNA world hypothesis[3] states, that RNA might have fulfilled two functions, genetic storage as well as enzymatic reactions. The discovery of ribozymes greatly supported this hypothesis. The behavior of such a ribozyme under high hydrostatic pressures is investigated in Subhapter 5.3. Ribozymes are regarded as precursors to modern enzymes. Thus, they link the RNA and the protein world in evolution. In contemporary cells, the link between RNA and proteins is transfer RNA (tRNA). The effect of pressure on phenylalanine tRNA, as an example of a modern RNA molecule, is analyzed in Subhapter 5.4.

Peptides and proteins are possibly the youngest class of biomolecules. The last chapter of this work, Chapter 6, shows how SAXS can be applied to learn more about their behavior under extreme conditions. The chapter starts with investigations of a short peptide, the so-called elastin-like peptide. The influence of different cosolutes on its temperature stability is analyzed (Subchapter 6.1). In the second part (Subchapter 6.2), pressure is used as a trigger in order to understand how flanking motives of modern leucine-rich repeat proteins influence their stability. SAXS measurements were performed on the wildtype phosphoprotein 32 as well as on two variants with destabilizing mutations in the flanking motives. Finally, the effect of temperature and pressure on a complex network of proteins is investigated using X-ray diffraction. The stability of two different types of actin-bundels was investigated. Bundling was induced by divalent ions and proteins as crosslinkers between the filaments (Subchapter 6.3).

2 Scattering methods

The scope of this chapter is to introduce the theory of the scattering methods relevant to this thesis. It is supposed to provide enough background information to understand the experiments of this thesis and their evaluation without further reading. More detailed reviews of the scattering methods can be found elsewhere.[4–15] After illustrating the theory of these methods, the details of the experimental setups and the X-ray sources where the measurements were performed are described.

2.1 Small-angle X-ray scattering

2.1.1 Introduction

Small-angle X-ray scattering is an increasingly used method which allows to analyze the structure and interactions of (biological) macromolecules in solution. The typical size range is 1-100 nm. One of the greatest advantages of this method is that biomolecules can be studied in their natural environment, even those which cannot be crystallized. At the same time, it also allows to study their response to different stimuli, like the addition of cosolvents or the application of different temperatures and pressures. Modifications of the biomolecules, like labeling, are not required.

Despite the lack of atomic resolution, modern computational methods for shape reconstruction allow to gain detailed information of the size and shape of proteins and nucleic acids under different conditions.[16] In contrast to NMR, SAXS is not restricted to molecules with a weight of a few kDa.[10,17] However, the combination of these two methods can be very fruitful, since SAXS can provide the overall changes in the conformation of a biomolecule, while NMR can resolve their underlying origin in atomic detail. [18] In a SAXS experiment, the scattered intensity, I, is recorded in dependence of the scattering angle 2θ. The geometry of such an experiment is displayed in Figure 2-1.

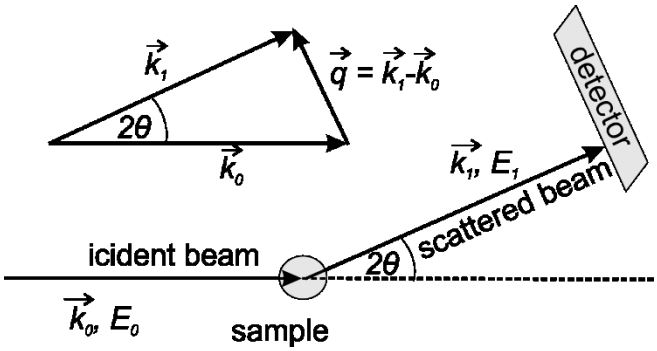

Figure 2-1. Geometry of a scattering experiment.[4]

An incident beam with the wave vector $\vec{k}_0$ and the energy E_0 hits the sample. Upon this, the scattered beam with the wave vector $\vec{k}_1$ and the energy E_1 is detected in dependence of the scattering angle 2θ. Thereby, the length of a wave vector $\vec{k}$ depends on its wavelength λ with $|\vec{k}| = 2\pi/\lambda$. Using the length of the wave vector transfer, q, instead of the scattering angle 2θ allows easy comparability of intensity curves recorded using different wavelengths. Under the assumption that the scattering process is elastic, i.e. $\Delta E = 0$ and $|\vec{k}_0|$ = $|\vec{k}_1|$, the length of the wave vector transfer can be described as

$$q = |\vec{q}| = 2\,|\vec{k}_0| \sin\theta = \frac{4\pi}{\lambda}\sin\theta. \qquad (2.1)$$

In ordered samples it can be more convenient to use $s = q/2\pi$ instead of q, because its reciprocal value directly provides the distance between lattice planes.[4]

The following parameters can be derived directly from the scattering curve: The radius of gyration, R_g, the maximum dimension, D_{max}, the overall compactness (Kratky-plots), the volume and surface structure. Indirect Fourier transformation (IFT) allows to gain more detailed information about the shape of a molecule by calculating pair distance distribution functions, $P(r)$. Modern computational methods allow to model 3D envelopes of the macromolecules to resolve their size and shape in more detail.

X-rays are scattered on the electronic shells of atoms. The electric component of the incident wave (photon) accelerates the negatively charged electrons to oscillate. Thus, a dipole is induced for each electron in the scattering object, emitting radiation of the same frequency as the incident radiation (Thomson-Scattering). The partial

waves of all electrons are summed up in order to calculate the scattering amplitude of a particle, $A(\vec{q})$:

$$A(\vec{q}) = \int_V \rho(\vec{r})\, \mathrm{e}^{\mathrm{i}\vec{q}\vec{r}}\, \mathrm{d}\vec{r} \tag{2.2}$$

Due to the high number of electrons and the fact that they cannot be exactly localized, the concept of electron density, $\rho(\vec{r})$, which is the number of electrons given in the volume element $\mathrm{d}\vec{r}$, is introduced.[4,6] The intensity, $I(q)$, which is detected in the scattering experiment, is then given as the mean square of the amplitude averaged over all orientations of the particle:

$$I(\vec{q}) = \langle |A(\vec{q})|^2 \rangle = \left\langle \left| \int_V \rho(\vec{r})\, \mathrm{e}^{\mathrm{i}\vec{q}\vec{r}}\, \mathrm{d}\vec{r} \right|^2 \right\rangle \tag{2.3}$$

2.1.2 Scattering from diluted solutions

In highly diluted solutions of monodisperse macromolecular particles, the latter can be regarded as isolated. Therefore, no interference between the partial waves originating from different particles can be observed. Furthermore, the particles are oriented in all directions due to the Brownian motion. Hence, the observed scattering pattern is representative for a single particle. [4] Since the distance between atoms within a particle is much smaller than the distance between particles, the electron density can be regarded as homogenously distributed within a particle. This is true for most of the biomolecules.[17]

Using this assumption that the electron density is independent of the location $\vec{r}$ within the particle, its electron density can be written as ρ_s. Including the surrounding solvent with the electron density ρ_0, the scattering of N_p particles in a solution can be calculated as following[4]:

$$I(q) = N_p(\rho_s - \rho_0)^2 \left\langle \left| \int_{V_p} \mathrm{e}^{\mathrm{i}\vec{q}\vec{r}}\, \mathrm{d}\vec{r} \right|^2 \right\rangle . \tag{2.4}$$

Defining the contrast $K = V_p\ (\rho_s - \rho_0)$, in which V_p is the volume of the particle, the form factor $F(\vec{q})$,

$$F(\vec{q}) = \frac{1}{V_p}\int \mathrm{e}^{i\vec{Q}\vec{r}}\mathrm{d}\vec{r} \tag{2.5}$$

only depends on the geometry of the particle, and the observed intensity becomes

$$I(q) = N_P K^2\langle|F(\vec{q})|^2\rangle = N_P K^2\langle P(\vec{q})\rangle = N_P K^2 P(q). \tag{2.6}$$

$P(q)$ is referred to as intraparticular structure factor and is equal to the form factor averaged over all orientations of the particle, i.e. $P(\vec{q}) = |F(\vec{q})|^2$. This averaging is performed by using the following relation introduced by Debye,[19]

$$\langle \mathrm{e}^{\mathrm{i}\vec{q}\vec{r}}\rangle = \frac{\sin(qr)}{qr}\,. \tag{2.7}$$

This averaging over all orientations allows calculating the form factors and thus the intraparticular structure factors of particles with different geometries, for example of a sphere or a cylinder.

Porod's law

For homogenous, smooth particles of any shape, the scattering intensity decays at large scattering angles in an asymptotic way proportional to q^{-4}. According to Porod,[20] the scattering factor $P(q)$ can in this case be approximated as

$$P(q) = \frac{2\pi A_\mathrm{p}}{V_\mathrm{p}^2} q^{-4} \tag{2.8}$$

with A_p as the surface of the particle and V_p its volume. Extrapolation to $q \to 0$ allows the calculation of the Porod volume

$$V_\mathrm{p} = \frac{2\pi^2 I^2(0)}{\int_0^\infty I(q) q^2 \mathrm{d}q}\,. \tag{2.9}$$

In this equation, $I(0)$ is the intensity at $q = 0$.

The Guinier approximation

The Guinier approximation[9,21] allows to calculate the radius of gyration, R_g, a measure for the overall size of the scattering macromolecule. R_g is defined as the average of square center-of-mass distances in the molecule:

$$R_{\mathrm{g}} = \frac{\int r^2 \rho(\vec{r}) \mathrm{d}\vec{r}}{\int \rho(\vec{r}) \mathrm{d}\vec{r}} \approx \frac{1}{V_p} \int r^2 \mathrm{d}\vec{r} \tag{2.10}$$

If a protein denatures, the overall size usually increases. Plotting R_{g} as a function of temperature or pressure usually results in a sigmoidal curve, whose turning point gives the denaturation point of the protein. The approximation relies on a small section of the scattering curve at low angles, only. If the molecules are monodisperse and there are no interactions between them, this section can be approached as

$$\begin{aligned} I(q) = I(0)\left[1 - \frac{1}{3} q^2 R_{\mathrm{g}}^2\right] \approx I(0) \mathrm{e}^{-q^2 R_{\mathrm{g}}^2/3} \\ \Rightarrow \ln I(q) = \ln I(0) - q^2 R_{\mathrm{g}}^2/3 \end{aligned} \tag{2.11}$$

For such a system, plotting the natural logarithm of the scattering intensity against q^2, the so-called Guinier-plot, yields a linear curve with the slope $-R_{\mathrm{g}}^2/3$. Thus, the linearity of the Guinier-Plot is a good indication for the monodispersity and the absence of interactions between the macromolecules. In this case, the radius of gyration can be derived from the slope in the linear Guinier region.

Another method to determine the radius of gyration is from distance distribution functions, $P(r)$, which will be discussed later in this chapter. The R_{g} values derived from these functions are usually more reliable, since this analysis is based on the whole scattering curve and less affected by heterodispersity and interactions between the molecules, and can also be applied if low angles cannot be resolved with sufficient accuracy. However, the Guinier approximation is an important and easy to apply method to determine the radius of gyration. In addition, it provides starting parameters for the calculation of $P(r)$.

The Kratky plot

Another plot, which can be calculated directly from the scattering curve, is the so-called Kratky plot.[6,10] It is obtained by plotting $I(q) * q^2$as a function of q and provides an excellent tool for evaluating the folding of proteins and RNA. For folded domains, the Kratky plot has a bell-shaped peak, because the scattering curve follows Porod's law ($I(q) \propto q^{-4}$, equation (2.8)).The position of the peak provides some information about the overall size.[10] If the protein unfolds and becomes a random-coil, the scattering curve decays with $I(q) \propto q^{-2}$ at high q-values. Thus, the Kratky plot reveals a plateau instead of a peak. The transformation from a peak to a plateau

allows to follow the changes in the folding or compactness of a polymeric molecule as a function of temperature, pressure or cosolutes concentration.

The autocorrelation and the pair distance distribution function

The autocorrelation function, $\gamma(r)$, of the electron density, $\rho(\vec{r})$, was defined by Debye and Bueche[22] and is the direct representation of the spatial information obtained from the scattered intensity in real space. It gives the probability of finding an electron in the distance between r and $r + \mathrm{d}r$ from a reference electron inside the volume V_p of a homogenous particle.

The pair distance distribution function, $P(r)$, is the spherically averaged auto-correlation function and gives a histogram of the distances r between every pair of electrons within a particle:

$$P(r) = r^2\gamma(r) = \frac{r^2}{(2\pi)^3}\int_0^\infty I(q)\frac{\sin(qr)}{qr}\frac{r^2}{(2\pi)^3}\,4\pi q^2\mathrm{d}q \tag{2.12}$$

This function provides information about the shape of a particle. The intercept of the curve $P(r)$ with the r-axis is the maximum distance within the particle, D_max. As already mentioned, this distance distribution function provides another method to calculate the radius of gyration, R_g:

$$R_\mathrm{g}^2 = \frac{\int_0^\infty r^2P(r)\,\mathrm{d}r}{2\int_0^\infty P(r)\,\mathrm{d}r} \tag{2.13}$$

Practically, the intensity $I(q)$ can not be recorded from $q = 0$ until $q = \infty$. Therefore, the distance distribution function is parameterized by a linear combination of orthogonal functions. The scattering intensity is then calculated as

$$I_\mathrm{theo}(q) = \int_0^{D_\mathrm{max}} P_\mathrm{theo}(r)\frac{\sin(qr)}{qr}\,4\pi\,\mathrm{d}r \tag{2.14}$$

$P_\mathrm{theo}(r)$ is varied until $I_\mathrm{theo}(q)$ matches the experimentally determined data. In this work, the software GNOM by Svergun[23] is used to calculate the distance distribution functions via indirect Fourier transformation.

Shape-reconstruction by modeling

Besides the distance distribution function, which gives only a rough idea of the molecule's shape, modern computational methods allow to generate a low-resolution three-dimensional envelope of the molecule from a scattering curve. Since the 1990s, the most common method used is bead-modeling.[24] Models presented in this thesis were calculated by the bead-modeling program DAMMIN[25] or GASBOR[26], which is an optimized version from the same author for proteins. The algorithm of DAMMIN involves the simulated annealing of numerous small beads (dummy atoms). They can be regarded as point scatterers and thus be used to fit the experimentally determined scattering curve.[27] This reduces the problem of finding the according structure to a multidimensional minimization problem, which can be solved using Monte Carlo methods. Physical constrains like a homogenous distribution of the beads in the inner of the molecule and a compactness criterion further decrease the amount of possible solutions. GASBOR uses a similar algorithm, but uses a chain-like ensemble of dummy residues representing the amino-acid chain with the peptide backbone of a protein.

Due to the loss of the information about the orientation in the observed scattering pattern, the reconstruction of a 3-D envelope from a 1-D scattering profile is not unique. This loss of information is also referred to as phase problem. Two different shapes can still result in the same observed scattering intensity. To deal with this problem, one normally performs several runs and superimposes the resulting structures. Further, previously known information about the symmetry or a known 3D structure from NMR experiments or crystallography can significantly improve the solution.

2.1.3 Scattering from concentrated solutions

The interparticular structure factor

If scattering macromolecules or particles are present at higher concentrations, they can no longer be regarded as isolated from each other and their interactions have to be taken into consideration. As long as the interaction does not introduce a certain orientation of the particles, the scattering intensity can be calculated as

$$I(q) = N_P K^2 P(q)\, S(q). \tag{2.15}$$

$S(q)$ is the interparticular structure factor defined as

$$S(q) = \frac{1}{N_P} \left\langle \sum_{n}^{N_P} \sum_{m}^{N_P} e^{i\vec{q}(\vec{r}_m - \vec{r}_n)} \right\rangle \tag{2.16}$$

Application of suitable models allows to calculate the interaction potential, $V(r)$, between the particles, since the distance $\vec{r}_{mn} = \vec{r}_m - \vec{r}_n$ depends on their interaction. For this, the intraparticlular structure factor, $P(q)$, needs to be known from measurements in diluted solutions. In analogy to the already discussed distance distribution function, $P(r)$, derived from $P(q)$, a realspace distribution of the interacting particles can be derived from $S(q)$ *via* Fourier transformation. This interparticular distribution function, $g(r)$, gives the probability of finding two particles with the distance r between each other:

$$g(r) = 1 + \frac{1}{(N_P/V)(2\pi)^3} \int_0^\infty [S(q) - 1] \frac{\sin(qr)}{qr} 4\pi q^2 \mathrm{d}q \tag{2.17}$$

The Teubner Strey model

For the special case of bicontinuous microemulsions (Subchapter 4.2), the structure factor can be analyzed using the Teubner Strey model.[28] The scattering profiles of such systems display a characteristic correlation peak. The scattered intensity can be calculated according to this model as

$$I(q) = \frac{8\pi\langle\eta^2\rangle/\xi}{a^2 - 2bq^2 + q^4} \quad , \tag{2.18}$$

in which η is the scattering length density contrast, $a^2 = (k^2 + 1/\xi^2)^2$ is always positive, and $b = k^2 + 1/\xi^2$ can be either positive or negative in dependence of the relative magnitude of the domain size d and the correlation length ξ. Per definition, k is $2\pi/d$. If b is positive, which means that the correlation length is larger than $d/2\pi$, a characteristic peak occurs with a maximum intensity at the position $q_{\max} = \sqrt{b}$. If b is negative and $\xi < d/2\pi$, such a peak is not observed. The correlation length d is the quasi-periodic repeat distance between water and oil regions within the microemulsion. The correlation length, ξ, refers to the positional correlation. The autocorrelation function of this system in real space, $\gamma(r)$, incorporates the alternating regions of water and oil and is given by

$$\gamma(r) = \frac{\sin(kr)}{kr} \mathrm{e}^{\frac{-r}{\xi}}. \tag{2.19}$$

2.1.4 Scattering from partially ordered systems

Similar to the highly ordered structures found in crystals, also partially ordered systems can give rise to characteristic reflections in scattering patterns. Examples of such systems discussed in this thesis are a microemulsion employing an ordered lamellar phase in the proximity of a surface (Subchapter 4.2), and the hexagonal structure of bundled actin filaments (Subchapter 6.3). Such systems can be evaluated using Bragg's equation:

$$n\lambda = 2d \sin\theta \,. \tag{2.20}$$

Combining this equation with the definition of $\vec{q}$ (equation (2.1)) is a direct method to calculate the lattice distance d of a lamellar, quasi-one-dimensional lattice in which n is the integer numeric order of the reflection:

$$q_n = \frac{4\pi}{\lambda} \sin\theta_n = n\frac{2\pi}{d} \tag{2.21}$$

For hexagonal phases, like observed in actin bundles, the lattice constant, d_{hex}, i.e. the distance between the centers of two rods or filaments, can be calculated as

$$s = \frac{q}{2\pi} = n\frac{2}{\sqrt{3}d_{\mathrm{hex}}}\sqrt{h^2 + k^2 + hk} \tag{2.22}$$

in which h and k are Miller indices.

2.2 X-ray reflectivity

2.2.1 Introduction

In contrast to SAXS focusing on the bulk solution, X-ray reflectivity is a method to study structures in direct proximity to an interface. This method is applied in Subchapter 4.2, where the near-surface behavior of a microemulsion under pressure is investigated. The geometry of an XRR experiment is illustrated in Figure 2-2.

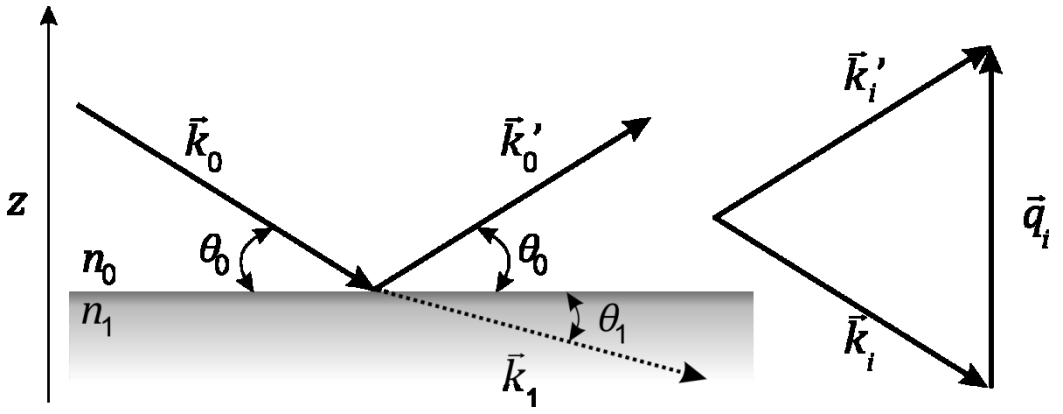

Figure 2-2. Geometry of an XRR experiment. [4]

An X-ray beam is reflected on the interface between two media with the refractive indices n_0 and n_1. The reflectivity $R = I/I_0$ is analyzed as a function of the incident angle θ_0, which is equal to the reflected angle under specular reflection conditions. Typically, the wave vector transfer, q (equation (2.1)), is used, which allows easier comparison of reflectivity curves recorded at different wave length, λ. Further, the observed intensity I is normalized to the intensity of the incoming beam to give the reflectivity $R = I/I_0$. The refractive index, n, for X-rays correlates with the electron density of the media[4]:

$$n = 1 - \frac{\lambda^2}{2\pi} r_e \rho + i\frac{\lambda}{4\pi}\mu = 1 - \delta + i\beta \tag{2.23}$$

Here, r_e is the classical electron radius, ρ the electron density and μ is the X-ray absorbtion coefficient of the medium. The dispersion δ contributes to the real pace while the absorption β contributes to the imaginary part. Below the critical angle, θ_c, the X-ray beam is totally reflected, i.e. $I = I_0$ and thus $R = 1$. The critical angle depends on the electron densities of the two media. [4] If the electron density of one medium is known, one can calculate the other by applying Snell's law:

$$n_1 \cos\theta_1 = n_2 \cos\theta_2 \tag{2.24}$$

At higher angles, the beam is partially reflected and partially refracted. The reflection coefficient is defined as the ratio of the amplitudes between the incident and the reflected beam. The reflection coefficient r_{01} between two media with the refractive indices n_0 and n_1 is defined as

$$r_{01} = \frac{q_0 - q_1}{q_0 + q_1} \mathrm{e}^{-\frac{1}{2} q_0 q_1 \sigma_{01}^2} \ . \tag{2.25}$$

Under specular conditions, the wave vector transfers q_0 and q_1 solely depend on the z-component of the wave vector, which is normal towards the xy-plane of the sample. The factor σ_{01} takes justice of a possible roughness of the interface and can also be used to describe a continuous change of the electron density between the two media. The wave vector transfer q_1 can be calculated from q_0 and q_{0c}, which is the wave vector transfer at the critical angle θ_c, by

$$q_1 = \sqrt{q_0^2 - q_{0c}^2} \approx \sqrt{q_0^2 - 16\pi r_e \rho} \quad . \tag{2.26}$$

The reflectivity can then be calculated as the mean square of the reflection coefficient, $R = |r_{01}|^2$. For a single layer on the interface of a medium, for example a protein adsorbed on an Si-wafer, one has to consider the reflection at two different interfaces. As a consequence, there are two reflection coefficients to be considered, $r_{01}$and r_{12}. Due to the interference of the two reflected beams after leaving the layer, a combined reflection coefficient can be calculated by

$$r'_{01} = \frac{r_{01} + r_{12}\, \mathrm{e}^{\mathrm{i} q_1 d_1}}{1 + r_{01} r_{12}\, \mathrm{e}^{i q_1 d_1}} \tag{2.27}$$

with q_1 as the wave vector transfer within the layer and d_1 as the thickness of the first layer. For a multilayer system, there are many parameters to vary in order to calculate a theoretical reflectivity curve.

2.2.2 The Parrat algorithm

Using the recursion algorithm developed by Parrat[29] allows to calculate the reflectivity curve of a multilayer system. Firstly, the combined reflection coefficient of the two lowest layers is calculated using equation (2.27). Then the next combined reflection coefficient is calculated using the combined reflection coefficient of the two lowest

layers and the layer above them. This algorithm is carried out until the top layer is reached. Applying this algorithm and thus determination of the electron densities, ρ_j and the thicknesses, d_j, of the layers allows to obtain an electron density profile of the sample normal to the sample plane. However, it has to be mentioned that the large number of variable parameters can lead to ambiguous results.

2.2.3 The effective density model

The Parrat algorithm is only applicable if the roughnesses of all interfaces, σ_i are much smaller in comparison to the thickness d_j of a layer, i.e. if $\sigma_j \ll d_j$. If the layer thickness is in the same order of magnitude as the fluctuations within the layers, i.e. $\sigma_j \approx d_j$, the effective density model[30] can be included in the calculation to take the roughness of the layers into account.

In the effective density model, it is assumed that the profiles at the interfaces are essentially determined by functions $Y_j(z)$ with the limits $Y_j(z) \to \pm 1$ for $z \to \pm\infty$, e.g. $Y_j(z) = \tanh\left[z\pi/2\sqrt{3}\sigma_j\right]$ or $Y_j(z) = \mathrm{erf}\left[z/\sqrt{2}\sigma_j\right]$. The fraction W_j of the material j at position z_j is than determined as

$$W_j(z) = \begin{cases} \frac{1}{2}\left[1 + Y_j\left(z - z_j\right)\right] & , \quad z \le \zeta_j \\ \frac{1}{2}\left[1 + Y_j\left(z - z_{j-1}\right)\right] & , \quad z > \zeta_j \end{cases} \tag{2.28}$$

with the coordinate

$$\zeta_j = \frac{\sigma_j z_{j-1} + \sigma_{j-1} z_j}{\sigma_j + \sigma_{j-1}} \tag{2.29}$$

denoting the depth at which the profiles of the upper and lower layer of interface j are connected continuously. In this model, the parameters σ_j, ζ_j, and $d_j = z_{j-1} - z_j$ need to be refined by fitting to the experimental data. From the dispersion $\delta_j\,(z)$, the electron density ρ_j can be derived according to equation (2.23).[30]

The difference in theoretical reflectivity profiles derived by the Parrat algorithm and effective density model will be most pronounced at large angles and thus large q_z-values, since the effective density model is of special importance for thin layers.[30] For example in Subchapter 4.2 of this work, the large q_z-range the application of this

model revealed the presence of a very thin water layer of about 0.8 nm thickness (~two water molecules) at the interface between the microemulsion and the silicon wafer.[31]

2.3 Experimental setups

2.3.1 High pressure cells

The high pressure cell for SAXS used in most of the experiments was developed by Dr. Christina Krywka (Tolan-Group, Experimental Physics I, TU-Dortmund University). The cell is made of high tensile strength alloy Inconel 718. It has a cubic body measuring 9 × 9 × 8 cm³.[32] It is suitable for pressures up to 400 MPa (4 kbar) and temperatures up to 60°C. The volume of the sample holder was reduced using PTFE-rings with an outer diameter of 7 mm and an inner diameter of 3 mm. Kapton-foil was mounted on the front and back side of the PTFE-rings using double-sided tape (Figure 2-3). This modification allowed to reduce the sample volume required from 55 µL to less than 10 µL. The reduction of the sample volume was especially useful for measurements of precious RNA and protein samples. The main advantage of this high pressure cell is that it has an additional opening for the sample holder, so that the diamond windows do not have to be removed when the sample is changed.

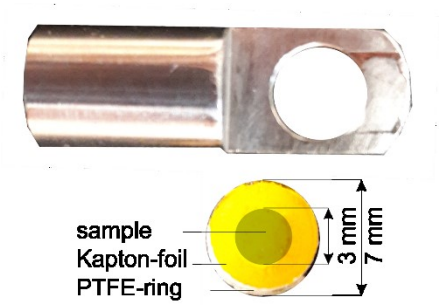

Figure 2-3. Reduction of the sample volume in the sample holder for the high pressure cell using PTFE-rings.

The high pressure cell used for the XRR measurements had a very similar setup. The outer dimensions of this cell are 98 mm × 90 mm × 80 mm and it is made out of high-strength steel (type 2.4668, NiCr19Fe19Nb5Mo3). The main difference to the previously described SAXS cell are the sample holders. These allow to mount a silicon wafer measuring 8 × 8 m on the bottom for reflectivity measurements.[33]

The second high pressure cell used for SAXS was built by Dr. Jürgen Woenckhaus (Winter-Group, Physical Chemistry I, TU-Dortmund University). It has a cylindrical

body and is made out of steel NIMONIC 90 Ni Cr 20 Co 18 Ti (No. 2.4969).[34,35] It is suitable for pressures up to 400 MPa (4 kbar) and temperatures up to 80°C. The sample holders were PTFE-rings with Kapton-foil.

In all three cells, flat diamonds (Type IIa, 6 mm in diameter, 1 mm thickness) served as windows. Since the transmission of X-rays through these diamonds is only 30 %, pressure dependent measurements could only be performed at Synchrotron sources. The temperature of the cells was controlled by an external water bath with an accuracy of $\pm$ 0.1°C. The commercially available high pressure spindle pumps used were either built by SITEC-Sieber Engineering AG (Maur (Zurich), Switzerland) or NovaSwiss (Effretikon, Switzerland)

2.3.2 X-ray sources

Kratky-Camera SAXSess mc²

Most of the temperature dependent measurements were performed in-house on the Kratky-Camera SAXSess mc² by Anton Paas (Graz, Austria). It contains an X-ray tube copper anode. The emitted K_α radiation (λ= 0.154 nm) is monochromatized by a Bragg-lattice. Samples were filled in to a capillary with 1 mm diameter and a sample volume of 10 µL (*µ-cell*). Measurements were performed in line-collimation with a beam of 1 mm high and a broadness of 10 mm. Temperature was maintained using the TSC 120 temperature control unit (Anton Paar, Graz, Austria). Imaging plates were used as detector. The exposure time was 30 min. The intensity was detected over a q-range between 0.1 and 4 nm^{-1}. The software 2D-SAXSquant was used to integrate the intensity in the 2D images in order to obtain scattering curves in dependence of the wave vector transfer, q. The raw data was normalized to the primary beam intensity and background corrected using a scattering curve of the respective solvent.

Beamline ID02 of the European Synchrotron Radiation Facility (ESRF)

Many high pressure SAXS experiments were carried out at the high brilliance beamline ID02 at the European Synchrotron Radiation Facility in Grenoble, France. At this recently upgraded beamline, three undulators provide a high photon flux with a maximum of 10^{14} photons/s/100 mA at 12.4 keV. Thus, the exposure time was always less than a second, typically between 0.1 and 0.5 seconds. In our

experiments, a beam energy of 16 keV (λ = 0.075 nm) was used. The beam size was 200 µm × 400 µm. The sample-to-detector distance can be varied between 1 and 10 m; for our experiments we usually used 2 m to cover a q-range between 0.05 and 4 nm^{-1}. The detector used was a FReLoN CCD detector with an active field of 100 mm x 100 mm and 2048 x 2048 pixels at a frame rate of 3 frames/s.

Beamline SWING of the Synchrotron SOLEIL

The French national synchrotron SOLEIL is located on the Plateau de Saclay in Saint Aubin, Essonne. At the SAXS beamline "SWING", the in-vacuum U20 undulator provides an electron flux of 8×10^{11} photons per second at 16 keV (with 400 mA ring). Our Experiments were carried out at 15 keV. The scattered intensity was detected using the SAXS-detector PCCD170170 (AVIEX). The beam had a size of 450 × 20 μm^2 FWHM in the experimental hutch. The sample to detector distance was 2 m. The exposure time was 1 s. The software FOXTROT programmed and provided by the beamline staff was used to convert the 2D images to 1D scattering curves.

Beamline BL9 of the Dortmunder Elektronen-Speicherring-Anlage (DELTA)

The pressure dependent XRR-measurements (Subchapter 4.2) were performed on the beamline BL9 at the electron storage ring DELTA. This Synchrotron facility is located on the campus of TU-Dortmund University, Dortmund, Germany. It is operated with an energy of 1.5 GeV and can reach a maximum ring current of 130 mA. One wiggler, two undulators, and various bending magnets provide Synchrotron radiation for several beamlines. The beamline is designed as a multi-purpose beamline, different setups for X-ray diffraction (XRD), gracing incident diffraction (GID), X-ray reflectivity (XRR), and SAXS are available.[32,36,37] The beam size is typically 1 mm in horizontal and 2 mm in vertical direction. The energy used for the XRR experiments was 27 keV to ensure proper transmission trough the sample. A PILATUS 100k detector was used for photon detection.

3 Biomolecules under extreme conditions

In this chapter, the relevance of studies under extreme conditions of temperature and pressure will be highlighted. Afterwards follow three short reviews on the effect of pressure on lipids, nucleic acids and proteins, respectively. Within these three subchapters, the corresponding systems investigated in this thesis will be introduced.

3.1 Extreme conditions of temperature and pressure

3.1.1 High pressure conditions and the origin of life

High hydrostatic pressure (HHP) is omnipresent in the environment. 88 % of the volume of the oceans is high pressure water. The average depth of the oceans is 3800 m, thereby establishing an average HHP of 38 MPa. The highest hydrostatic pressures in the ocean can be found in the Mariana Trench with a depth of 11000 m, where pressures of 110 MPa prevail. Such habitats are generally cold (~3°C), since they lack the presence of sunlight. Exceptions are hydrothermal vents. In these, the water can reach temperatures of up to 400°C. If this hot water mixes with the 3°C cold seawater, zones with a wide range of temperatures are produced.[38]

Very harsh conditions on the surface of the Hadean Earth including high radiation and a reducing atmosphere make deep sea waters a highly plausible habitat for the development of life.[1] The shielding effect of the water might have given way to prebiotic synthesis of nucleic acids, fatty acids and amino acids.[39,40] Upon this, an RNA world[3] and the first vesicles as well as subsequent protocells might have originated from the self-assembly of these molecules.[41,42]

3.1.2 Homeoviscous adaptation to high pressure habitats

The biological relevance of HHP is not limited to the origin of life. It is interesting to study how organisms adapted to these conditions, i.e. which strategies they developed to cope with such high pressures, involving modifications in their proteins, their membrane lipids and the synthesis of stabilizing cosolutes. The latter have a great influence on the temperature and pressure stability of proteins. The cytoplasm of cells contains many different organic and inorganic osmolytes as well as a large number of other macromolecules (crowding effect).

The chaotropic agent urea, for example, can denature proteins. Destabilizers like this compound form hydrogen bonds with the backbone of proteins. Thus, they favor unfolding of proteins, upon which further parts of the backbone become exposed and provide additional binding sites.

In contrast, cosmotropic osmolytes like trimethylamine oxide (TMAO) and sugars, stabilize proteins and are accumulated in the cells with rising pressure.[43] These osmolytes are excluded from the surface of proteins. This effect is referred to as preferential exclusion or, since the binding of water is preferred over the binding of the osmolyte, as preferential hydration.[44] These osmolytes stabilize the hydrogen bonding between water molecules and thus enhance the water structure in the hydration shell of a protein. Unfolding of a protein would provide further solvent accessible surface area and is avoided to prevent further loss in entropy by increasing the hydration shell surrounding the protein.[45]

Unlike in diluted solutions commonly used in *in vitro* studies, the volume of biological cells is occupied by a large number of different macromolecules. They reduce the volume of solvent available for other macromolecules. Thereby, the effective concentration as well as the chemical activity of the macromolecule increases. This so called excluded volume effect can alter the rates and equilibrium constants of reactions performed by these molecules. Especially the association of proteins or nucleic acids is favored if the available volume is limited. Enzymatic reactions can also be affected, if the reaction requires a large conformational change of the shape of the enzyme.[46] To mimic these crowding conditions *in vitro*, high concentrations of branched polymers may be added to the samples. For example, 15 wt% poly(ethylene glycol) with a molecular mass of 20 kDa is used as a crowder in this work to investigate the effect of crowding on the self-assembly of disodium guanosine monophosphate in aqueous solutions (Subchapter 5.1).

3.1.3 Technological relevance of high hydrostatic pressure conditions

Beside the biological relevance, pressure is also an interesting physical parameter. In contrast to temperature, which always involves concomitant changes of the energy and volume, pressure allows to study the volume changes only, leaving the energy in a system constant. Further, it provides a controlled way of modulating inter- and

intramolecular interactions. Non-covalent interactions are very sensitive to pressure, while covalent interactions are hardly influenced by pressures below 2 GPa.[38]

Since non-covalent interactions are vital for many biomolecules and thus organisms, high pressure can be used in food processing to inactivate viruses and bacteria.[47] In contrast to high temperature processes like pasteurization, the nutrients and flavors do not change markedly when high pressure is applied for preservation of foods. It affects all levels of cellular physiology, like metabolism, transport, transcription translation and membrane physiology. Cellular membranes are especially sensitive to changes in pressure.[2]

A more detailed review on the effect of pressure on the different classes of biomolecules will be given in the following subchapters.

3.2 The effect of temperature and pressure on lipids

Biological membranes establish a high complexity, including various proteins and many different kinds of lipids involving different chain length, saturated and unsaturated chains and different head groups. Lipids are an essential component of cell membranes forming a selectively permeable barrier between the interior of a cell and the outer environment. [48] This compartmentalization is also crucial to build up a concentration or pH-gradient, like used for energy storage in mitochondria. In contemporary cells, this barrier is mainly formed by a bilayer of phospholipids with integrated proteins controlling transport processes.[48] However, it was a long process until these modern lipids evolved. The first precursors to modern lipids were probably simple fatty acids, since they are found as a main product of Fisher-Tropsch-type reactions.[49–54]

Lipids self-associate in aqueous environment due to the hydrophobic effect. They consist of a hydrophilic head group and a hydrophobic tail and can form micelles, vesicles and bilayers when present in a sufficient concentration.[4] For example, fatty acids with a small hydrophilic head group and a single hydrophobic chain can form small, spherical micelles in which all chains associate in the center due to the hydrophobic effect and the hydrophilic head groups face the solvent. However, phospholipids like 1,2-dipalmitoylphosphatidylcholine (DPPC) with two aliphatic chains and a more bulky and charged head group forms bilayers. Whether a lipid forms micelles or bilayers depends on the critical packaging parameter (CCP)[4,55]:

$$\mathrm{CCP} = \frac{V}{A\,l} \quad , \tag{3.1}$$

where V is the volume of the hydrophobic chains, A the area required for the head group and l the length of the chains. If the CCP is lower than 1/3, micelles are formed. If it is between 1/2 and 1, bilayers are preferred. With a higher water content, these bilayers can be observed as multilamellar vesicles. Unilamellar vesicles are only stable at very low lipid concentrations in water.[4] The size of micelles and unilamellar vesicles can be analyzed by small-angle X-ray scattering when in the right order of magnitude, i.e. between 1 and 100 nm in diameter.

Due to the complexity of biological cell membranes, most studies on the phase behavior of lipid membranes were performed on model membranes consisting of one or very few components only. Even such a model system can show a very complex phase behavior. It can establish several lyotropic mesophases. This lyotropic polymorphism is influenced by many parameters, such as the characteristics of the lipid itself, the pH, the ionic strength, temperature, and pressure.[2,56–61]

In phospholipids, lamellar mesophases are the most common. Saturated phospholipids, as common in modern membranes, undergo two main temperature-dependent phase transitions: One pretransition from the L_β, gel-phase to the P_β, gel-phase and a main transition from the P_β, gel-phase to the liquid-crystalline and biologically relevant L_α phase at a higher temperature, T_m. In the gel-phases, the chains are extended and ordered, while in the liquid phase they are conformationally disordered.[60,61]

However, the lyotropic phases are not limited to lamellar structures. Bicontinuous cubic phases can be found in different lipids, like ethanolamines and monoacylglycerides occurring during fat digestion. Such phases also occur in the fusion process of two vesicles or cells and in cell division.[2,62–64] They involve a rearrangement of biological membranes to form non-lamellar highly curved lipid structures. Membranes in their cubic phase consist of a mostly bicontinuous unilamellar lipid bilayer in a periodic three-dimensional order.[2] Certain microemulsions can form disordered bicontinuous cubic phases. A third class of lyotropic mesophases are inverse hexagonal structures, which form when the CCP is larger than 1.

X-ray diffraction on stacked lipid layers allows to analyze these lyotropic mesophases by deriving the lattice constant from the position of the resulting Bragg peaks in dependence of temperature or pressure. In this work, this technique is applied in Subchapter 4.2, where the dimensions of the oil and water domains in a microemulsion are explored.

Lipids are the class of biomolecules which is most sensitive to changes in pressure. The lipids adapt to the compression by changing their ordering and packing to reduce their volume.[2] Thus, pressure has an ordering effect on these structures and can significantly increase the melting temperature necessary to reach the liquid phase essential for living organisms.[38] Further, the chain ordering is unfavorable to micelles establishing a high surface curvature making the accommodation of cylindrically shaped molecules unfavorable. The formation of vesicles with a lower surface curvature then leads to a relaxation of the system.[65] Further compression may lead to a deformation of the vesicles from a spherical to a prolate shape further reducing the surface.[2,56,57]

Organisms developed a variety of strategies in order to keep their membranes in the fluid phase at cold temperatures or high pressures. The inclusion of unsaturated lipids as well as lipids with shorter chain length in biological membranes lowers the transition temperature T_{m}.[66–68] Further, cholesterol plays an important role in biological membranes and can reach up to 50% of the lipid content of animal cell membranes. On the liquid-crystalline phase, it has a condensing effect, thereby increasing the packing density of the chains and increasing the thickness of the membrane. On the other hand, it inhibits the condensation of the highly ordered chains in the gel phases present at low temperatures. By these two effects, it drastically decreases the transition enthalpy of the melting, ΔH_m, until at cholesterol contents of more than 30 wt% the transition vanishes completely. These strategies are referred to as homeoviscous adaptation.[2]

3.2.1 Prebiotic lipids

Simple fatty acids and alkanols can be abiotically synthesized by Fisher-Tropsch-type reactions simulating geochemical conditions, like hydrothermal systems. These molecules have also been detected in carbonaceous meteorites.[49–54] It was documented by *Deamer* and others, that these are able to form membrane-like

structures in aqueous solution.[69–72] The stability of these membranes strongly depends on the pH, the concentration, ionic strength, and the specific head–group of the amphiphiles.[65] In Subchapter 4.1, the self-assembly and phase behavior of a mixture of decanoic acid and decanol, which can be synthesized in Fisher-Tropsch-type reactions, will be investigated.

Decanoic acid, also referred to as capric acid, is a saturated fatty acid with a carboxylic head group (Figure 3-1). This fatty acid occurs naturally in coconut oil (about 10%) and palm kernel oil (about 4%), otherwise it is uncommon in typical seed oils.[73] The head group is rather small compared to phospholipids. The lipid has a C_{10} chain, which is the average length obtained for fatty acids in the Fisher-Tropsch-reaction. This chain length is rather short in comparison to modern phospholipids, whose chains contain usually between 14 and 24 carbon atoms [48] and have at least one *cis*-double bond.

At elevated pH values, like those used in our study, the decanoic acid becomes deprotonated. Thus, it is negatively charged, making the self assembly of decanoic acid molecules energetically unfavorable. A partial substitution of the fatty acid by its corresponding alcohol allows the formation of micelles and vesicles. Decanol (Figure 3-1) is also a main product in Fisher-Tropsch-reactions. The effect of temperature, pressure and the preparation method on the morphology of the aggregates is investigated using SAXS in Subchapter 4.1.

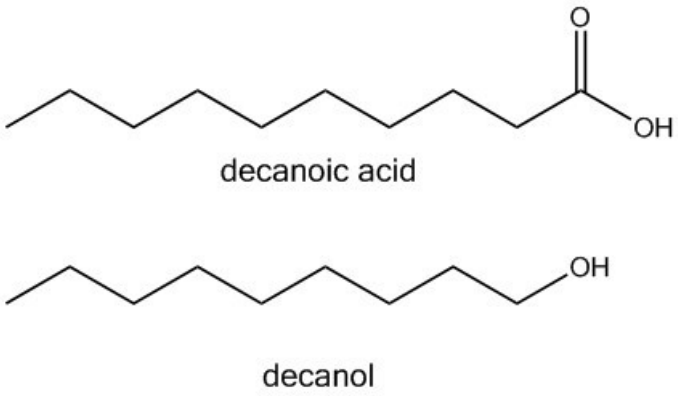

Figure 3-1. Chemical structures of decanoic acid and decanol.

3.2.2 Bicontinuous microemulsions

Lamellar-to-non-lamellar phase transitions in lipid model systems gained much attention during recent years as they are significant in a variety of dynamic

membrane-associated biological processes.[74–76] For example, the transition from a fluid lamellar phase to an inverse bicontinuous cubic phase has been studied to reveal mechanistic information about the final step in vesicle fusion. During this process, transient contacts between lipid bilayer membranes are formed, which widen and break to form interlamellar attachments or fusion pores.[74] Most of these studies were performed on highly ordered lipid systems. However, cellular membranes incorporate a high variety of lipids and can therefore be expected to form disordered phases. Disordered bicontinuous phases can, for example, be found in bicontinuous microemulsions (BME).

Microemulsions are ternary systems that consist of water, oil, and a surfactant lining the interface between the two. Their composition is characterized by the ratio of water and oil as volume fraction, ϕ, and by the mass fraction of surfactant in the emulsion, γ[77]:

$$\phi = \frac{V_{\mathrm{oil}}}{V_{\mathrm{water}} + V_{\mathrm{oil}}} \tag{3.2}$$

$$\gamma = \frac{m_{\mathrm{surfactant}}}{m_{\mathrm{surfactant}} + m_{\mathrm{water}} + m_{\mathrm{oil}}} \tag{3.3}$$

A microemulsion is referred to as bicontinuous if the oil and the water networks span the whole system. The bicontinuous phase is only obtained for certain compositions and at specific temperatures, as shown in the phase diagram in Figure 3-2 A. Beside the exclusively bicontinuous phase (1ϕ), oil droplets in water with coexisting oil phase ($\underline{2}\phi$) and water droplets in oil with coexisting water phase ($\overline{2}\phi$), and bicontinuous phase in coexistence with pure water and oil phases (3ϕ), are further prominent phases.

Interestingly, some BMEs show a transition from their bicontinuous structure in the bulk to a lamellar phase when approaching a surface (Figure 3-2), as revealed by neutron reflectometry and theory, recently.[78,79] Further, grazing incidence neutron spin echo spectroscopy (GINSES) revealed that the dynamics within such a system is significantly faster in the proximity of a hydrophilic solid interface.[80,81]

In the work presented in Subchapter 4.2, a mixture consisting of equal volumes of water and *n*-octane as an oil ($\phi = 0.5$), and 16 wt% of the surfactant tetraethylene glycol decanoyl ether ($C_{10}E_4$, $\gamma = 0.16$) was used to create a BME featuring such

phase behavior. As the name $C_{10}E_4$ suggests, this nonionic surfactant consists of four ethylene glycol repeat units (hydrophilic) and a C_{10} carbon chain (hydrophobic). The high amount of surfactant causes a very low interfacial tension between water and oil domains. Hence, curvature effects play an important role in BMEs. They are everywhere curved into saddle-like shapes to multiply interconnect throughout the sample in the three dimensions of space.

Such bicontinuous microemulsions can, for example, serve as a model system for cellular compartmentalization. They also serve as reaction media for biocatalysis, polymer synthesis, the dispersion of drugs, the extraction of contaminated material, and oil recovery[35,82–84].

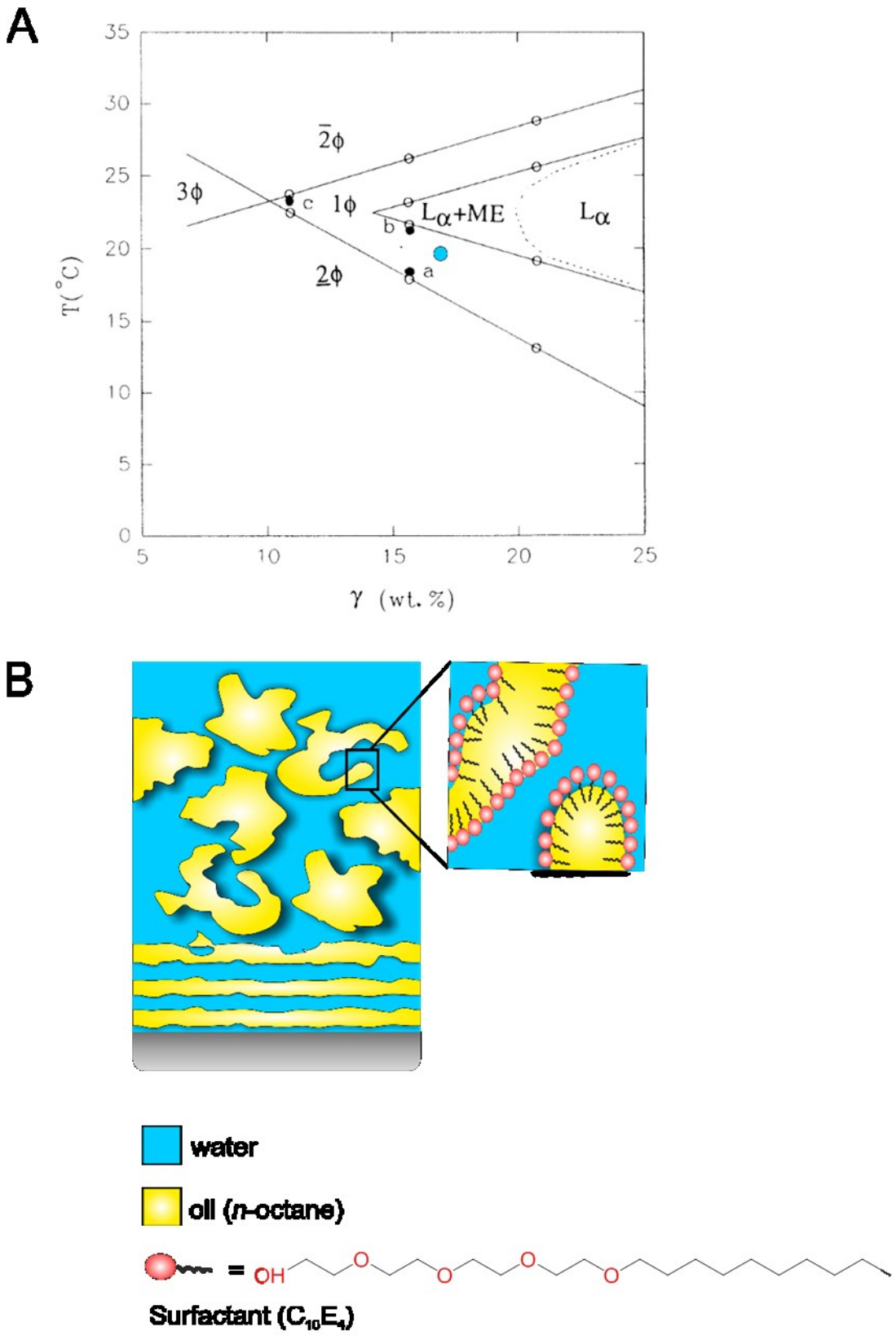

Figure 3-2. (A) Phase diagram of a microemulsion consisting of n-octane/D_2O/$C_{10}E_4$.[79] The blue circle indicates the conditions used in this study (bicontinuous phase). (B) Illustration of the phase behavior of the same microemulsion near a hydrophilic interface. The surfactant is distributed at the interface between water and oil.

3.3 The effect of temperature and pressure on nucleic acids

Nucleic acids fulfill various functions in living organisms. The genetic information is stored in the double-stranded desoxyribonucleic acid (DNA). During transcription, the RNA polymerase transcribes this DNA sequence to RNA sequences fulfilling different functions. The messenger RNA is used as a template during translation. In this process, a ribosome containing ribosomal RNA (rRNA) translates the messenger RNA (mRNA) to an amino acid sequence using transfer RNA (tRNA) coding specific amino acids. Moreover, RNAs are also involved in the regulation of gene expression.[48]

Similar to proteins, RNAs can form complex tertiary structures. The scaffold for this structure is given by secondary structural elements that are determined by canonical and non-canonical intramolecular base pairing. This leads to several recognizable "domains" of secondary structure like hairpin loops, bulges, and internal loops.[85] Due to the phosphate groups at the ribose-backbone, RNA is highly negatively charged. Therefore, metal ions such as Mg^{2+} are required to form secondary and tertiary structures, which are vital for their activity.[86] These ions also influence the stability of RNA structures against temperature and pressure. Electrostatic interactions are weakened by pressure due to the electrostrictive effect.[87–89] The dipolar water molecules can be packed more densely on exposed charged surfaces than in bulk water, leading to an increased hydration of the molecule. This is the driving force leading to unfolding. In contrast, pressure stabilizes stacking interactions and hydrogen bonds.[90,91]

Since RNA can form these complex secondary and tertiary structures, RNA can also act as a catalyst. An RNA molecule with an enzymatic activity is referred to as ribozyme.[92] The discovery or catalytically active RNA supported the RNA world hypothesis, which proposes that RNA played a key role as a first self-replicating system, since it can store information as well as catalyze reactions.[3,93]

A possible scenario for the development of an RNA world is the deep sea close to hydrothermal vents. Temperatures can lead to the loss of the secondary structure of nucleic acids. The denaturation temperature, T_{m}, of this transition is determined by the base sequence. In RNA, there are three hydrogen bonds involved in the pairing

between adenine and uracil and only two in the pairing between cytosine and guanine. Further, there are stacking interactions between the bases further stabilizing intramolecular base pairing. All these interactions can be disrupted by temperature and lead to denaturation (melting) of the nucleic acid's secondary structure.

Whereas the effects of pressure on lipid membranes and protein systems have been studied extensively, the knowledge about the effect of temperature and pressure on the conformation and stability of nucleic acids is still very limited. The intramolecular interactions within nucleic acids, i.e., base pairing and base stacking, are rather strong. These interactions are ultimately responsible for driving the native folding of DNA and RNA molecules. The effect of pressure on nucleic acids is rather complex. Generally, pressure stabilizes stacking interactions and hydrogen bonds and therefore increases T_{m}.[90,91]

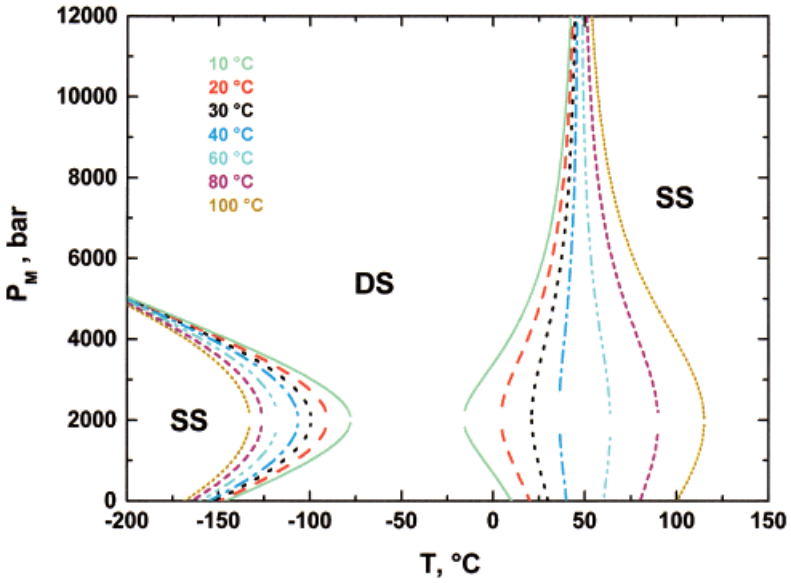

Figure 3-3. Putative phase diagram for the helix-to-coil transition of double stranded nucleic acid polymers. The denaturation pressure, p_{m}, is plotted as a function of temperature, T, for several values of the helix-to-coil transition temperature, T_{m}, at atmospheric pressure: 10°C (solid line); 20°C (dashed line); 30°C (dotted line); 40°C (dash-dot); 60°C (dash-dot-dot); 80°C (short dash); 100°C (short dot). In the figure, SS denotes the single stranded conformation and DS denotes the double stranded conformation.[94]

Dubins et al. present a pressure-versus-temperature diagram which shows that the effect of pressure on double stranded nucleic acids strongly depends on T_{m} at ambient pressure conditions (Figure 3-3).[94] If T_{m} is below 50°C at atmospheric pressure, pressures below 200 MPa have a destabilizing effect and pressures above 200 MPa have a stabilizing effect. If T_{m} is about 50°C at ambient pressure, elevated

pressures hardly affect the melting temperature. If T_m is above 50°C at atmospheric pressure, pressures below 200 MPa have a stabilizing effect and pressures above 200 MPa destabilizing effect, i.e. the effect of pressure is reversed.

Canonical DNA duplex structures are usually based on Watson Crick base pairs. These structures were found to have a negative partial molar volume, i.e. the volume change upon unfolding (melting), ΔV, of DNA is positive. This indicates that applying pressure will causes the duplex to be more stable.[94–97] In comparison to proteins for which a ΔV of unfolding is typically -30 to -100 mL mol^{-1}, the ΔV for DNA duplexes unfolding is rather small (about 1 to 5 mL mol^{-1}).[98,99] A negative volume change of nucleic acids upon melting only occurs in very special cases, such as in poly[d(A-T)]. Only in these cases, pressurization leads to the melting of the nucleic acid structures. Also structural investigations using high pressure NMR revealed that the conformation and configuration of the DNA duplex are not significantly perturbed under high pressure.[96,100] While pressure is generally not able to affect duplex structures, it was found to have a pronounced effect on non-canonical DNA structures, like G-quadruplexes.[95] In this case, the magnitude of ΔV can reach similar magnitudes as ΔV measured for proteins.

Though of high biological relevance for organisms living in the deep sea and also considering this habitat as a plausible cradle of life, there is still a lack of investigations on the effect of pressure on RNAs. In comparison to DNA, RNA structures were found to be more labile towards pressure.[95,101–106] For example, an RNA duplex with AU base pairs was found to be slightly destabilized by pressure,[104] and pressure was also found to destabilize tetraloop−receptor docking.[105] Furthermore, a previous study showed that HHP decreases the cleavage rate of the hairpin ribozyme, which was interpreted as pressure destabilizing formation of a catalytically critical loop−loop tertiary interaction in the ribozyme.[106,107]

3.3.1 The self-assembly of guanosine monophosphate sodium salt

The structural complexity of RNA molecules is not limited to base-paired regions and loops. Guanine quadruplex structures, in which four guanine bases form a tetramer via Hoogsteen base pairing, have achieved great attention during the last decades.[108–111] They are found in human telomeres and in some promoter regions

and are thus associated with aging and cancer.[112,113] Though most of the studies so far were performed on oligomers, G-tetramers can also be formed by the self-assembly of single guanosine monophosphate molecules (GMP), see Figure 3-4 A and B.[114–117] The disk-like G-tetramers stabilized by Hoogsteen base pairing can stack to form four stranded helical structures (Figure 3-4 C). These are stabilized by $\pi - \pi$ interactions. In these structures, each G-tetramer is rotated 30° against its neighbor and the stacking distance is 0.33 nm, which is very close to the distance between bases in an RNA helix.[115,118]

The formation of the tetramers as well as the formation of helical structures are promoted by monovalent cations (K^+, Na^+, NH_4^+), which can be sandwiched between two tetramers and thereby be complexed by eight carbonyl oxygens of the nucleobases. Moreover, cations are also located at the centers of the tetramers themselves, being coordinated by 4 oxygen atoms. In addition to the central channel of the helical structures, the cations can neutralize the negative surface charge of the phosphate backbone. [115,118]

With a sufficient amount of monovalent cations, the helices can associate to form a cholesteric and a hexagonal phase (Figure 3-4 D). The center-to-center distance between helices in the hexagonal phase is about 3.2 nm, i.e., there is a distance of about 0.7 nm between the helix surfaces.[114] This distance reflects the balance between the attractive forces leading to self-assembly and the repulsive forces preventing contact between the helices. The repulsion is probably of hydrational and not electrostatic nature, as *Mariani et al.* showed that this repulsion persists even at very high salt concentrations.[114]

In the work presented in Subchapter 5.1, the effect of temperature and pressure as well as of different cosolutes (monovalent cations, TMAO, PEG 20 kDa) on the self-assembly of guanosine monophsosphate sodium salt at various pressure conditions is explored. Depending on the conditions, the size of the aggregates is analyzed or the changes in the lyotropic hexagonal phase with pressure is investigated.

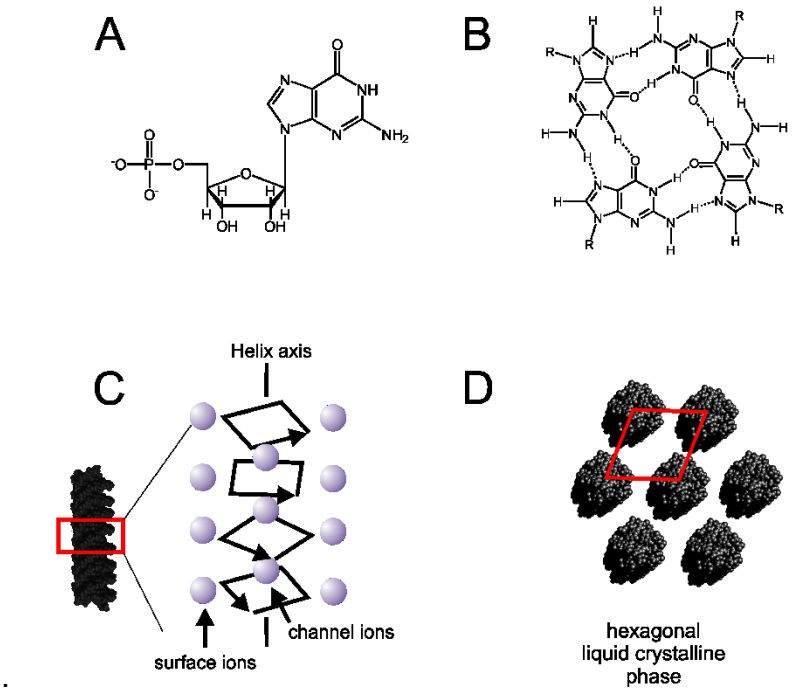

Figure 3-4. Self-assembly of GMP. (A) Structure of a GMP molecule. (B) Assembly of four GMP molecules to form a tetramer via Hoogsteen base pairing. (C) Stacking of tetramers to form a helical structure. (D) Assembly of the helices to form a lyotropic hexagonal phase. Parts of the figure were adapted from literature.[118]

3.3.2 The small RNA hairpin

The hairpin is a common secondary structure element in RNA. Hairpin motives can serve as nucleation sites for RNA folding, ligand binding and tertiary folding initiation,[119–125] for example in ribozymes and riboswitches. The small RNA hairpin (sRNAh) structure is formed when a polynucleotide single strand folds back on itself. The formation of Watson-Crick base pairs results in a helical stem capped by a loop (Figure 3-5). The amount of nucleotide residues at the loop varies, depending on the RNA molecule. For example, tRNA hairpin loops contain seven nucleotides while ribosomal hairpin loops contain only four nucleotides.[119]

It has been found in various studies that 70% of all tetraloops in ribosomal RNA are either UNCG or GNRA (N = nucleotide, R = purine), and they vary between organisms, from UUCG to GCAA for the same hairpin in closely related organisms.[126] Due to the presence of several non-canonical interactions,[127,128] these RNA hairpins have a significant thermodynamic stability.

Beside their pronounced thermostability, hairpin structures are of high biological importance, since they occur in many RNA structures. Their features as common

simple and small structural elements make them ideal models for folding studies. Therefore, they serve as prototype for folding dynamics and structural stability studies of polynucleotides, also in theoretical studies [104,128–133].

These theoretical studies predicted a rather complex energy landscape, even for such small tetraloop hairpins like UUCG and GCAA hairpin loops.[128] Their folding mechanism cannot be depicted by a simple two-state kinetic profile. They are predicted to be highly thermostable, even at simulation temperatures of 1000 K, extended-chain confirmations are hardly populated.

The folding free energy landscape of the RNA tetraloop gcGCAAgc recently investigated by a molecular dynamic study revealed that the stem of the loop preferably adapts a right-handed A-RNA confirmation, while the loop can adapt various configurations. But also a stem in the left-handed Z-RNA conformation and a compact purine triplet have been found. All of these confirmations establish different stabilities against temperature and pressure.[133] High hydrostatic pressure can lead to a shift in the equilibrium from the Z-RNA to the A-RNA confirmation, since the first is destabilized and the latter is stabilized upon compression. Beside directly influencing the folding of the RNA, high pressure can also alter the interaction of the RNA with solvent molecules and ions.

The small hairpin under investigation in this work (Subchapter 5.2) is a short strand of eight nucleotides with the sequence gcUUCGgc (Figure 3-5). The bases in lower case refer to the helical stem, i.e. form base pairs, while those in the upper case are in the loop region. The folding/unfolding equilibrium thermodynamics of this RNA tetraloop has been studied theoretically by *Gracia* and *Paschek*. Their work resulted in a temperature-pressure stability phase diagram of the small RNA hairpin, which shows the population of multiple conformational states.[104]

The construct used in the work presented here is labeled with two fluorophores, since the measurements were performed to complement FRET studies. The donor fluorophores Cy3 and the acceptor fluorophore Cy5 are attached to the 5’ and 3’ ends of the hairpin, respectively.

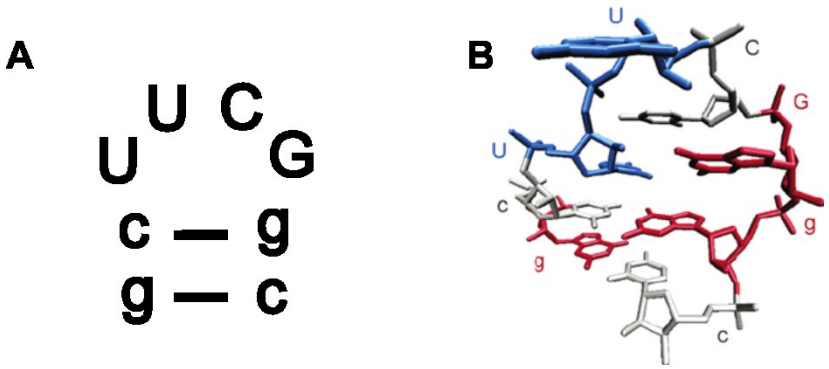

Figure 3-5. Schematic representation (A) and 3D-structure [129] (B) of the stem-loop structure of the sRNAh with the sequence gcUUCGgc. The bases written in upper case are the unpaired bases found in the loop region, and those written in lower case comprise the stem. Protein Data Bank (PDB): 1F7Y. In the labeled sRNAh, the donor fluorophore Cy3 and the acceptor fluorophore Cy5 are attached to the 5' and 3' ends of the hairpin, respectively.

3.3.3 The hairpin ribozyme

The RNA world hypothesis proposes that early life forms were based on RNA molecules. These molecules combined two important functions: Storage of genetic information and catalytic activity.[3] RNA with these two functions is referred to as ribozyme. The discovery of ribozymes greatly supported the RNA world hypothesis. Today it is known that there are thousands of ribozymes in each living cell. For example, the 28S-rRNA catalyzes the formation of peptide bonds in the eukaryotic ribosome during translation.[134]

The cleavage or ligation of RNA and DNA and peptide bond formation are the most common activities of natural or *in vitro*-evolved ribozymes.[135] Thus, RNA can splice itself to its functional form (self-cleavage). In former times, it was assumed that the catalytic activity of ribozymes would be limited to phosphate chemistry. This assumption has been overcome and it is established now that the catalytic range is much broader.

However, it is still largely unknown how the catalysis works mechanistically and which conformational changes need to be involved, in particular upon changes in temperature and pressure. Although pressure effects on protein-catalyzed reactions have been extensively studied in the last years,[136–143] there are only a few studies investigating the pressure effects on catalytic reactions of ribozymes.[106,144,145] In particular, very little is known about pressure-induced effects on the self-cleavage reaction catalyzed by ribozymes.

The hairpin ribozyme (HpRz) studied in this work (Subchapter 5.3) is a small nucleolytic ribozyme found in tobacco ringspot virus satellites. It catalyzes a reversible self-cleavage reaction by transesterification, which is sequence-specific.[146–149] The cleavage and ligation process the products of rolling circle virus replication into linear and circular satellite RNA molecules.[149] The hairpin ribozyme consists of two independently folding domains, A and B. Each of them consists of an internal loop and two helices (Figure 3-6 A). Its tertiary structure (Figure 3-6 B) is similar to a paperclip, hence it is also referred to as 'paperclip ribozyme'.

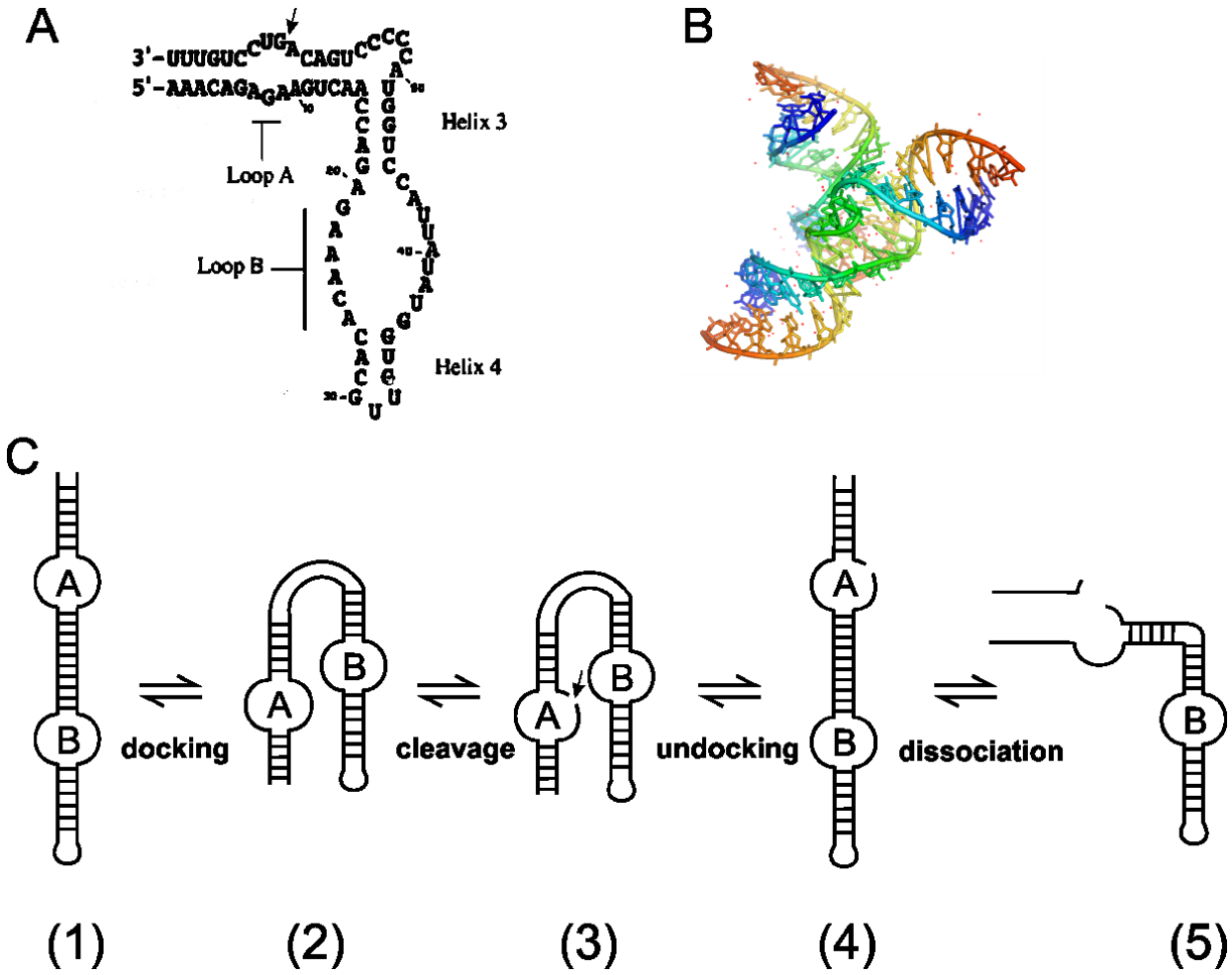

Figure 3-6. (A) Secondary structure [150] and (B) tertiary structure (PDB ID: 2OUE) of the self-cleaving wild-type hairpin ribozyme (HpRz) from tobacco ringspot virus satellite. The arrow in (A) marks the self-cleavage site. (C) Schematic representation of the entire multistep self-cleavage process of HpRz involving non-covalent steps before and after the covalent self-cleavage reaction from (2) to (3). Scheme based on a publication by *Walter et al.*[151]

The overall reaction process contains at least three major steps. The first step is the docking of the loops. After this follows the chemical cleavage step itself and finally undocking and the dissociation of the cleaved product (Figure 3-6 C).[152–160] The docked state, also referred to as pre-catalytic state, is essential for the cleavage reaction. It is formed by a rearrangement of loops A and B (Figure 3-6 C) by coming into close proximity.[150,161,162] It has been found that the adjacent nucleobases A38 and G8 in the reaction site play an important role in the stabilization of the transition state *via* distinct hydrogen bonding interactions.[163–170]

3.3.4 Phenylalanine transfer RNA

In contemporary cells, aminoacylated transfer RNA connects the RNA and the protein world and plays a central role in protein biosynthesis.[93] They translate the codons in the mRNA to the according amino acid. The translation from RNA to an amino acid sequence is not only undertaken frequently in each living cell, but was also a key step in the development of proteins and the establishment of the genetic code. *De Farias et al.* even proposed very recently that these molecules were the core in the transition from an RNA to a modern ribonucleoprotein world.[171]Typically, tRNA molecules have a length of 76-95 nucleotides. In general, tRNAs establish a cloverleaf-like secondary structure. Their anticodon, consisting of three bases complementary to the codon in the mRNA, is in the middle of their lower loop. They fold into complex three-dimensional structures, which are usually L-shaped. Detailed molecular mechanisms that drive formation of RNA tertiary interactions and how they are affected by temperature, pressure, and ionic strength, are not yet well understood.

The molecule under investigation in this work (Subchapter 5.4) is the 76-residue yeast phenylalanine transfer RNA, $tRNA^{Phe}$, of *Saccharomyces cerevisiae*. This molecule has a particularly well known structure which includes many structural motifs common in tRNA such as turns and hairpins. Like many tRNAs, $tRNA^{Phe}$ has a cloverleaf-like secondary structure that turns into a L-shape tertiary structure upon folding (Figure 3-7). In addition, it has a modified nucleobase in the anticodon loop, the wybutine or Y-base, which was used as intrinsic fluorophor in complementary fluorescence spectroscopic studies. As observed frequently in RNAs, divalent ions, such as Mg^{2+}, are required for the conformational stability of the tertiary structure.[172–174] The latter contains various cation binding sites. The complex tertiary structure is

further stabilized by extensive stacking interactions and base pairing within and between its helical stems. Interestingly, the majority of these tertiary base interactions are non-Watson-Crick pairs.

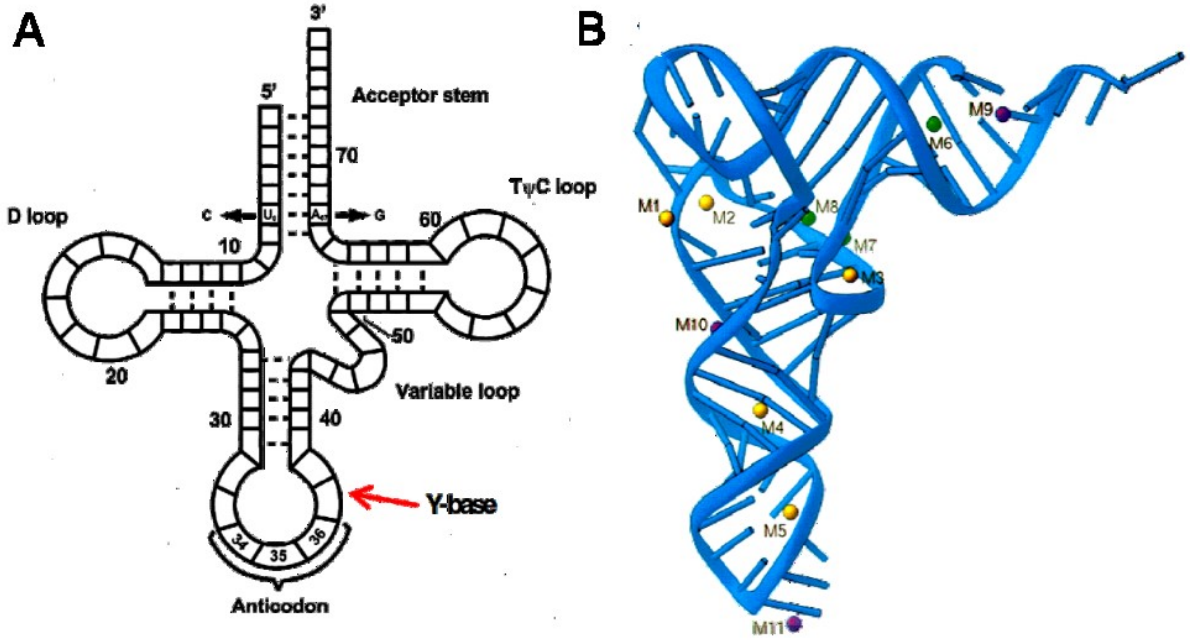

Figure 3-7. Cloverleaf-like secondary structure (A) and L-shaped tertiary structure (B) of $tRNA^{Phe}$.[175,176] The Y-base is indicated by a red arrow.

3.4 The effect of temperature and pressure on proteins and peptides

Proteins fulfill various functions inside the cell. They catalyze metabolic reactions, are involved in DNA replication and the response to stimuli as well as in the transportation of molecules and in maintaining the cellular skeleton. The primary structure of a protein is determined by its amino acid sequence, which is dictated by the nucleotide sequence of their genes. Depending on this sequence, the amino acid chain folds to α-helices, β-sheets and loop regions. These structural motifs are referred to as secondary structure of a protein. They are based on intramolecular hydrogen bonds within the peptide backbone of the protein. Finally, hydrophobic interactions between the amino acid residues lead to the complex, three-dimensional tertiary structure required for the function of the protein.[48] This complex folding can be influenced by parameters like temperature, pressure and cosolutes, which might lead to the denaturation of a protein.

While heat generally results in the loss of hydrogen bonds resulting in extended unfolded states, pressure favors hydrogen bonding but disturbs hydrophobic

interactions. Thus, in proteins the pressure-induced unfolded state can be substantially different from the heat-induced unfolded state. The unfolded state induced by pressure is more compact and often resembles “molten-globe”-type structures, since mainly the tertiary structure is influenced and the secondary structure can even be stabilized. Next to the decrease of void volume, the penetration of water between the hydrophobic residues in the protein interior is discussed as a plausible mechanism for pressure denaturation. While monomeric proteins usually unfold at pressures above 200 MPa, oligomeric or two different, interacting proteins might be disrupted already at much lower pressures of 100-200 MPa only.[38,177–179]

Noteworthy, proteins can also unfold upon cooling, even though it is difficult to access this process experimentally. Only moderate pressure allows to cool aqueous solutions to temperatures of about -15°C in order to study the cold denaturation of proteins. Like pressure, cold temperature does not lead to a complete disruption of all hydrogen bonds, many structural motives within the protein remain intact.[38]

T p,T-stability diagram of a protein has an elliptical shape. Several methods can be used to determine this diagram. Thermodynamic methods like differential scanning calorimetry (DSC) can be applied to investigate the changes in energy upon denaturation. Spectroscopic methods like Fourier transform infrared spectroscopy (FTIR) and NMR allow to explore the changes in secondary structure. Finally, scattering methods, as mainly used in this work, allow to study changes in size and shape upon denaturation. As an example, the p,T-diagram of SNase is shown in Figure 3-8.[180]

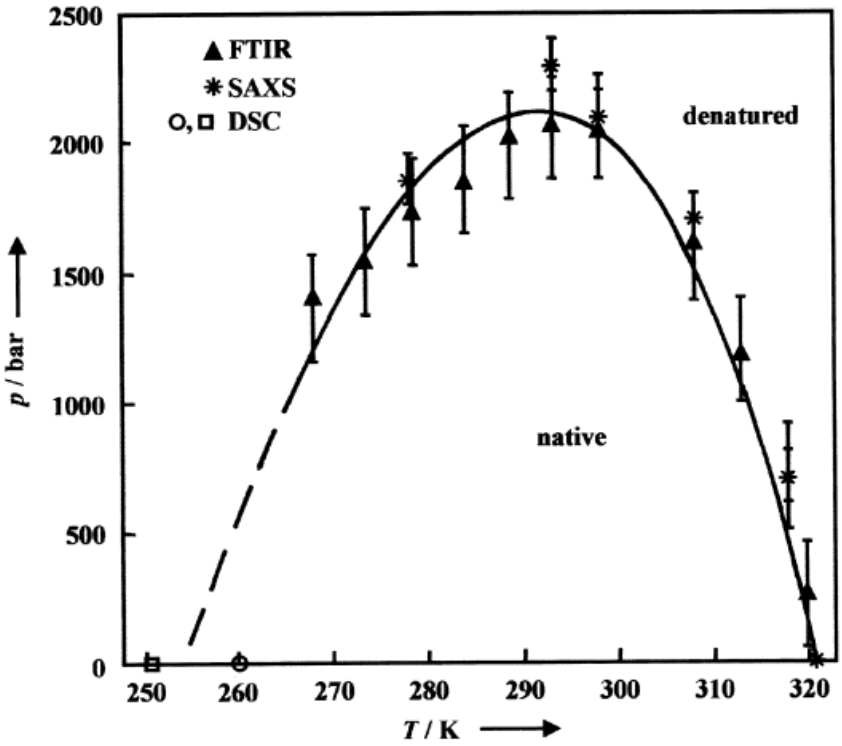

Figure 3-8. Temperature versus pressure stability diagram of SNase at pH 5.5 as obtained by SAXS, FTIR and DSC measurements.[180]

3.4.1 Elastin-like peptide

The elastic properties of connective tissues like skin, lungs, heart and vascular walls are maintained by the protein elastin. It is responsible for the tissue resuming its shape after being stretched or contracted. The elastic properties of elastin are determined by its molecular structure. It is composed of cross-linked units of its soluble precursor, tropoelastin. These molecules are cross-linked via hydrophilic domains, which are rich in the amino acid lysine. [181] Tropoelastin consists of a large number of hydrophobic domains containing repetitive units of amino acids like VPGVG, GGVP or GVGVAP, which are also responsible for the elasticity of the monomeric precursor of elastin.[182]

Due to the many hydrophobic residues, tropoelastin performs a so-called ‘inverse temperature transition’ (ITT) upon heating. In particular, temperature induces a transition from a disordered to an ordered state in this protein, which is contradictory to the usual effect of temperature on proteins. This process is still not well understood, however, it is assumed that the gain in entropy of the water molecules released upon hydrophobic interactions is its driving force. Details of the molecular origin of this process are still subject of controversial debate. The different

approaches of explaining this unusual behavior involve classical rubber elasticity,[183,184] librational entropy mechanisms,[184–186] the hydrophobic collapse, multiphase models[187,188] or iceberg/clathrate formation.

Interestingly, even a single VPGVG pentapeptide shows a transition to a Type II β-turn with increasing temperature.[189] Thus, such short peptides can be used as a model system. The studies presented here (Subchapter 6.1) were performed on the elastin-like peptide (ELP) with the sequence GVG(VPGVG)$_3$ in order to investigate the influence of cosolvents and confinement on the inverse temperature transition of ELPs. The ITT of this peptide has previously been studied by NMR[190] and theoretical investigations[191]. The work presented in this thesis focuses on the overall changes in shape with temperature under the influence of different cosolvents like TMAO, urea and trifluoroethanol (TFE).[192]

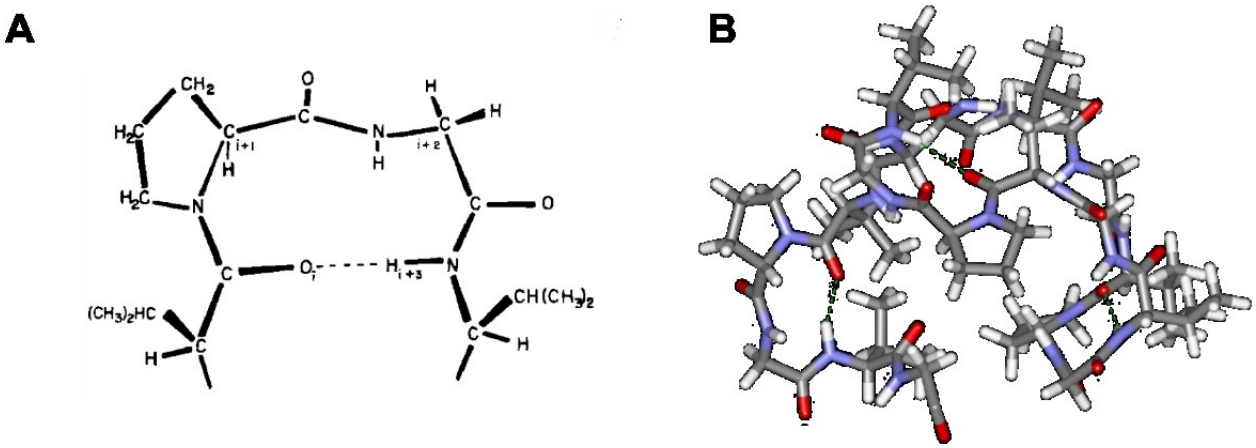

Figure 3-9. The β-turn in the pentapeptide repeat unit (A)[193] and illustration of the three dimensional, left-handed β-helix structure occurring in the peptide GVG(VPGVG)$_3$ (B).[190] Hydrogen bonds are indicated as dashed lines in (A).

3.4.2 Phosphoprotein 32

Phosphoprotein 32 (PP32), also known as Anp32A, is a member of an evolutionarily conserved acidic nuclear phosphoprotein family. Proteins of the PP32 type are involved in many cellular functions, such as modulation of cellular signaling and gene expression. They fulfill important functions, such as regulation of the morphology and dynamics of the cytoskeleton, cell adhesion, neuronal development, or cerebellar morphogenesis.[194] Furthermore, PP32 can act as a tumor suppressor.[195] PP32 proteins establish leucine-rich repeats (LRR), a structural motif occurring in many functionally different proteins. The leucine-rich repeats form β-strands with the

hydrophobic leucines pointing towards the core of the protein.[196] These repeats are very well suited to investigate the energetic contribution of single structural motives, since their unfolding is very cooperative.[197]

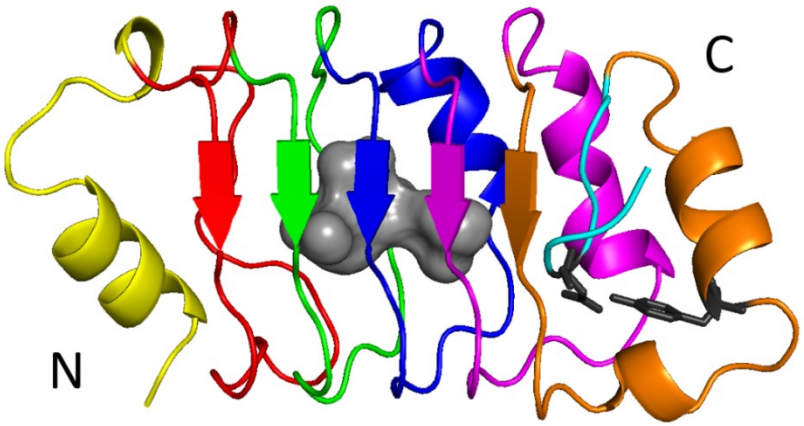

Figure 3-10. Ribbon diagram of the crystal structure of the repeat protein PP32 (PDB: 2JE0), created with PyMOL.[198] The N-terminal capping motif is shown in yellow. Repeats 1−5 are in red, green, blue, purple, and orange, respectively, and the C-terminal capping motif is colored cyan. The grey spheres represent the solvent excluded voids in the structure, which are calculated by HOLLOW[199] with a grid of 0.025 nm and a probe radius of 0.12 nm. The hydrogen-bonded Y131 and D146 are shown as black sticks.

In many proteins, capping motifs are attached to the LRR motif. They shield the hydrophobic core from the solvent, thereby preventing aggregation.[200] Further, they guide folding of the LRR region and can bind to other proteins. PP32 has five LRRs in its LRR domain, which is flanked by an N-terminal (NCap) and a C-terminal (CCap) capping motif, which are both highly conserved. In the CCap, Y131 and D146 form a structural hydrogen bond. Removal of the CCap unfolds PP32 completely. [201] If these residues are mutated (Y131F/D146L) to interrupt this hydrogen bond, the overall fold is still very similar to the wildtype PP32. This indicates that this H-bond is not vital for maintaining the structure. In contrast to the CCap, removal of the NCap does not lead to complete unfolding of the protein. Even though the LRR region is destabilized, it still retains significant secondary structure content.[201]

3.4.3 Actin bundles

The maintenance of the cytoskeleton is vital for every cell. It provides the cell shape and integrity and permits movement. One of the most important proteins in this skeleton is actin; it is the most abundant intracellular protein in many eukaryotic cells.

It is highly conserved, none of its 375 amino acids differs between chicken and humans in its skeletal muscle isoform.[202]

The monomeric form of actin is referred to as G-actin (G for globular). It is folded into two domains, which are stabilized by an adenine nucleotide incorporated between them. In cells, G-actin is usually saturated with ATP, because it occurs in higher concentrations therein. However, actin has also a high affinity for ADP and, due to many carboxylic side chains of its amino acids, to Mg^{2+} ions. The G-actin proteins can self-assemble to form filamentous actin (F-actin), which is responsible for the mechanical stability of cells (Figure 3-11). This self-assembly proceeds in three steps. The first and rate-determining step is the nucleation, in which three G-actin proteins form a nucleus. After this follows the elongation step, in which polymerization is much faster than depolymerization and the filament grows. Depolymerization occurs, when the bound ATP becomes hydrolyzed to ADP. Finally, the process reaches a steady-state, in which polymerization and depolymerization are in equilibrium, so the length of the filament remains constant.[48]

At physiological pH-values, F-actin is a polyanion and has similar features as other well-characterized polyelectrolytes, such as double-stranded DNA.[203] Thus, repulsive interactions between actin filaments would be expected in aqueous solution according to mean-field theories such as the Poisson-Boltzmann formalism.[204] *In vitro*, like-charge attractions between the polyanionic actin filaments can be induced by adding a high amount of divalent cations. In this case, F-actin can be bundeled to form B-actin (Figure 3-11).

In vivo, actin binding proteins, such as fascin, are used to bundle these filaments. Fascin is a key bundling protein in filopodia.[205–208] These thin, finger-like membrane protrusions can sense the mechanical and chemical environment of a cell.[209] Filopodia establish various functions, they are employed in cell migration, play an important role in the adhesion of cells to the extracellular matrix within tissues, in the formation of neurite outgrowth, and in wound healing.[210] Interestingly, fascin is also a biomarker in cancer diagnosis and prognosis because its elevated expression correlates with increased tumor metastasis and invasiveness.[211] Fascin has a molecular weight of 55 kDa and establishes four β-trefoil domains arranged in a two-lobed structure with pseudo-2-fold symmetry.[206,207]

The molecular mechanism of F-actin bundling by fascin is not fully understood yet. Mutagenesis studies revealed at least two positively charged actin binding sites which are conformationally connected, allowing cooperative binding of F-actin.[207] When approximately every fourth actin is bound to fascin, saturation of bundling occurs.[205,208] Fascin induces a maximal overtwist of 0.9° per monomer in the native F-actin helix by bundling (13/6 monomers/turn). This induced turn is concentration dependent.[212]

The question why nature actively produces proteins to bundle F-actin when it can also be bundled by divalent ions present in high abundance within the cell is addressed in Subchapter 6.3. The hexagonal arrangement of the actin filaments within the B-actin allows to explore the temperature and pressure stability of magnesium- and fascin-induced bundles using X-ray diffraction.[213]

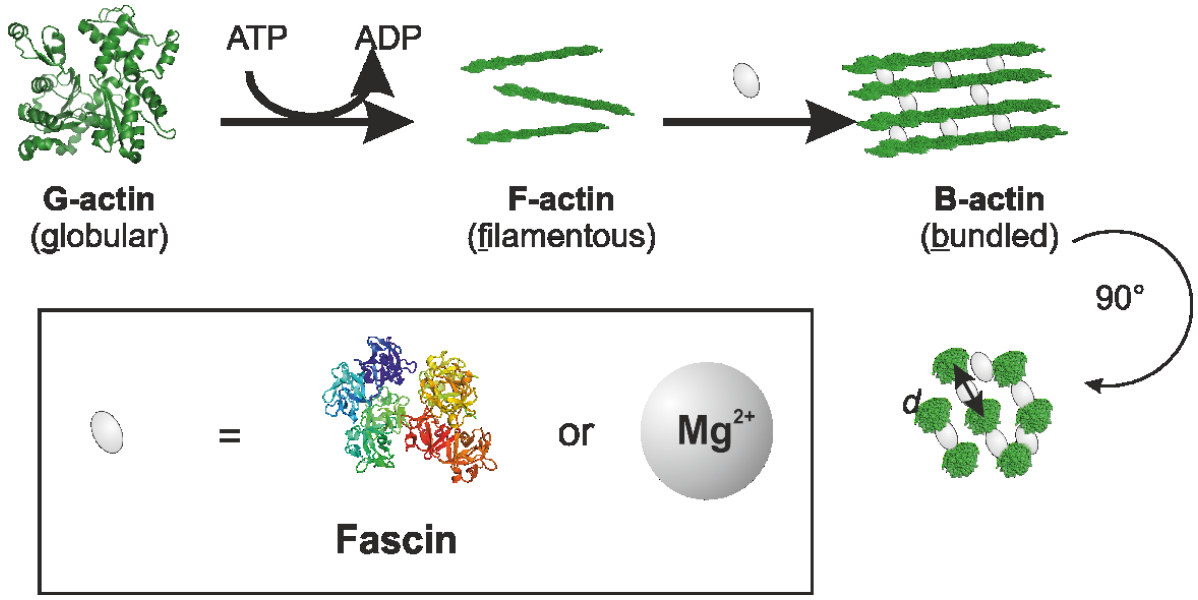

Figure 3-11. Structural forms of actin. Monomeric G-actin (PDB-ID:1J6Z) polymerizes to filaments (F-actin, PDB-ID: 3G37). Condensation agents, such as fascin (PDB-ID: 3P53) or magnesium, can induce bundling of actin filaments (B-actin) with a hexagonal structure.

4 Investigations of lipids

The following subchapters describe the structural investigations on two different lipid systems by scattering methods. In the first subchapter, the effect of temperature and pressure on a prebiotic lipid mixture is explored. Thereby, SAXS is applied to monitor the changes in the equilibrium between micelles and vesicles with these parameters. In the second subchapter, the effect of pressure on the lyotropic phases of a microemulsion is analyzed in direct proximity to a Si-wafer and in the bulk solution using X-ray reflectivity and SAXS, respectively.

4.1 Prebiotic lipids

4.1.1 Introduction

In this subchapter, the structural properties of a prebiotic lipid system consisting of an aqueous solution containing decanoic acid (DA) and decanol (DOH) are investigated using scattering techniques. Small-angle x-ray scattering is an excellent method of choice for structural elucidation of systems of colloidal size, typically up to 100 nm, and was used to obtain further insights into the pressure- and temperature-induced structural changes of the prebiotic lipid mixture, especially on the equilibrium between micelles and vesicles. Dr. Shobhna Kapoor and made complementary investigations on the same system using FTIR, electron microscopy, and dynamic light scattering. Dr. Sebastian Grobelny is acknowledged for recording the pressure-dependent scattering data, which was evaluated in the course of this work and is presented here together with the data recorded using our in-house instrument. The results of these investigations have been published in the journal *Angewandte Chemie*[65] and are partially reproduced here with permission, Copyright © 2014 by John Wiley & Sons.

4.1.2 Materials and methods

Sample preparation

Decanoic acid, decanol and 1-decanoyl-rac-glycerol and all other chemicals and solvents were purchased from Sigma-Aldrich. The vesicles were prepared by mixing the fatty acid and the other components as neat oils to obtain the desired composition, following dispersion in aqueous 0.2 M bicine buffer solution titrated with NaOH to pH 8.5. This was followed by vigorous vortexing and tumbling overnight at

room temperature. The final total amphiphile concentration (i.e. decanoic acid + decanol) in the preparation was 80 mM, unless noted otherwise.

For some samples, vesicles were extruded 11 times through 100 nm pore-sized polycarbonate membrane using an extruder (Avanti Polar lipids, Alabaster, USA). To prevent excessive polycarbonate membrane fouling and concomitant loss of fatty acid material, the hydrated fatty acid mixtures were disrupted by five freeze-and-thaw cycles prior to extrusion. In addition, the extrusion was performed at a temperature above the melting temperature of the amphiphillic mixture (i.e. at room temperature, 25°C). These steps help prevent significant loss of material during extrusion, and improves the homogeneity of the size distribution of the final suspension.[214]

Small-angle X-ray scattering

The pressure-dependent SAXS experiments performed by Dr. Sebastian Grobelny were carried out at the high brilliance beamline ID02 at the European Synchrotron Radiation Facility in Grenoble, France. The X-ray energy was 12.4 keV, which corresponds to a wavelength λ of 0.1 nm, with a flux of $4 \cdot 10^{13}$ photons/s. The pressure-dependent scattering curves were recorded with a CCD-detector with a sample to detector distance of 1 m, covering a range of momentum transfers from 0.2 to 3.30 nm^{-1}. The exposure time was between 0.05 and 0.5 s. The measurements were carried out in the high-pressure cell constructed by *Woenckhaus*[34]. High hydrostatic pressures up to 250 MPa in steps of 10 MPa were applied at 25°C using water as pressurizing medium. Temperature control (with an accuracy of ± 0.2°C) was achieved by a computer-controlled water circulation system from a thermostat through the temperature-controlled jacket of the pressure cell. The time for thermal equilibration before each measurement was set to 15 min. For the measurements, a total of 1 mL of the sample was filled into the pressure cell, yielding a concentration of 3 % (w/w). The scattering intensity curves were corrected by background subtraction using the scattering intensity of the pure solvent, taking into account the different absorption factors, and plotted against the magnitude of the wave vector transfer, q , by a MATLAB based software, provided by the ESRF[215]. The pressure-dependent SAXS measurements only employed the non-extruded fatty acid mixture comprising decanoic acid: decanol (2:1 molar ratio, pH 8.5).

In-house measurements were carried out in the SAXSess mc^2 small-angle X-ray scattering instrument from Anton Paar GmbH (Graz, Austria). The sample was measured in the slit configuration using a 1 mm quartz capillary provided with the TCS 120 temperature-controlled sample holder unit from Anton Paar (Graz, Austria). The exposure time of the sample to the X-rays was 30 min per measurement. While recording the temperature-dependent scattering data, temperature was adjusted using a Julado F25 heating circulator (Seelbach, Germany) and the actual cell temperature was monitored by the TCS control unit for TCS sample stages from Anton Paar (Graz, Austria). The 2D images obtained were transformed to an intensity profile, $I(q)$, using the software 2D-SAXSquant. The data were collected for q-values between 0.12 and 4.00 nm^{-1}.

The raw data obtained were normalized to the primary beam intensity and corrected by background subtraction using the scattering intensity of the pure solvent (0.2 M bicine buffer) in SAXSquant 3.1 software provided with the SAXSess mc^2 system. Further, the data were desmeared to compensate for instrumental broadening effects ("slit-smearing") using the GNOM software[216]. The latter was also used to calculate the according pair distance distribution functions, $P(r)$, using the indirect Fourier transformation. SAXS measurements were carried out for several mixtures including the decanoic acid: decanol, 1:1 and 1:2 molar ratio, with different preparation protocols as well as at different temperatures.

4.1.3 Results and discussion

Effect of decanol:decanoic acid ratio

Figure 4-1 displays two scattering profiles of solutions with a total lipid content of 3 wt% (80 mM) in bicine buffer, pH 8.5, at 25°C. To investigate the effect of the ratio of decanoic acid to decanol (DA:DOH), the latter was once chosen to be 2:1 and once 1:1. The scattering profile of the solution with the 2:1 ratio exhibits a plateau at small q-values. This indicates that the species present in the mixture are small enough to be analyzed by SAXS. Contrary, the curve with a higher amount of alcohol (1:1, DA:DOH) shows a higher intensity in this region and an increase towards low q-values. Hence, aggregates lager than suitable for this method are present in the mixture.

Such behavior can be expected, since DA is negatively charged at the pH selected for this study (pH 8.5). Increasing the amount of DA in the mixture is thus expected to hinder self assembly of the lipid molecules, while a higher amount of DOH favors it by screening the negative charges. Therefore, the following temperature- and pressure-dependent measurements were performed on mixtures comprising the 2:1 DA:DOH ratio.

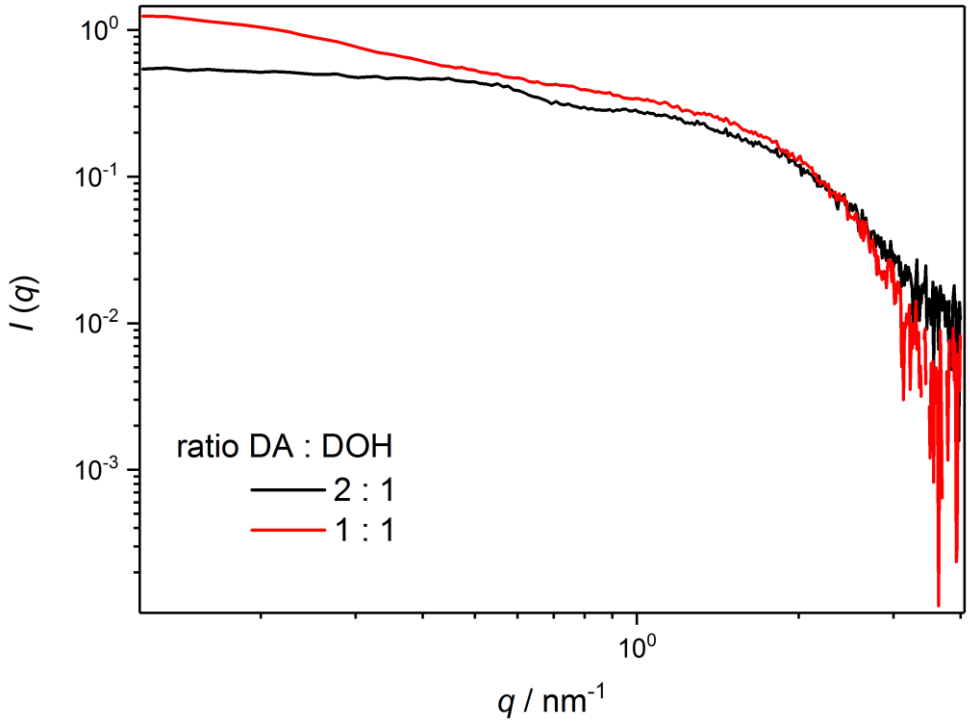

Figure 4-1. Effect of the ratio between decanoic acid and decanol on the scattering profile of the mixture.

Beside the DA:DOH ratio, the effect of extrusion on the system was investigated. Extrusion is a method to homogenize the size distribution of vesicles within a solution. It was found that extrusion hardly had an effect on the scattering curves (Figure A1). This can be explained by the high dynamics of the system, which immediately relaxes to the original micelle-vesicle equilibrium present before extrusion. Extrusion was therefore omitted for the temperature- and pressure-dependent scattering experiments to prevent the loss of lipids.

Effect of pressure

In this section, the changes in the scattering profile of the prebiotic lipid mixture upon compression are analyzed. Figure 4-2 displays patterns of the decanoic acid:decanol system upon compression at 25°C. The absence of Bragg reflections indicates, in agreement with TEM data[65] that the vesicles present in the mixture are unilamellar. At ambient pressure, the distance-distribution function $P(r)$ (Figure 4-3), derived from the scattering intensity data, depicts not only spherical particles with radii of 20 nm and more, but also a significant population of small-sized particles (i.e., micelles), confirming the co-existence of vesicles and micelles in the prebiotic lipid mixture observed in the TEM images.[65]

Upon pressurization, the scattering intensities at small angles increase, indicating formation of more and larger vesicles at the expense of small-sized micelles (Figure 4-2). This behavior is clearly evident by the pressure-dependent changes in the $P(r)$ functions, which show a strong decrease in the micellar population under pressure (Figure 4-3, inset); some selected fits used for the calculation of $P(r)$ are depicted in Figure A2. Hence, we can conclude that pressurization leads to a redistribution of the population of micelles and vesicles, favoring vesicular particles under pressure.

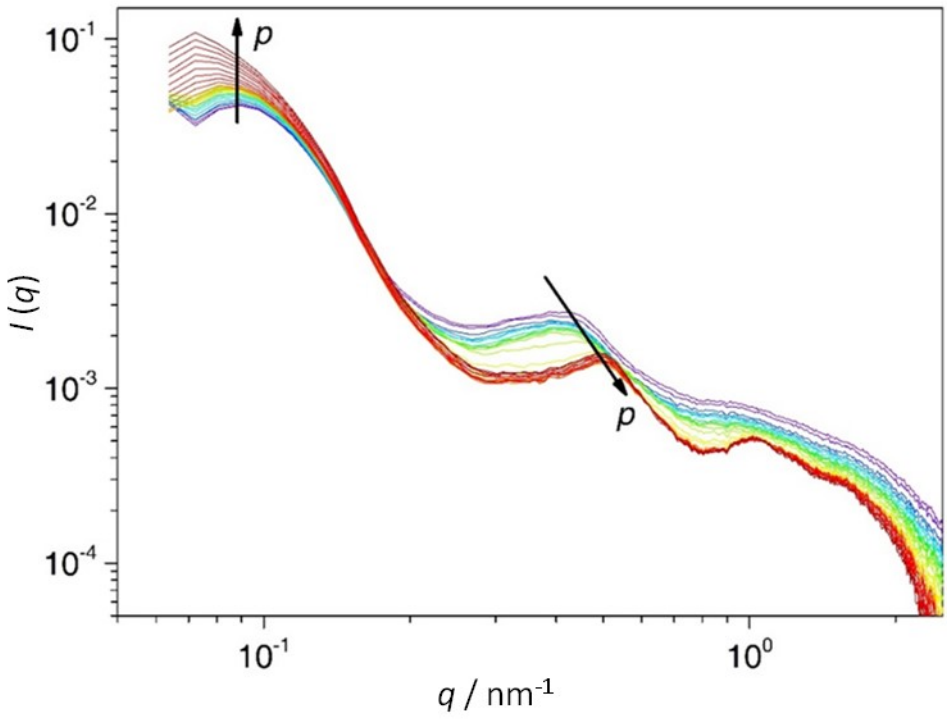

Figure 4-2. Pressure dependent SAXS profiles for the prebiotic lipid mixture comprising decanoic acid : decanol (2:1 molar ratio, pH 8.5) in the range from 0.1 MPa to 250 MPa (step size 10 MPa) at 25°C.

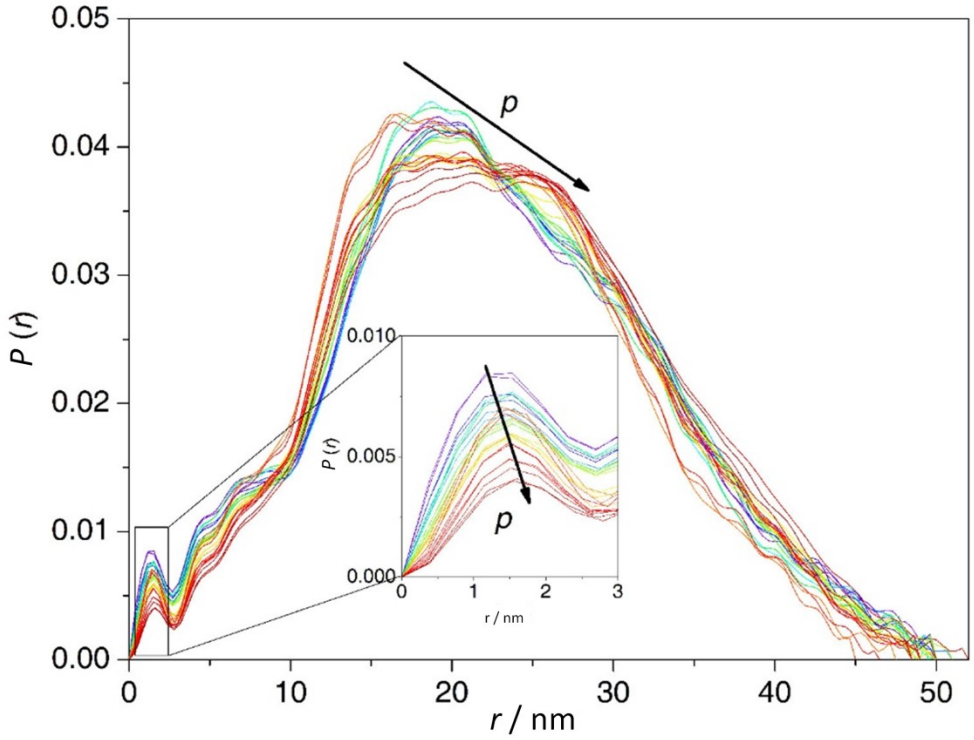

Figure 4-3. The corresponding pair distance distribution functions, $P(r)$, to the scattering profiles displayed in Figure 4-2. Inset: Zoom-in of the changes within the micellar sub population upon compression. Pressure increases the amount of vesicular structures of about 40-100 nm size.

Effect of temperature

Temperature-dependent SAXS profiles of the same system at ambient pressure also show an increase in the scattering intensity at small angles with rising temperature, indicating an increase in larger particles (Figure 4-4). Due to the large size and polydispersity of the vesicles and the limitation in the smaller $q-$range on the SAXSess instrument, a more quantitative analysis employing the calculation of $P(r)$ functions was omitted. Owing to the size limitation of the SAXS technique, complementary dynamic light scattering studies were carried out as well. They confirmed the presence of vesicles and their increase in size and polydispersity with increasing temperature.[65]

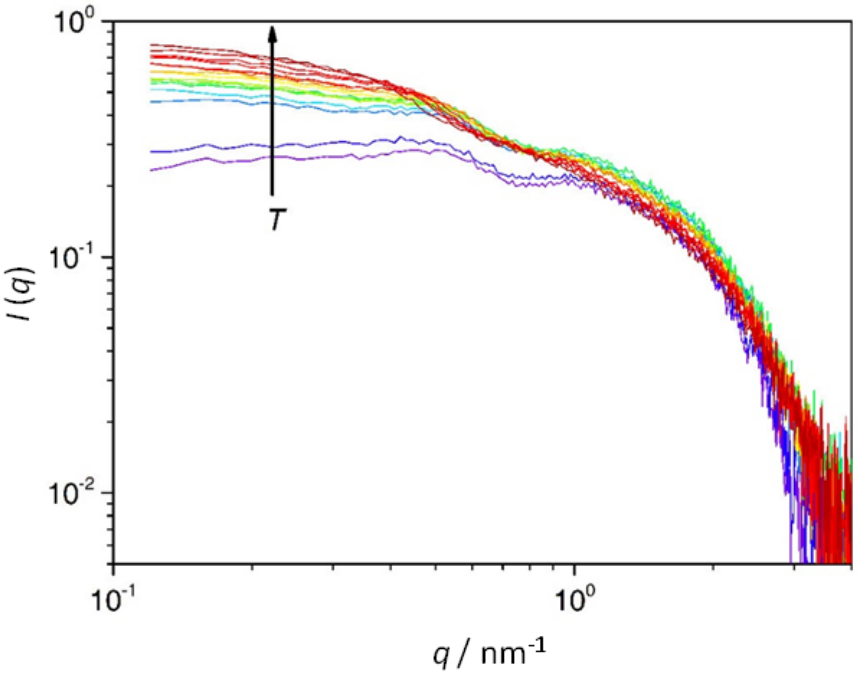

Figure 4-4. Temperature dependent SAXS profiles in the range from 5°C to 75°C (step size 5°C) at ambient pressure (0.1 MPa).

Conclusions

The results show that an increase of the neutral DOH in relation to the negatively charged DA results in lager species, which are too large to be analyzed by SAXS in more detail. The system is so dynamic that extrusion does not have a lasting effect on the size distribution of the species present in it.

In the prebiotic mixture containing 2:1 DA to DOH, SAXS confirmed the coexistence of micelles and unilamelar vesicles. High hydrostatic pressure increases the amount of vesicular structures of short-length fatty-acid-membranes, which can serve as prebiotic membrane envelopes. Complementary laurdan fluorescence, DSC and IR measurements were performed in order to evaluate the fluidity and permeability of such membranes.[65] They showed that even without the complex, highly evolved protein machinery of modern biomembranes, the dynamic nature of fluid fatty-acid-membranes seems particularly well suited for growth, division, and nutrient uptake.[65]

Together with the other methods, the SAXS results permitted the construction of a temperature-pressure stability diagram of the prebiotic lipid mixture.[65] According to

this, fatty-acid-based vesicles are not only highly temperature resistant, but also pressure-stable up to the high pressures reached in the deep sea and sub-seafloor crust. From the view of membrane biophysical chemistry, our results propose that high hydrostatic pressure conditions are highly plausible as planetary environments for the origin of life on Earth.

Our studies also show that pressures in the range encountered in the deep sea could serve as a multifunctional toggle: it limits the flexibility and permeability and therefore reduces the leakage rate of solutes. At the same time, pressure keeps the membrane in a fluid-like state, which is required for its function. Our observations extend the range of tolerable environments for early cell membranes and may add another layer of complexity to developing laboratory models of primitive cell membranes. Such approach to explore laboratory models of primitive cell membranes under extreme environmental conditions aids in better understanding of the evolutionary pathway that led to the first forms of boundary membrane that might potentially isolate a primitive catalytic replicating system from the nutrients required for growth. [217]

4.2 Microemulsions

4.2.1 Introduction

The pressure effects on lyotropic mesophases have been studied mainly on ordered lipid structures in recent years. [2,74,218,219] The effect of conformational disorder and the presence of interfaces (hard and soft matter) on such kind of mesophase transitions is much less explored, though also of high biological and technical relevance. To investigate the effects of disorder and the presence of interfaces, the pressure-response on the structure of a disordered bicontinuous microemulsion at a solid interface was studied by X-ray reflectivity measurements. For comparison, small-angle X-ray scattering was used to analyze the behavior of the bulk solution. Relevant applications range from studies of non-lamellar lipid architectures *in cellulo* at high pressures to strategies aiming at enhancing oil recovery using microemulsions in boreholes.

An important parameter in these studies is the persistent length of the microemulsion, ξ_p , obtained using the Teubner Strey model (Subchapter 2.1.4). It

describes the length over which the film is locally flat, and is given by $\xi_{\mathrm{p}} = l \exp(2\pi\kappa/(k_{\mathrm{B}}\,T))$ where l is the molecular length of the surfactant. [220,221] High ξ_{p}-values indicate flat surfaces, whereas low values are found with highly curved interfaces, which is the case if the bending elastic constant, κ, of the film is as low as of the order of $k_{\mathrm{B}}T$. The results presented here were published in the *Journal of Physical Chemistry B*[31] and are partially reproduced in this chapter with permission from the American Chemical Society, 2016.

4.2.2 Materials and methods

Sample preparation

The distilled water used was of MilliQ purity. *N*-octane was purchased from Fluka (Taufkirchen Germany), the surfactant tetraethylene glycol decanoyl ether, $C_{10}E_4$, was purchased from Bachem (Bubendorf, Switzerland). Equal volumes of water and *n*-octane were combined and a sufficient amount of $C_{10}E_4$ was added to obtain a final concentration of 16 wt% surfactant. All compounds were mixed by vigorous agitation.

The undoped and polished silicon wafers used for the reflectivity measurements with a roughness of 0.3 nm were provided by Wacker Siltronic (Burghausen, Germany). They were cut into pieces of 8×8 mm, rinsed and hydrophilized in a solution of NH_4OH and H_2O_2 (RCA cleaning[222]), and stored in deionized water until usage.

X-ray reflectivity measurements

In the X-ray reflectivity experiment, the specular reflected intensity is measured as a function of the wave vector transfer $q_z = (4\pi/\lambda)\sin(\theta)$ perpendicular to the sample's surface. Thus, only information on the laterally averaged electron density profile is obtained from the XRR data. Depending on the maximum accessible wave vector transfer q_z, the spatial resolution in the z-direction can reach sub-angstroems. The X-ray reflectivities were recorded at beamline BL9 of the Synchrotron radiation source DELTA, Dortmund, Germany, using the 27 keV reflectivity setup.[37] All measurements were performed at a constant temperature of 20°C. A high hydrostatic pressure cell was used, which allows the application of pressures up to 500 MPa.[33] After preparation of the sample, the liquid was filled into the cell and the pressure was raised to 5 MPa, in order to supplant air in the cell. Subsequently, reflectivities were measured at different pressures using a PILATUS 100k detector for photon

detection. In order to characterize the solid substrate, the reflectivity curve with pure water above the silicon wafer was measured. The detected signal was normalized to the incoming photon flux and analyzed using the Parratt algorithm[29] in combination with the effective density model.[30] This evaluation was performed by Dr. Michael Paulus.

Small-angle X-ray scattering measurements

Pressure-dependent SAXS measurements were performed in a home-built high hydrostatic pressure cell with diamond windows[33] at Beamline ID02 at the European Synchrotron Radiation Facility (ESRF) in Grenoble, France. The energy used was 16 keV and the sample to detector distance was 2 m. The samples were exposed to the beam for 0.2 s for each measurement. All measurements were performed at a constant temperature of 20°C. Data were background corrected using the SAXSutilities Package provided by ESRF.[215] The experimental data were fitted according to the Teubner-Strey model[28] using the software SASfit.[223] Pair-distance distribution functions were calculated using the software GNOM of the Atsas software package.[216]

4.2.3 Results and discussion

Near-surface behavior investigated by X-ray reflectivity

XRR was used to investigate the near-surface behavior of the microemulsion. All reflectivity curves show a correlation peak, which shifts to higher q_z-values upon pressurization, as shown in Figure 4-5. This correlation peak can be attributed to a (disordered) lamellar phase whose domain size of alternating lamellar arrangements,[78,79] $d_{\mathrm{surface}} = 2\pi/q_0$, can be derived from the position of the correlation peak, q_0. The size of the domains within the lamellar phase is compressed from about 15 nm at near-ambient pressure (5 MPa) to 12 nm at 400 MPa. The corresponding compressibility of the lamellar lattice, $\mathrm{d}d_{surface}/\mathrm{d}p$, amounts to 0.01 nm MPa^{-1}.

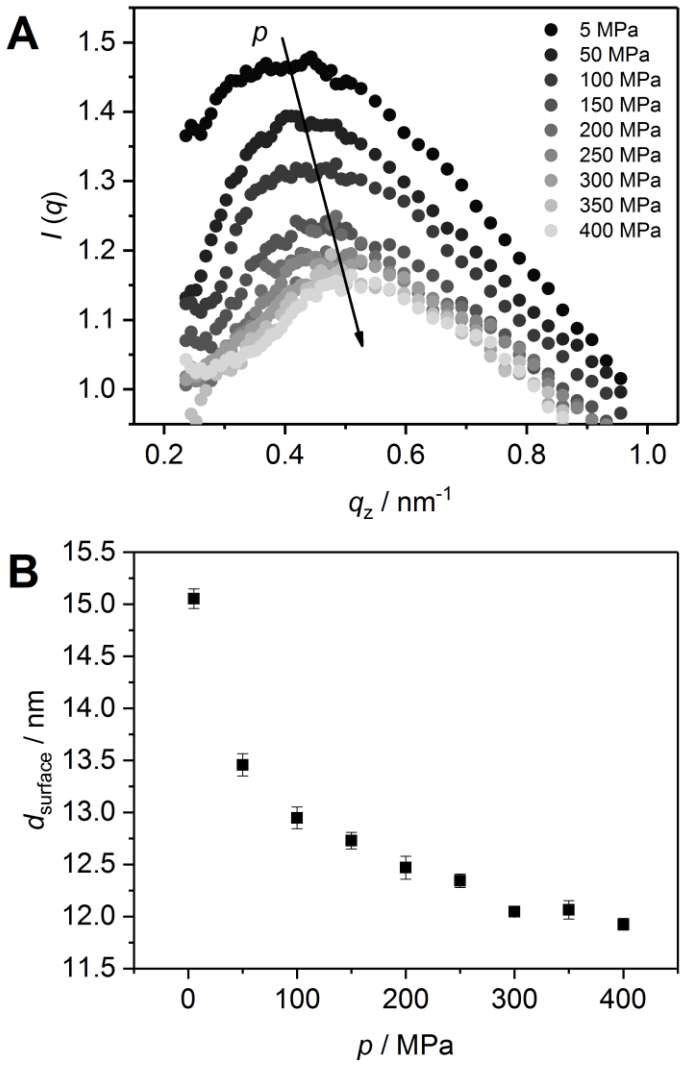

Figure 4-5. (A) Correlation peaks extracted from X-ray reflectivity measurements of the microemulsion consisting of equal volumes of water and *n*-octane and 16 wt% $C_{10}E_4$ near the surface of a hydrophilic Si-wafer at different pressure conditions. The position of the correlation peak associated with the lamellar phase, q_0, shifts towards higher q_z-values upon pressurization. (B) Decrease of the corresponding size of the alternating arrangements of water and oil, $d_{surface} = 2\pi/q_0$, with pressure. Error bars were derived from Gaussian fits to determine the position of the peak maximum, q_0.

Corresponding real-space electron density profiles (EDP) were calculated using the Parratt algorithm[29] to fit the reflectivity curves at selected pressures (50, 200 and 400 MPa), as can be seen in Figure 4-6. In order to determine the electron density profiles, we fitted the entire q_z-range from 0.2 nm^{-1} to 6 nm^{-1}. Such wide q-range is needed to obtain the EDP with sufficient accuracy. The location of the Si wafer with the highest electron density is defined as $z = 0$ nm. A thin layer with the electron density of water (~ 0.8 nm, 2-3 layers of H_2O) is visible in direct proximity to the hydrophilic Si-surface. A similar water layer was also found previously at the liquid-air

interface of a comparable system.[79] In contrast, in direct proximity to a hydrophobic interface, an oil layer was observed.[224] Thicker layers of alternating water and oil domains close to the surface of the Si wafer are visible as oscillations in the electron density profile (corresponding to about three layers), which approach the electron density of the bulk solution at a distance of about 45 nm away from the surface for the EDP at 5 MPa. This distance, which can be regarded as the correlation length of the lamellar interface, $\xi_{surface,}$ decreases slightly with pressure, which is in good agreement with the compression of the layers discussed above. Neutron reflectivity studies found that $\xi_{surface}$ of the lamellar phase is about 30 nm at atmospheric pressure,[78] which is in a similar range as the correlation length of the hydrophilic surface-induced lamellar interface found in our experiments.

The overall electron density close to the surface is significantly lower than in the bulk solution about 50 nm away from the surface. This is probably due to a laterally extended surfactant/oil layer close to the interface, and is a consequence of the ordering effect the hydrophilic interface imposes on the arrangement of the surfactant molecules, which are supposed to bind to the wet hydrophilic solid interface by their hydrophilic headgroups. With increase distance, z, from the surface, lamellar ordering is reduced, finally vanishing after about 2-3 water-oil layers. The increased disorder is most likely due to the fact that the lamellae get increasingly perforated, leading to an increase of the electron density, which approaches the bulk value of the microemulsion beyond about 45 nm.

With increasing pressure, the maxima of the oscillations in the EDP shift toward the surface, indicating marked compression of the lamellar layers, which is probably due to the about 3-fold larger compressibility of *n*-octane compared to water (isothermal compressibility $\kappa_T(\mathrm{water})$ = 0.459 GPa^{-1}, κ_T (n-octane) = 1.282 GPa^{-1} at room temperature and ambient pressure[225–227]). The density increase of the system upon compression is also reflected in the overall increase of the electron densities observed in the EDPs. Interestingly, we did not find an increase in the number of near-surface layers at high pressures.

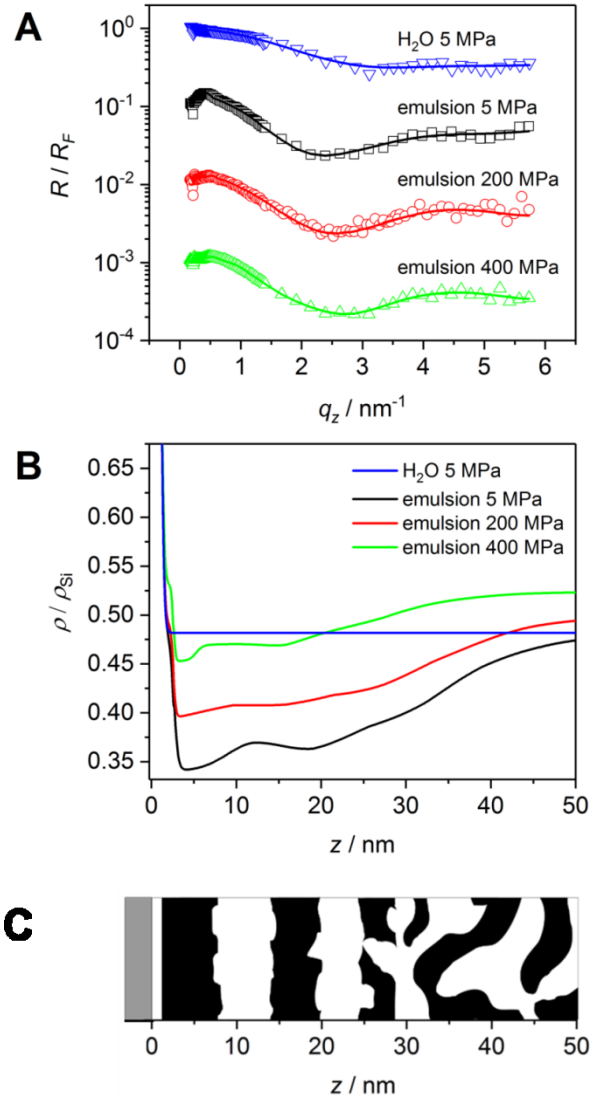

Figure 4-6. (A) Fits according to the Parratt algorithm[29] to the experimental X-ray reflectivity data of water at 5 MPa and of the microemulsion near the surface of a Si-wafer at 5 MPa, 200 MPa and 400 MPa to determine electron density profiles. Curves were shifted for clarity. (B) Corresponding real-space electron density profiles. The oscillations in the electron density reflect the alternating water/oil domains, which are compressed by applying pressure. (C) Illustration of the water (white) and oil (black) domains based on the electron density profile of the emulsion at 5 MPa.

Bulk-behavior investigated by SAXS

Within the bulk phase, the pressure-dependent structure of the bicontinuous microemulsion was determined by small-angle X-ray scattering (Figure 4-7). All scattering intensity profiles show a broad correlation peak at scattering vector q_0, which shifts to higher scattering angles upon pressurization, indicating a decrease of the domain size of the bicontinuous phase. No phase transition to a different mesophase structure is observed up to 400 MPa. The data were further analyzed by

fitting the results to the Teubner-Strey model.[28] The overall quality of the fits decreases with increasing pressure. However, in the region of the correlation peak, the fits are of sufficient accuracy that the parameters for the average domain spacing in the bulk, $d_{\mathrm{m,bulk}} \approx 2\pi/q_0$, and the correlation length, $\xi_{\mathrm{m,bulk}}$, which characterizes the decay of local order, can be derived. The suffix "m" characterizes the bicontinuous microemulsion structure. As expected, at large q, the Porod law $I(q) \propto q^{-4}$ indicates a sharp water-oil interface.

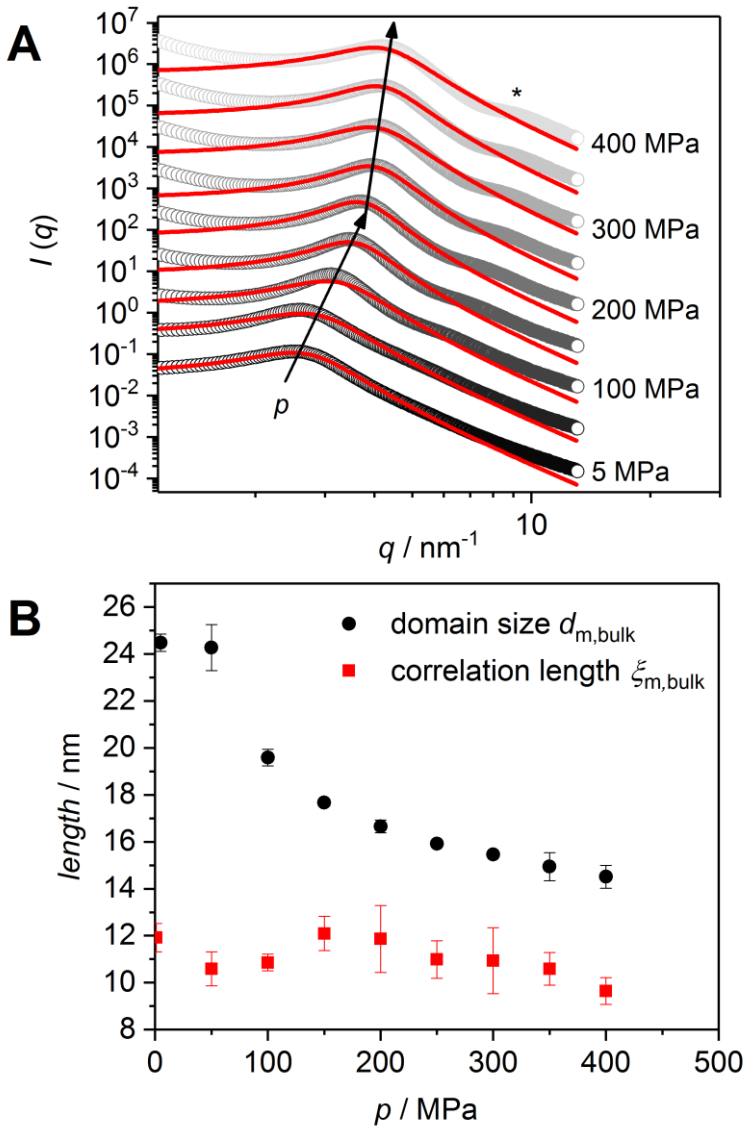

Figure 4-7. (A) Bulk scattering intensity profiles, $I(q)$, of the bicontinuous microemulsion at different pressures in double-logarithmic representation. Red solid lines indicate fits according to the Teubner-Strey model.[28] Second-order peaks arising under pressurization are indicated by an asterisk. Curves were shifted for clarity. (B) Pressure-dependent changes in the domain size, $d_{\mathrm{m,bulk}}$, and correlation length, $\xi_{\mathrm{m,bulk}}$, of the bicontinuous microemulsion derived from fits using the Teubner-Strey model. The decrease of $d_{\mathrm{m,bulk}}$, reveals a high compressibility of the domains, while the correlation length $\xi_{\mathrm{m,bulk}}$, i.e. the coherent length of the local periodic domain structure, does not change markedly. Error bars are standard deviations from the evaluation of three independent measurements.

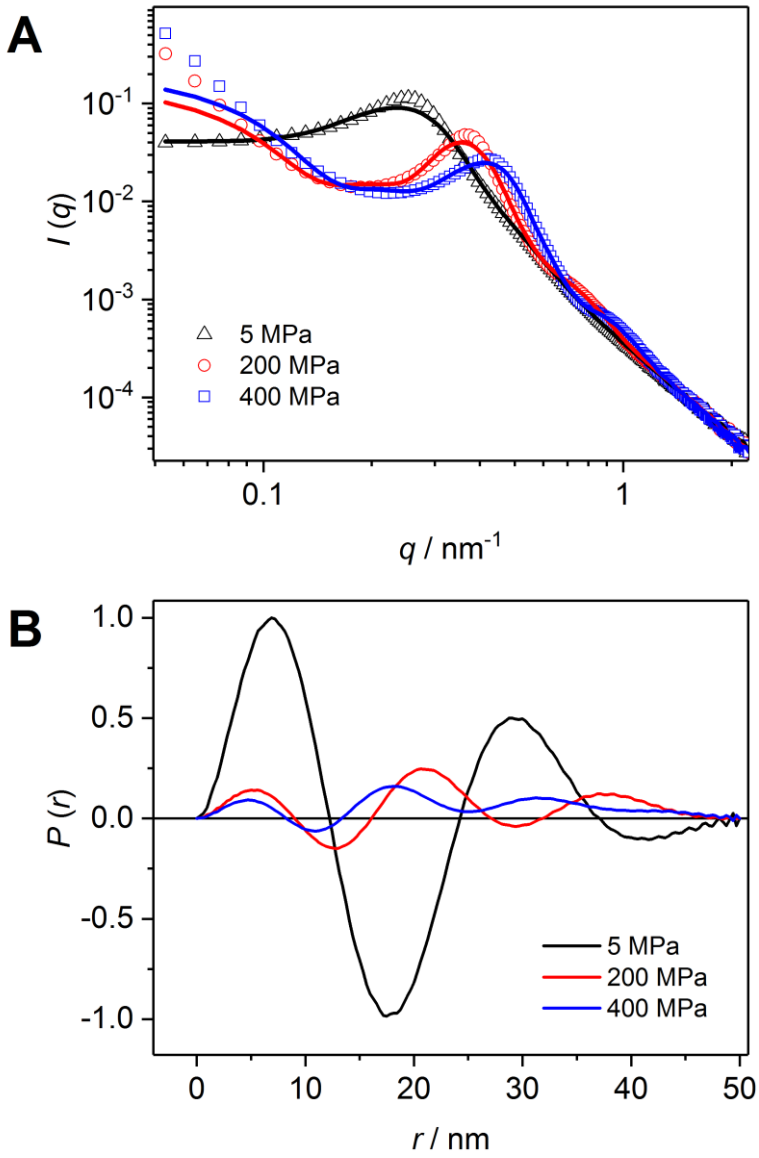

Figure 4-8. Pressure-dependent changes in the real-space pair distance distribution functions, $P(r)$, of the bulk phase of the microemulsion derived from the SAXS data by indirect Fourier transformation. (A) Experimental data (open Symbols) with according fits (solid lines). (B) $P(r)$ functions obtained by indirect Fourier transformation.

The domain size decreases from about 24 to 14 nm upon pressurization, which is in good agreement with the domain size derived directly from the position of the correlation peak ($2\pi/q_0$) and the pair distance distribution function, $P(r)$, calculated by indirect Fourier transformation (Figure 4-8). Most of the compression takes place in the pressure regime between 50 and 200 MPa, in which the $d_{m,bulk}$ value decreases from 24 to 16 nm, its compressibility, $\mathrm{d}d_{m,bulk}/\mathrm{d}p$, amounting to 0.04 nm MPa^{-1}. At higher pressures, the domain size of the bicontinuous phase gets only slightly more compressed, about 1 nm between 200 and 400 MPa,

corresponding to a $\mathrm{d}d_{\mathrm{m,bulk}}/\mathrm{d}p$ value of 0.01 nm MPa^{-1}. The overall decrease of the compressibility of the domain structure upon compression is reminiscent to that of single component bulk liquids.[228] In comparison to the domain size, the change in the correlation length, $\xi_{\mathrm{m,bulk}}$, with pressure is relatively small. The value for $\xi_{\mathrm{m,bulk}}$ is about 11 nm throughout the whole pressure range covered. At 5 MPa, this value is about $d_{\mathrm{m,bulk}}/2$, indicating correlations only between nearest neighbor domains. The compression of the domain size in combination with the essentially constant correlation length leads to a marked change in the ratio between $d_{\mathrm{m,bulk}}$ and $\xi_{\mathrm{m,bulk}}$ with increasing pressure.

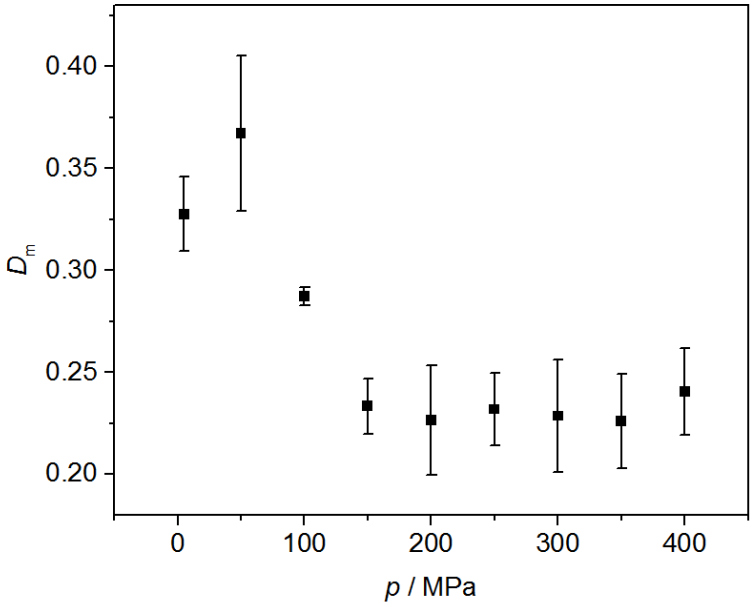

Figure 4-9. Decrease in the disorder parameter D_{m} of the bulk phase of the microemulsion with pressure. Error bars are standard deviations from three independent measurements.

The parameter $D_m = d_{\mathrm{m,bulk}}/(2\pi\,\xi_{\mathrm{m,bulk}})$, which is a measure of the disorder in the system (disorder parameter),[77,228] experiences a significant decrease up to 200 MPa (Figure 4-9), from 0.33 to 0.22, i.e., the structural order of the system increases with pressurization. The appearance of a slight second order correlation peak at $2q_0$ in the scattering curves (Figure 4-7) supports this observation. The overall bicontinuous structure remains preserved, however. These findings are in agreement with the observation that the surfactant monolayers become more rigid with increasing pressure as revealed by neutron spin echo (NSE) experiments for a similar system.[229] This can be attributed to a decreased flexibility in the hydrophobic part of

the surfactant molecules. At much higher pressures, the increase in bending modulus of the interface and a marked decrease of the packing parameter - the ratio of the volume of the surfactant molecule and the product of the area of the polar head group and the tail length - might still lead to a phase change to a lamellar phase, however.

Thermal undulations of the soft elastic sheets of the BME exhibit an increase of their amplitude with rising temperature. Concomitantly, such undulation forces should decrease when the bending modulus increase and the packing parameter of the surfactant is reduced. Therefore, it can be expected that an increase of pressure can induce the transition from a bicontinuous to a lamellar structure, also of near-surface lamellar ordering. However, a freezing-in of the thermally excited long-wavelength modes due to an increased bending modulus upon compression of the system would reduce the entropy associated with these thermal excitations and lead to an increase in free energy. Therefore, the entropy term seems to outweight the increase in bending energy also at high pressures, which prevents the system from undergoing a phase transition to a more ordered lamellar phase - at least in the pressure range covered in these experiments.

Conclusions

To summarize, our results show that bicontinuous microemulsions form a thin lamellar phase close to hydrophilic interfaces, and this layer persists upon compression. Due to the wide q_z-range covered in the XRR measurements, we could analyze the electron density profile in the proximity to the hydrophilic solid-liquid interface in detail. About 2-3 lamellar layers could be resolved, displaying increasing disorder with increasing distance from the solid interface. We found that the lamellar domains are compressed with increasing pressure and that the correlation length of lamellar order does not change markedly with pressure.

The SAXS measurements on the bulk microemulsion phase revealed an increased order of the bicontinuous phase upon pressurization. However, no phase transition is observed up to 400 MPa. While pressure has been shown to cause the formation of highly ordered lamellar phases from ordered bicontinuous cubic lipid phases, such scenario is not observed for the disordered BME system studied here. High pressure

leads to an increase of the stiffness and hence the bending modulus of the interfacial layer, but this is not sufficient to overcome the loss in conformational entropy that would result from a phase transition to a more ordered lamellar phase. Our observations might have several implications, ranging from pressure effects on emulsions in deep subsurface oil recovery, up to biologically relevant problems dealing with lamellar-to-non-lamellar phase transitions in organisms thriving in the deep sea, where pressures up to the 100 MPa pressure level and beyond are encountered.

5 Investigations of nucleic acids

This chapter is divided in four subchapters. It starts with the exploration of single nucleotides (guanosine monophosphate sodium salt) with a very complex self-assembly behavior. After this, a small RNA hairpin representing a very common structural motive in RNA, is analyzed. In the following, the investigations focus on the step from RNA towards proteins. Structural investigations on the phenylalanine transfer RNA, connecting the RNA and the protein world within contemporary cells, were performed. Finally, the hairpin ribozyme, RNA with enzymatic activity, is analyzed. These molecules are regarded as precursors of modern enzymes.

5.1 Self-assembly of guanosine monophosphate sodium salt

5.1.1 Introduction

Guanosine monophosphate (GMP) molecules can self-assemble in water to form tetramers, which can stack to form four-stranded helical structures. This structurally complex system consisting of relatively simple molecules was exploited as a model system in order to gain a deeper understanding on the self-assembly of nucleotides under extreme conditions of temperature and pressure like in the primordial soup. We explored the effect of osmotic pressure, temperature and cosolutes, such as salts and trimethylamine *N*-oxide (TMAO), on the pressure-dependent dissociation of GMP tetramer stacks. Synchrotron small-angle X-ray scattering was employed to determine the dimensions of the species present in the GMP solutions.

In the presence of high salt concentrations, the cylindrical GMP tetramer stacks self-associate to form a hexagonal lyotropic phase. The pressure-dependent changes in the hexagonal lattice constant of this phase in the absence and presence of cosolutes and at different temperatures was analyzed using Synchrotron X-ray diffraction in a home-built high pressure cell with diamond windows. The project was performed in collaboration with Mimi Gao and Rana Seymen (TU-Dortmund, Germany), who helped to prepare the samples and performed FTIR and DLS measurements on the system. The group around Catherine Royer (Troy, NY, USA) performed corresponding high-pressure NMR measurements.

A manuscript for publication containing the SAXS measurements on the self-assembly of GMP-Na_2 in pure water at different temperatures and pressures has been submitted.[230]

5.1.2 Materials and methods

Guanosine 5'-monophosphate disodium salt hydrate (>99% purity), potassium chloride (KCl), trimethylamine *N*-oxide (TMAO) and poly(ethylene glycol) with an average molecular weight of 20 kDa (PEG 20 kDa) were all purchased from Sigma Aldrich (Munich, Germany). GMP was allowed to dissolve in H_2O overnight at room temperature in order to give a stock solution with a concentration of 35 wt%. The stock solution was filtered using a 0.2 µm filter. The exact concentration was then determined by UV absorption at a wavelength of 260 nm using an extinction coefficient of 10674 M cm^{-1} [231]. Cosolute stock solutions were 3 M for KCl, 4 M for TMAO and 30 wt% of PEG 20 kDa. Appropriate volumes of the GMP stock solutions and the cosolute stock solutions were then mixed in order to obtain the final concentrations given in Table 5-1.

Table 5-1. Compositions of the GMP-samples investigated and according temperatures.

***c*(GMP) / M**	***c*(KCl) / M**	***c*(TMAO) / M**	***c*(PEG 20 kDa) / wt%**	***T* /°C**
0.48	-		-	7, 25, 35
0.48	1			7, 25, 35
0.48	-	2		25
0.48	1	2		25
0.48	-	-	15	25
0.48	1	-	15	25

All measurements were performed at the ESRF beamline ID 02 (Grenoble, France) in a home-built high pressure cell with diamond windows.[32] The sample volume was 10 µL. The energy used was 16 keV and the sample to detector distance was 2.4 m. The samples were exposed to the beam for 0.25 s for each measurement. No radiation damages were detected within the total exposure time of a complete pressure series. The diffraction data was background corrected and analyzed using

the SAXSutilities[215] software package provided by the ESRF. For the samples where the hexagonal phase gave origin to Bragg-peaks, the peak maxima were obtained from Gaussian fits using the software Origin and were used to derive the hexagonal lattice constant, d_{hex}. For the measurements at 7°C, the accessible pressure range was limited to 400 MPa due to an increased rigidity of the O-ring seals at these cold temperatures causing leakage of the high pressure cell.

5.1.3 Results and discussion

Pressure-dependent changes at different temperatures in pure water

The pressure dependent self-assembly of Na_2GMP was investigated at three different temperatures (7°C, 25°C and 35°C) in the absence and presence of 1 M KCl (Figure 5-1). In the absence of further stabilizing cations, there is an intrinsically high polydispersity within the system, since monomers, dimers, quartets and helical stacks are present in an equilibrium. The evaluation of these data is thus only performed in a qualitative manner.

In pure water, low temperatures (7°C) favor the self-assembly of Na_2GMP to form helical stacks as can be seen in Figure 5-1A. These are reflected in the scattering profiles as overall high intensities associated with larger species, probably helical stacks. As can be seen from a slight decrease in intensity with pressure, the latter seems to foster the dissociation of larger to smaller species. At an elevated temperature of 25°C and atmospheric pressure, the intensities observed in the scattering profiles are slightly lower, indicating a shift towards smaller species within the equilibrium of the mixture, probably caused by dissociation of the helical stacks with rising temperature. With increasing pressure, the loss in overall intensity is much more pronounced than at 7°C. Thus, an increase in temperature seems to lower the pressure stability of the helical stacks. At 35°C, the overall low intensity of the scattering profile suggests the presence of smaller species, only. The corresponding FTIR and NMR measurements[230] revealed that the base pairing is interrupted, while the stacking interactions remain intact. Taken together with this information about the effect of pressure on the interactions operative in the helical stacks, the observed effect might lead to the conclusion that the helical stack consisting of quartets dissociates to become four thin strands of stacked monomers, explaining the

lowering of intensity observed in the SAXS measurements. This can be expected, since stacking interactions are generally stabilized by pressure. [90,91]

Pressure-dependent changes at different temperatures in 1 M KCl

In the presence of 1 M KCl, the stabilizing effect of monovalent cations induces a hexagonal phase, giving rise to Bragg-reflections (Figure 5-1 B,C). At the coldest temperature investigated, i.e. 7°C, one peak is observed at a q-position of 2.25 nm^{-1}. This peak can be attributed to the q_{10} hexagonal phase.[115] In contrast to the work by *Ausili et al*., further peaks of the hexagonal phase are not observed here, which might be explained by the relatively low Na_2GMP concentration of the sample (0.48 M, ~20 wt%).

With increasing pressure, the peak shifts from 2.25 nm^{-1} to 2.10 nm^{-1}, but persists even at pressures as high as 400 MPa. Thus, the dimension of the hexagonal unit cell, d_{hex}, increases from about 3.2 nm at 0.1 MPa to 3.5 nm at 400 MPa. No dissociation is observed at these high pressures, which would be indicated by a broadening and decrease in intensity of the peak. Further, there is a linear correlation between the lattice constant and the applied pressure. These results are in good agreement with those found by *Ausili et al.* [115] Interestingly, this group also found that the tetramer repeat distance decreases concomitantly with pressure with up to 0.3 nm GPa^{-1}. However, the limited q-range of the high pressure cell used did not permit to analyze the changes in this tetramer repeat distance with pressure.

At 25°C, the dimension of the hexagonal unit cell increases and cylinders start to dissociate at high pressures (> 400 MPa), as can be seen from a slight decrease in intensity of the peak at higher pressures. Until there, d_{hex} behaves very similar as observed for 7°C. In contrast, at 35°C the dimension of the hexagonal unit cell increases more drastically with pressure. In addition to that, the strong decrease in the peak intensity indicates a dissociation of the hexagonal phase until no peak is observed anymore. Like for all measurements, two independent experiments were performed. In the first series, the diffraction peak disappeared at 250 MPa (Figure 5-1 B) and in the second series at 450 MPa (open symbols in Figure 5-1 C), respectively. The difference between these two apparent critical pressures might be explained by a slightly higher concentration of the hexagonal phase present within the second sample, increasing the overall intensity and stability of the hexagonal phase. As can

be seen from Figure 5-1 C, for the second sample, the correlation between d_{hex} and pressure is not completely linear between 250 MPa and 450 MPa, but a divergence is observed. Such a divergence of the d_{hex}-values upon approaching a critical pressure value, p_c, can be interpreted as an unbinding transition, which has been observed in other soft elastic manifolds, including stacks of lipid bilayer membranes[232–234] and actin bundles[213] (Subchapter 6.3). The origin of such a transition could be the competition of attractive molecular interactions and an effective repulsion between the helical stacks within the hexagonal phase.

All in all, in 1 M KCl an increase of temperature and also of pressure has a destabilizing effect on the hexagonal assembly of the cylindrical stacks. The interactions between the cylindrical stacks within the hexagonal phase are dominated by electrostatic interactions between the negatively charged phosphate groups of the nucleotides with the positively charged monovalent cations. This type of interaction is weakened by increasing temperature due to entropic reasons as well as by pressure due to the electrostrictive effect.[87–89]

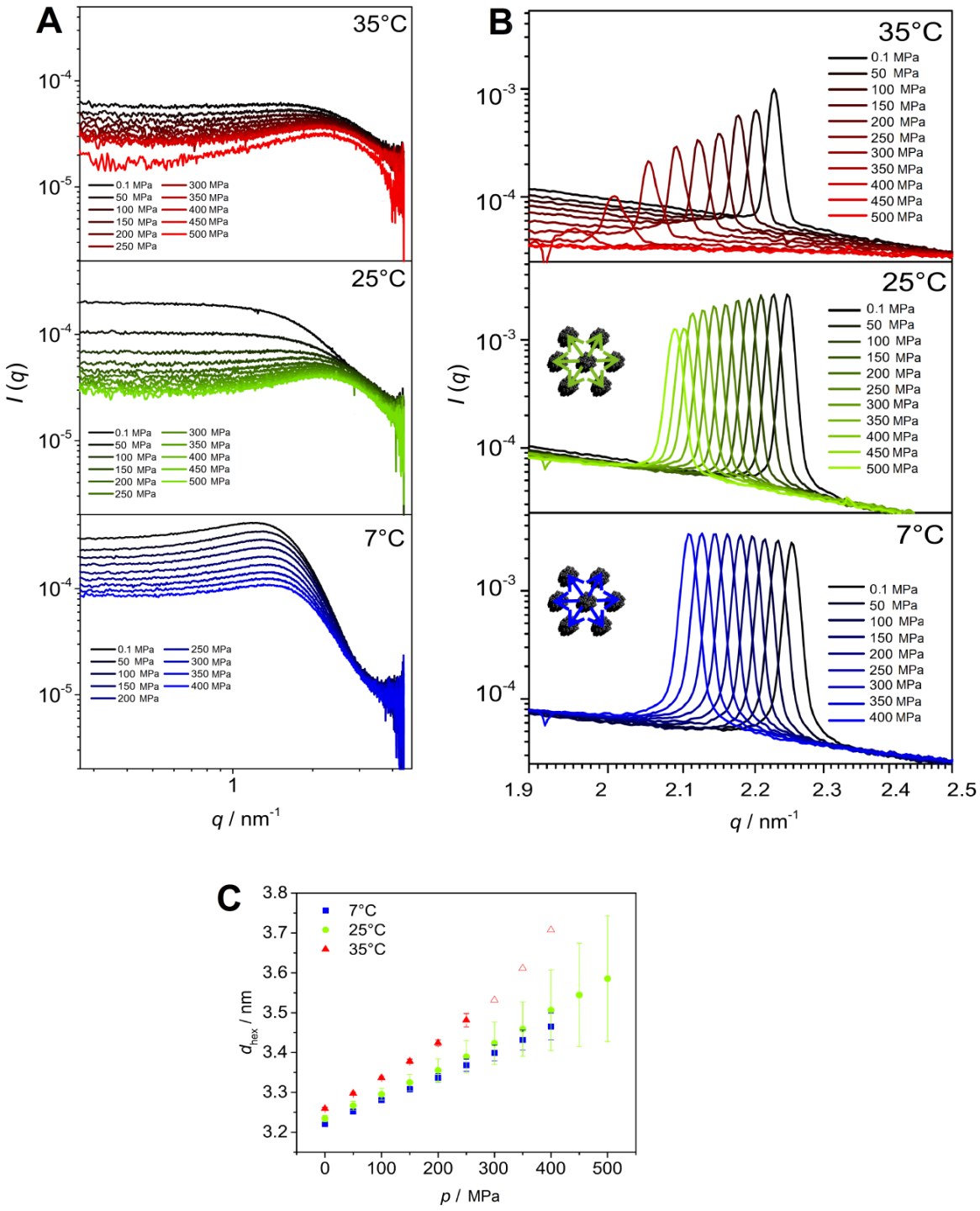

Figure 5-1. SAXS intensity profiles of 0.48 M GMP in H_2O as a function of pressure in the absence (A) and presence (B) of 1 M KCl and the hexagonal unit cell dimensions (C) derived from the peaks observed in (B). Error bars are derived from two independent measurements. For the open symbols, the peak was only present in one of the series, thus no error bar is given.

Pressure-dependent changes in the presence of 2 M TMAO

Interestingly, 2 M TMAO is able to induce the hexagonal phase even in the absence of salt, as can be seen in Figure 5-2 A, E. This phase has an about 0.1 nm lower d_{hex} than the hexagonal phase induced by 1 M KCl. This phase is very labile to pressure, so that at p > 200 MPa the peak is not observed anymore, i.e. the helical stacks are no longer hexagonally packed. The ability of TMAO to induce a hexagonal phase in the absence of salt can be explained by the preferential hydration effect induced by TMAO.[44] Unfavorable interactions of TMAO with all GMP surface types (nucleobase, phosphate, sugar), but especially with the phosphate induce greater hydration of the GMP stacks. At atmospheric pressure, self assembly is favored in order to minimize surface from which TMAO is excluded. Rising pressure induces dissociation of the hexagonal phase due to the electrostrictive effect.[87–89] The dissociation increases the surface area exposing the negatively charged phosphate backbone at which the water molecules can be packed more densely than in the bulk.

In the presence of 2 M TMAO and 1 M KCl (Figure 5-2 B, E), the dimension of the hexagonal unit cell is smaller and increases less with pressure than in pure 1 M KCl at 25°C. No dissociation is observed in the pressure range up to 500 MPa. This further underlines the stabilizing effect of the TMAO on the hexagonal phase.

Pressure-dependent changes in the presence of 15 wt% PEG (20 kDa)

The presence of 15 wt% PEG (20 kDa) has a stabilizing effect on the cylindrical stacks, which, in contrast to pure water, do not dissociate completely under pressure at 25°C. Even at the highest pressure investigated, i.e. 500 MPa, the intensity of the scattering curves still indicates the presence of lager species, as can be seen from Figure 5-2 C. The pronounced correlation peak at about 1.5 nm^{-1} indicates an increase in repulsion between the cylinders, which can be attributed to the excluded volume effect.[235] The negatively charged surface of the stacks is the origin of this repulsion, whereby the bulky PEG molecules limit the volume available to cylindrical stacks limiting the distance between them. Thus, the stacks are stabilized and arrange in a regular distance giving rise to a correlation peak in the scattering profile. Dissociation of the stacks is prevented by the crowding effect, since smaller fragments would occupy a larger volume than the cylindrical stacks.

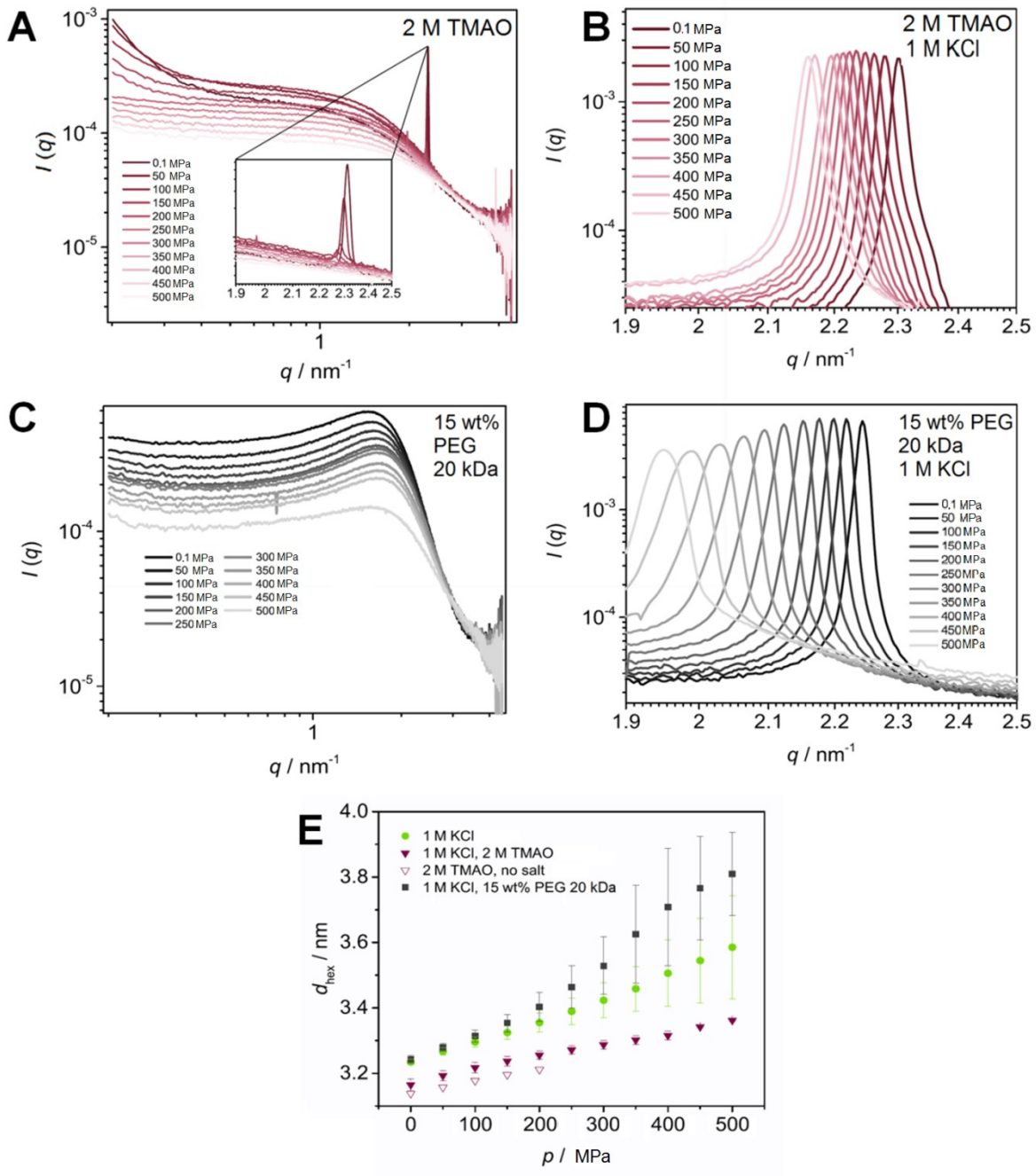

Figure 5-2. SAXS intensity profiles of 0.48 M GMP in an aqueous solution of 2 M TMAO (A,B) or 15 wt% PEG 20 kDa (C,D) as a function of pressure. Samples were analyzed in the absence (A,C) and presence (B,D) of 1 M KCl. From the peaks observed in (A, B, D), the hexagonal unit cell dimensions were derived and plotted as a function of pressure. All measurements were performed at 25°C. For comparison, the hexagonal unit cell dimensions in 1 M KCl at 25°C (Figure 5-1 C) are also displayed.

In contrast, the hexagonal phase formed in the presence of 1 M KCl is destabilized by the presence of 15 wt% PEG (20 kDa). It is more labile to pressure in comparison to the pure salt solution. The increase in the lattice constant with pressure is more pronounced. The broadening of the Bragg-peak with pressure indicates a disordering of the hexagonal phase. This might be explained by the increased repulsion of the stacks due to the excluded volume effect, which is reflected in the correlation peak in the absence of salt. Since pressure is weakening electrostatic interactions,[87–89] the attractive interactions are weakened with increasing pressure. The correlation peak observed in the absence of salt (Figure 5-2 C) supports this hypothesis. Since pressure is weakening electrostatic interactions,[87–89] the attractive interactions are weakened with increasing pressure. This leads to repulsion and a concomitant increase in the distance between the stacks and finally to the onset of dissociation of the hexagonal phase.

Conclusions

At low temperatures, as present in the deep sea, GMP can form cylindrical stacks, which are stable up to the pressures found in these habitats. In the presence of excess cations, the negatively charged cylindrical stacks assemble to a hexagonal phase. Pressure weakens electrostatic interactions and thus can lead to dissociation of this hexagonal lyotropic phase.

Certain cosolutes, such as TMAO and PEG (20 kDa), can favor the assembly of quartets to cylindrical stacks and stabilize them against pressure, even at higher temperatures. TMAO has been shown to induce the assembly to a hexagonal phase even in the absence of excess cations, which might be explained by the stronger hydration of GMP and the reduced accessible surface area of this phase. PEG has been shown to increase the repulsive interaction between the cylindrical stacks. Due to the reduced volume, the cylindrical stacks are forced to be in closer proximity to each other, leading to an increase in repulsive interactions, visible as correlation peak.

At ambient pressure, 1 M KCl is able to compensate this repulsion by additional attractive electrostatic interactions. However, the electostrictive effect of pressure leads to a decrease in the pressure stability of the hexagonal phase and finally to dissociation of the cylinders. Thus, we showed that at cold temperatures cylindrical

GMP-stacks exist up to pressures as high as 400 MPa and can be further stabilized by the presence of cosolutes. Self-assembled Na_2GMP could be stable at conditions found in the primodal soup and thus could have served as precursors for the first linked RNA structures.

5.2 Small RNA hairpin

5.2.1 Introduction

After the self-assembly of small nucleotides was investigated in the previous chapter, this chapter deals with the influence of temperature and pressure on a small common RNA motif, the small RNA hairpin. It is highly important to understand the thermal and pressure stability of fundamental RNA structures in thermophilic and piezophilic organisms because the adaptation mechanisms of these organisms living under particular harsh conditions are still largely unanswered. This can be achieved by revealing the free energy and conformational landscape of these structures, and exploring the forces controlling their stability.

The aim of the study presented here is to analyze conformational changes of the labeled RNA tetraloop gcUUCGgc over a wide range of temperatures and pressures using small-angle X-ray scattering experiments as well as FRET, UV-Vis and FTIR spectroscopy, and to compare the results with theoretical predictions. To ensure comparability with the fluorescence measurements, SAXS measurements were also preformed on the small RNA hairpin labeled with two fluorophores. Their chemical nature is built from two indole rings that are connected by a polymethine chain. Cy3 serves as the donor fluorophore and Cy5 as the acceptor in the FRET assay. These measurements under various conditions of temperature and pressure should also help to answer the question to what regard the fluorophores influence the stability of the small hairpin. The results of these investigations were published in the journal *Biophysical Chemistry*.[236]

5.2.2 Materials and methods

The small RNA hairpin (sRNAh) molecule used in this study has a 5'-gcUUCGgc-3' sequence. Since this study had the aim to complement FRET experiments, the RNAh has two fluorescent dyes attached, Cyanine 3 phosphoramidite (Cy3) and Cyanine 5 phosphoramidite (Cy5) to the 5' and 3' ends of the sequence, respectively. The small

RNA was synthesized by IBA Life Solutions for Life Science GmbH (Goettingen, *G*ermany), and was received as lyophilized powder. The sRNAh was suspended in nuclease-free water to obtain a 0.1 mmol μL^{-1} solution and stored at -80 °C. The samples were lyophilized to remove H_2O, and then suspended in pure 50 mM TRIS-HCl buffer + 0.1 mM ethylenediaminetetraacetic acid (EDTA), pH 7.5. Nuclease-free water, pipette tips, microfuge tubes, conical tubes and RNase AWAY® reagent were obtained from Ambion® (Life Technologies) and were used for all experiments.

All measurements were performed at the European Synchrotron Radiation Facility (ESRF), beamline ID 02 using a home-built high-pressure cell with diamond windows[33]. Samples of the labeled sRNAh were prepared at a concentration of 20 mg mL^{-1} in 50 mM Tris-HCl-buffer+ 0.1 mM EDTA, pH 7.5. The data was processed and background corrected using the software SAXSutilities[215] provided by the beamline. Pair-distance distribution functions, $P(r)$, were calculated using the software GNOM, modelling using the software GASBOR of the Atsas software package. [216]

5.2.3 Results and discussion

The structural changes of the sRNAh with the fluorophores were investigated for various conditions of temperature and pressure. Figure 5-3 shows the changes in the radius of gyration of the small molecule as derived from the Guinier approximation. At 20°C and 0.1 MPa, the eight nucleotide construct with the fluorophores has a radius of gyration of about 1.45 nm, which is at the lower end of the size range accessible by SAXS. However, this very small size gives rise to a large linear section in the Guinier plots, so that the slope of this section, from which the radius of gyration is derived, can be determined with sufficient accuracy. The scattering profiles from which this data was derived can be found in Figure A5 to Figure A7 in the Appendix. With increasing temperature, the radius of gyration decreases slightly from about 1.43 nm to 1.27 nm. In contrast to this, rising pressure leads to an increase of this value. This increase becomes more pronounced with rising temperature. At about 400 MPa, all curves converge against a radius of gyration of about 1.45 nm.

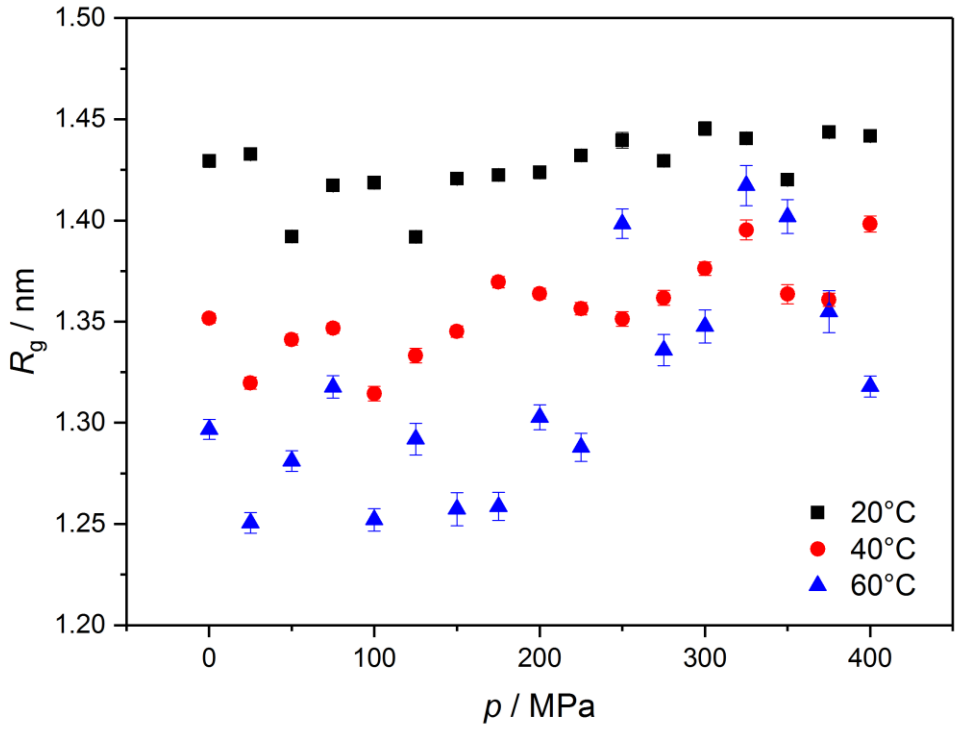

Figure 5-3. Influence of temperature and pressure on the radius of gyration derived by the Guinier approximation of the small RNA hairpin labeled with the two fluorophores.

To investigate these findings in more detail, temperature-dependent $P(r)$ functions were calculated, which are displayed in Figure 5-4 A. They show an increase in the occurrence of distances, r, of about 1.5 nm and a concomitant decrease of the occurrence of distances of about 3 nm within the molecule with increasing temperature. However, the maximal dimension, r_{max}, does not change markedly, indicating a rearrangement within the molecule. The pressure-dependent curves show an opposite trend, as can be seen in Figure 5-4 B. Pressure leads to an increase in the occurrence of distances with longer dimensions, while the maximal dimension also does not alter much with pressure.

In order to gain a better understanding of the observed changes in the $P(r)$ functions, we generated models of the labeled sRNAh for selected conditions. These conditions were ambient condition (20°C, 0.1 MPa), a high temperature at atmospheric pressure (60°C, 0.1 MPa) and ambient temperature at high pressure (20°C, 400 MPa). These models reveal a dumbbell-shape of the labeled sRNAh with one handle larger than the other for 20°C at 0.1 MPa (see Figure 5-4 C). The size of the larger handle of this dumbbell is in good agreement with the shape and size of the folded gcUUCGgc

sequence. For illustration, the PDB structure of this hairpin is superimposed on the model in Figure 5-4 C.

The smaller handle probably reflects the fluorophores linked to the latter. Upon temperature increase, the smaller handle becomes smaller while the larger handle becomes lager. This could be interpreted by one fluorophore swapping to the sequence region and forming a stacking interaction with the bases, explaining the change in the stability towards temperature upon labeling observed by other means.[236] With pressure, both handles become lager, suggesting partial unfolding of the labeled sRNAh with pressure.

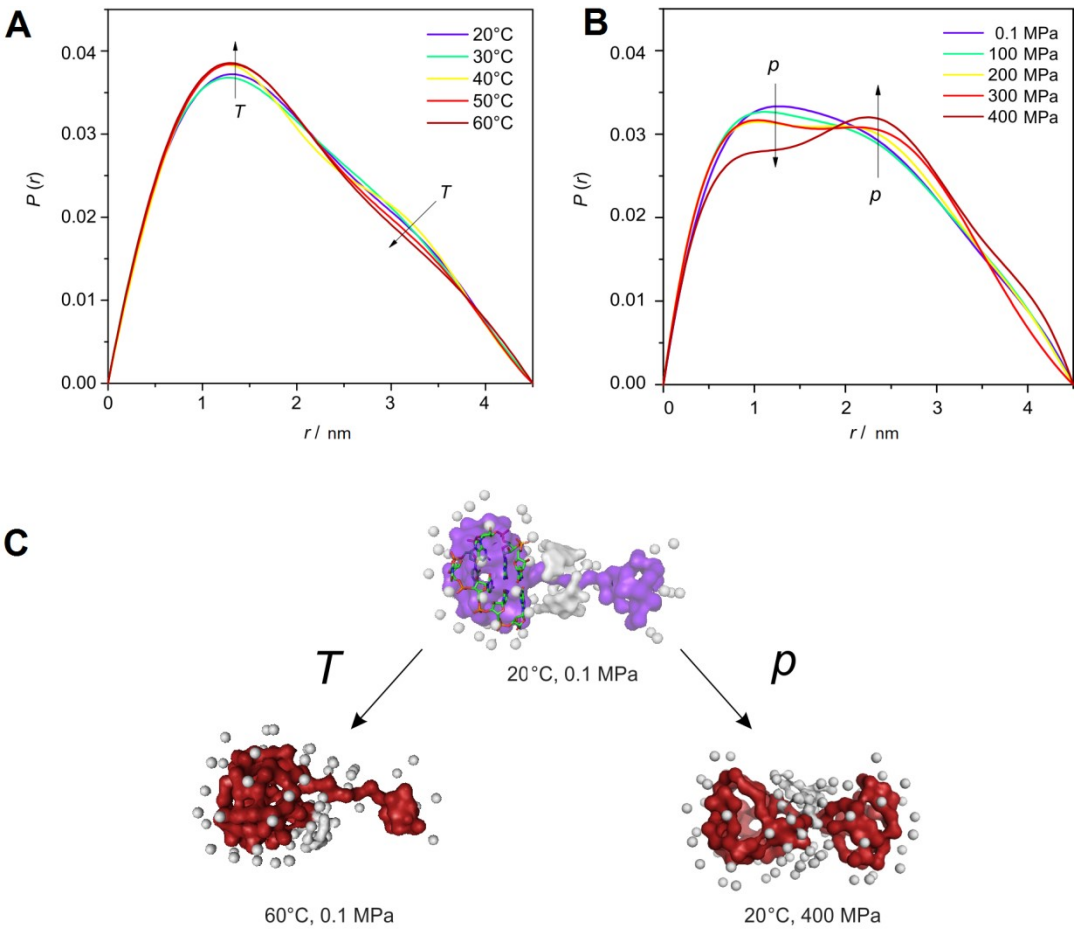

Figure 5-4. Influence of temperature and pressure on the overall shape of the labeled sRNAh. Pair distance distribution functions in dependence of temperature (A) and pressure (B) and models derived from the same data illustrating these changes (C). For comparison, the PDB structure (extracted from PDB-ID 1F7Y) of the sRNAh is laid over the larger handle of the model at ambient conditions. Temperature most likely promotes the interaction of a fluorophore with the bases of the sRNAh.

Conclusions

The conformational changes of the sRNAh of sequence gcUUCGgc were experimentally analyzed over a wide range of temperatures and pressures. SAXS measurements showed that increasing temperature leads to a rearrangement within the labeled RNA construct, which is in good agreement with one of the fluorophores interacting with the loop region. Also a significant effect of pressure on the radius of gyration was revealed, especially at high temperatures, also in corresponding FRET experiments.[236]

Being too small for analysis with small-angle X-ray scattering (<1 nm), the sRNAh without fluorophores was not investigated with this method. Instead FTIR and UV/Vis spectroscopy were used. The findings were substantially different from the labeled sRNAh. The unlabeled sRNAh shows a broad melting profile with continuous increase of unpaired conformations up to about 60°C. However, the sRNAh structure might not be fully unfolded at temperatures as high as 90°C and still comprise various partially unfolded compact conformations. Pressure up to 400 MPa were found to have a small effect on the base pairing and base stacking interactions of the sRNAh, indicating small conformational perturbations, only. The latter might originate from minor changes in packing and hydration of the RNA molecule upon compression. Pressurization at 70°C, i.e. above the melting transition, does not promote formation of new native stem connections after thermal denaturation.[236]

Finally, we noticed that Cy3/Cy5 labeling of the sRNAh changes, probably via stacking interactions between the fluorescent dyes and the nucleotide rings, the stability of the sRNAh, thereby rendering FRET analysis of the conformational dynamics of such small RNA structure inappropriate. The SAXS measurements presented in this chapter essentially contributed to the understanding how the attachment of fluorophores can influence the temperature- and pressure-dependent structure and stability of the small RNA constructs.

5.3 Ribozymes

5.3.1 Introduction

Ribozymes are RNA molecules with catalytic activity, which are regarded as precursors of modern enzymes. The conformational changes, which are also highly relevant for performing catalysis, are still not well understood. This is especially the case for the conformations they adopt under extreme conditions where ribozymes might have evolved. We conducted temperature, pressure and time dependent experiments on the hairpin ribozyme, including the influence of divalent ions (Mg^{2+}), which are required for its self-cleavage activity. The experiments were performed in order to evaluate the conformational stability of these RNA molecules under environmental conditions where ribozymes and protocells might have evolved, such as hydrothermal vent environments in the deep sea.

5.3.2 Materials and methods

The wild-type hairpin ribozyme wt-HpRz with the sequence 5'-AAACAGAGAA-GUCAACCAGAGAAACACACGUUGUGGUAUAUUACCUGGUACCCCCUGACAGU-CCUGUUU-3' was synthesized by IBA Life Solutions GmbH (Goettingen, Germany) and was received as lyophilized powder. This RNA sequence is a simple model system of the original four-way junction tobacco ringspot virus satellite RNA. The ribozyme was suspended in a 0.1 nmol μL^{-1} nuclease free water solution, and stored at - 80°C until usage. Solutions of 1 wt% wt-HpRz were prepared by resuspension in pure 50 mM TRIS-HCl buffer + 0.1 mM EDTA, pH 7.5. The cleavage reaction was initiated by adding the same volume of a double concentrated buffer solution of 50 mM TRIS- HCl + 0.1 mM EDTA + 2 mM or 4 mM $MgCl_2$. Final salt concentrations in the reaction were 1 mM or 2 mM MgCl2, respectively.

All measurements were performed at the ESRF beamline ID 02 (Grenoble, France) in a home-built high pressure cell with diamond windows.[32] The sample volume was 10 µL. The energy used was 16 keV and the sample to detector distance was 2.4 m. The samples were exposed to the beam for 0.25 s for each measurement. No radiation damages were detected within the total exposure time of a complete pressure series. The time-dependent measurements at atmospheric pressure were performed in a temperate quarz-capillary provided by the beamline.

All data was background corrected using scattering profiles of the pure buffer and analyzed using the SAXSutilities[215] software package provided by ESRF. Pair-distance distribution functions, $P(r)$, were calculated using the software GNOM of the Atsas software package [216].

5.3.3 Results and discussion

First, the pressure-dependent structural changes of the hairpin ribozyme (0.5 wt%) in buffer without magnesium were investigated (Figure 5-5). At these conditions, a very low rate of self-cleavage can be expected. The radius of gyration, R_g, decreases already at relatively low pressures such as 50 MPa and 100 MPa. In the regime between 150 and 250 MPa, the R_g remains constant and then decreases further at pressures above 250 MPa. The Kratky plots reflect this behavior. The maximum shifts towards higher q-values until 150 MPa, and remains almost constant until 250 MPa. Above this pressure, the logarithmic shape of the scattering curves reflects unfolding of the ribozyme. These findings are in agreement with our FRET and PAGE studies[237] revealing that low pressures favor the active docked-state of the ribozyme, which is more compact, and thus favor the self-cleavage reaction, though the overall ribozymatic reaction is retarded. Thus, pressures of up to 100 MPa, as can be found in the deep sea, would favor the docking of the ribozyme.

Next, the time-dependent measurements at 0.1 MPa employing different magnesium concentrations (Figure 5-6) were performed. Time-dependent studies show only very slight changes in the scattering profiles for all conditions displayed here. The minor changes observed might be explained by observing an ensemble of docked and undocked states being in equilibrium with each other and partial product dissociation only owing to the cleavage reaction.

The chosen magnesium concentrations (1 and 2 mM $MgCl_2$) were relatively low. Thus, only a low rate of self-cleavage can be expected, therefore the measurements were performed over a long time span for about 2 hours. Higher magnesium concentrations might speed up the cleavage reaction, but concomitantly favor the oligomer formation of the ribozyme. This is especially the case for the relatively high concentration of 0.5 wt% ribozyme needed for sufficient resolution in the high hydrostatic pressure cell used for the SAXS experiments. This effect makes an

unbiased interpretation of the data at higher magnesium concentrations difficult (Figure A3).

In the absence of stabilizing cations, higher concentrations of the ribozyme in order to increase the signal-to-noise ratio of the SAXS measurements lead to the occurrence of a correlation peak in the scattering profile (Figure A3), which can be explained by repulsion between the negatively charged RNA molecules in the absence of neutralizing cations.[238] The addition of magnesium at these even higher concentrations leads to an aggregation of the ribozyme. For the experiments presented here, the lowest concentrations of ribozyme leading to a sufficient resolution in the high pressure cell, but not to repulsion between the molecules, was chosen.

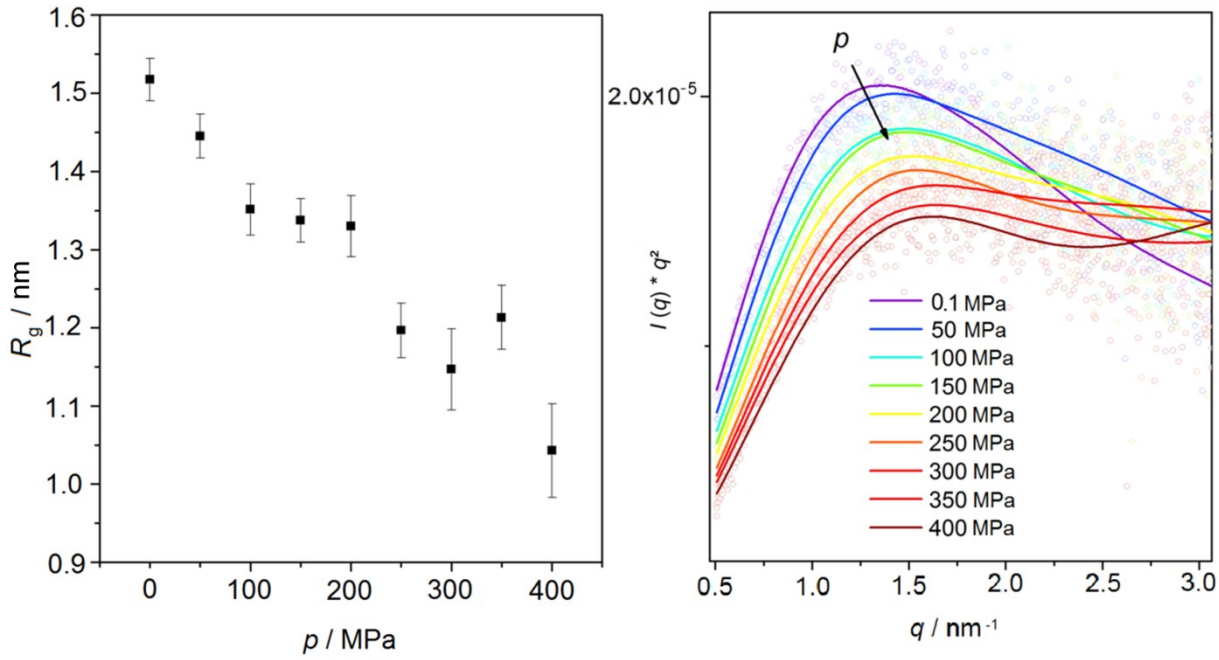

Figure 5-5. Pressure-dependent changes in the radius of gyration (left) and the Kratky plots (right) of the 0.5 wt% hairpin ribozyme in 50 mM Tris-HCl buffer without magnesium.

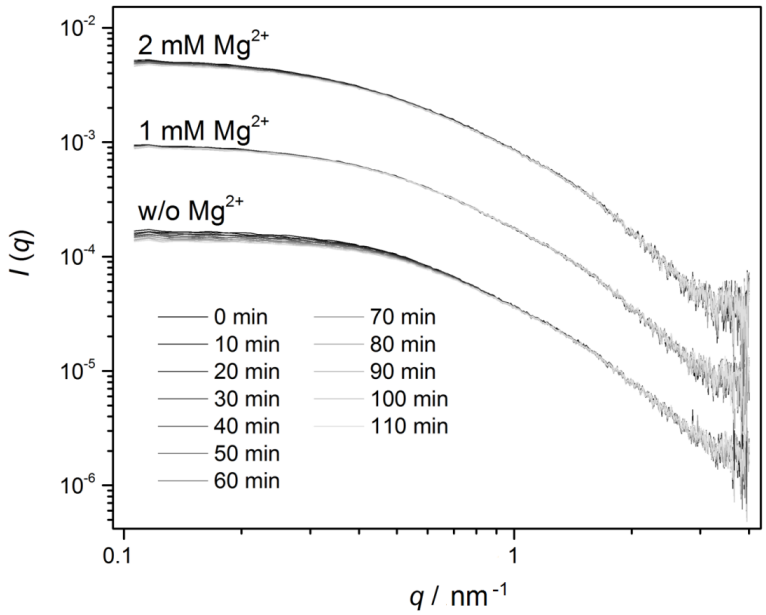

Figure 5-6. Time-dependent scattering profiles of 0.5 wt% hairpin ribozyme in 50 mM Tris-HCl with different magnesium concentrations.

Conclusions

The SAXS and FRET measurements on the hairpin ribozyme under high hydrostatic pressure conditions indicate increased population of the docked state at pressures up to 100 MPa, like found in the deep sea. However, at pressures above 250 MPa, the radius of gyration further decreases and the Kratky plots indicate unfolding.

In the time dependent measurements, no significant changes in the scattering profile pointing towards the known self-cleavage reaction of the hairpin ribozyme could be observed. Many factors could contribute to that. On the one hand, the nature of RNA as a polyelectrolyte strongly limits the concentration conditions and ionic strengths at which the form factor can be determined with sufficient accuracy. A too high concentration of the RNA in combination with low ionic strength leads to repulsion between the RNA molecules, while a too high ionic strength leads to oligomerization and aggregation. This might also be a reason why only very few SAXS studies on RNA are available so far.[239]

On the other hand, there is an equilibrium between many different states of the hairpin ribozyme and between cleavage and ligation. The different docked and undocked states were addressed by FRET studies, while the cleavage was investigated in PAGE analysis under denaturating conditions. The latter revealed an increase of the cleaved fractions from 30 % to 60 % in the presence of 6 mM Mg^{2+}.[237]

The reaction reached equilibrium after about 120 minutes. For the SAXS experiments, an even lower rate of self-cleavage can be expected, with a maximum of 2 mM Mg^{2+} present. In addition, the SAXS measurements were performed under non-denaturating conditions. Thus, it might be possible that the cleaved fragment remained on the ribozyme. Taken together, these factors might explain why the SAXS measurements were not able to resolve the self-cleaving reaction of the hairpin ribozyme.

5.4 Phenylalanyl transfer RNA

5.4.1 Introduction

In contemporary cells, aminoacylated transfer RNA (tRNA) connects the RNA and the protein world and plays a central role in protein biosynthesis.[93] The translation from RNA to an amino acid sequence is not only undertaken frequently in each living cell, but was also a key step in the development of proteins and the establishment of the genetic code. Even though many 3D crystal structures of tRNA molecules are available, their stability and conformational changes upon changes in temperature and pressure are still largely unknown, also under environmental conditions where the step from prebiotic catalytic RNA to proteins might have proceeded, such as hydrothermal vent environments encountered in the deep sea, where pressures up to 110 MPa are encountered. Fundamental research on the behavior of these molecules under extreme environmental conditions is required to help answer the question how the pathway from an ancient RNA world towards a modern protein world was initiated.

Next to the small-angle X-ray scattering study presented in this subchapter, which allows elucidation of changes in shape and size, complementary Fourier-transform infrared and fluorescence spectroscopic studies were carried out in our lab to reveal complementary changes in tertiary and secondary structure of the chosen model tRNA molecule, $tRNA^{Phe}$. The aim of this project was to evaluate the possibility of deep-sea-like conditions for the step from an RNA world towards a protein world via tRNA by measuring the conformational stability of $tRNA^{Phe}$ under extreme conditions of temperature and pressure including stabilizing and destabilizing additives, such as Mg^{2+}. The temperature-dependent SAXS results presented in the following

subchapters were published in the journal *ChemPhysChem*[176] and are partially reproduced here with permission, copyright © John Wiley & Sons, 2015.

5.4.2 Materials and methods

Yeast phenylalanine transfer RNA ($tRNA^{Phe}$) was obtained from Sigma Aldrich (St. Louis, MO) and used without further purification. Nuclease-free water, pipette tips, microfuge tubes, conical tubes and RNase AWAY® reagent were obtained from Ambion® (Life Technologies). All experiments were carried out in D_2O or 50 mM Tris-HCl buffer + 0.1 mM EDTA, pH 7.5, in the presence or absence of 15 mM $MgCl_2$. All samples were lyophilized from solutions in D_2O and resuspended to the different conditions needed. All items related to sample handling were nuclease-free proofed or cleaned with RNase AWAY® reagent (Invitrogen®).[240]

Temperature-dependent SAXS data were obtained with a SAXSess mc^2 small-angle X-ray scattering instrument from Anton Paar GmbH (Graz, Austria), equipped with a sealed tube X-ray generator Iso-Debyeflex 3003 from GE Inspection Technologies (Ahrensburg, Germany). Cu-Kα radiation was used (λ = 0.154 nm) and the instrument was operated with 40 kV and 50 mA. Solutions of 0.5 wt% (or 3 wt%) $tRNA^{Phe}$ in the absence and presence of 15 mM $MgCl_2$ were prepared in D_2O as well as in 50 mM Tris-HCl buffer, 0.1 mM EDTA, pH 7.5. The exposure time of the sample to the X-rays was 30 min per measurement. The data were collected for q-values between 0.12 and 4.00 nm^{-1}. The measurements covered a temperature range from 5 to 90°C in steps of 5°C.

The sample was measured in the slit configuration using a 1 mm quartz capillary (μ-cell) suitable for the TCS 120 temperature-controlled sample holder unit from Anton Paar (Graz, Austria). While recording the temperature-dependent scattering data, temperature was adjusted by the TCS control unit for TCS sample stages from Anton Paar (Graz, Austria). Detection was performed via 2D-imaging plates, which were read out using the Storage Phosphor System Cyclone Plus by Perkin Elmer (Waltham, Massachusetts). The latter was operated by the software Optiquant. The 2D images obtained were transformed to an intensity profile, $I(q)$, using the software 2D-SAXSquant. The raw data obtained were normalized to the primary beam intensity and corrected for the background using the pure solvent in SAXSquant 3.1 software provided with the SAXSess mc^2 system. Further, the data were desmeared to compensate for instrumental broadening effects ("slit-smearing") using the GNOM

software.[216] The latter was also used to calculate the pair-distance distribution functions, $P(r)$, using the indirect Fourier transformation method.

Pressure-dependent measurements were performed at the ESRF beamline ID 02 (Grenoble, France) in a home-built high pressure cell with diamond windows.[32] The sample volume was 10 µL. The energy used was 16 keV and the sample to detector distance was 2.4 m. The samples were exposed to the beam for 0.25 s for each measurement. No radiation damages were detected within the total exposure time of a complete pressure series.

5.4.3 Results and discussion

Temperature-dependent measurements on tRNA^{Phe}

To reveal corresponding changes in the overall shape of the tRNA^{Phe} upon temperature change, small-angle X-ray scattering measurements were carried out. As an example, Figure 5-7 shows the temperature dependent intensity profiles of 0.5 wt% tRNA^{Phe} in pure solvent (D_2O) in the absence and 3 wt% tRNA^{Phe} in the presence of 15 mM Mg^{2+}. Like discussed in the previous subchapter, in the absence of stabilizing ions the sample had to be diluted to 0.5 wt% in order to eliminate the correlation peak arising from repulsion between the negatively charged molecules and to exclusively access the form factor.

In order to gain information about changes in compactness and unfolding of the molecule, the data are plotted also in the Kratky representation (insets of Figure 5-7 A and B). In both cases, with and without Mg^{2+}, a highly compact form of tRNA^{Phe} is observed at low temperatures, as can be seen from the Gaussian shape of the Kratky plots. With increasing temperature, we observed a gradual loss of compactness in the range between 45 and 65°C for tRNA^{Phe} in the absence of Mg^{2+}. In the presence of Mg^{2+}, the loss of compactness takes place at significantly higher temperatures and within a much smaller temperature range (75-85°C), in good agreement with the thermodynamic data for tRNA^{Phe} unfolding.[241]

Clearly, no complete unfolding is seen here as observed in the presence of urea.[242] Measurements were also carried out in the Tris-HCl buffer, which does not lead to significant changes in the temperature dependent SAXS profiles compared to the

data in pure solvent, however (Figure A8). The transition range in Tris-HCl buffer takes place between 50 and 60°C without Mg^{2+}, and between 80 and 90°C with Mg^{2+}.

Further analysis of the scattering data (Guinier analysis, evaluation of the pair-distance distribution function $P(r)$, Figure A9) indicate that the radius of gyration, which is about 2.2 nm in the native state, does not change markedly for all solution conditions upon rising the temperature, i.e. the structural changes taking place seem to involve more internal structural rearrangements of the L-shaped RNA molecule rather than a complete unfolding to a random-coil kind of conformation as often observed for temperature-induced unfolding of proteins.[243]

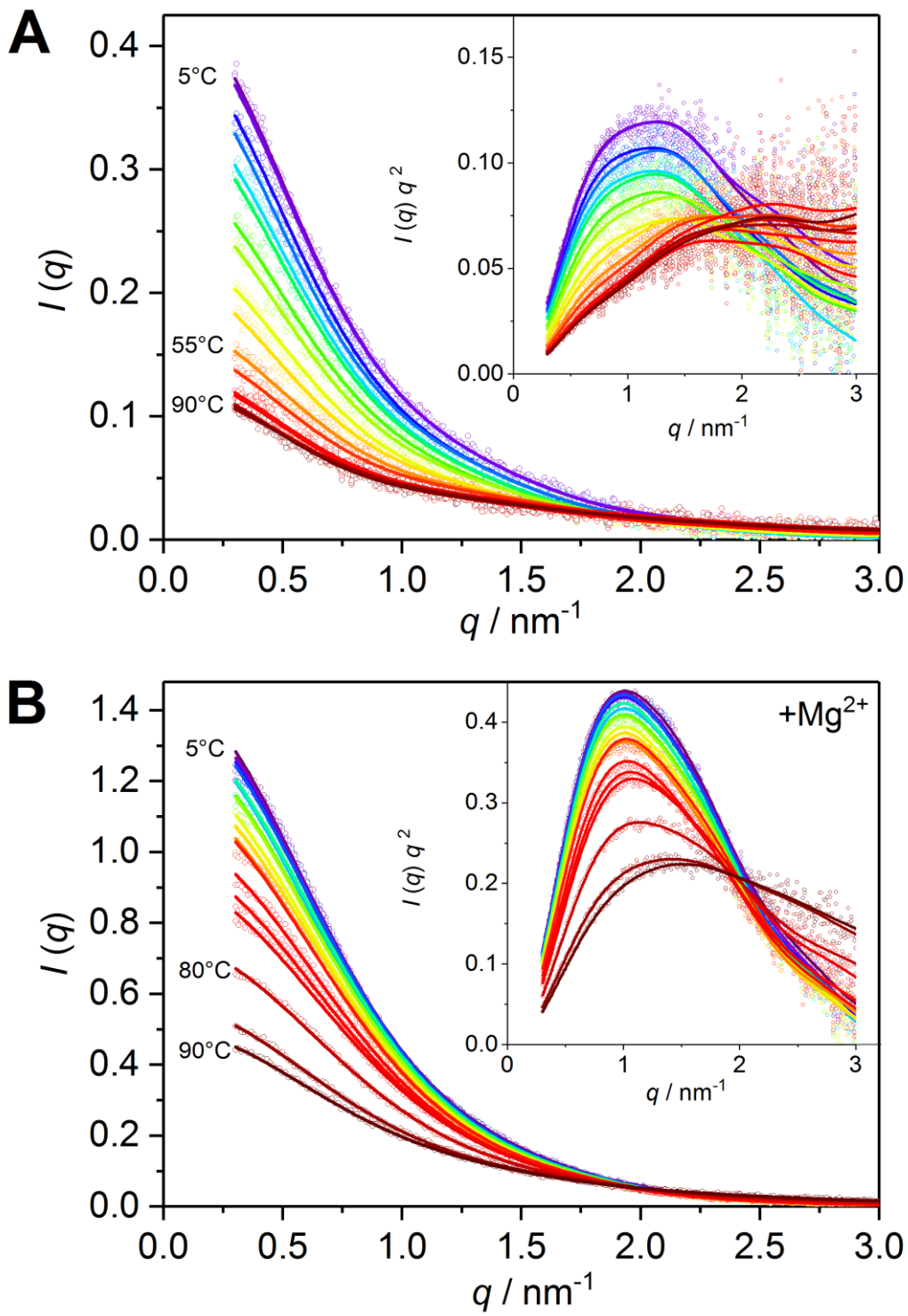

Figure 5-7. Temperature dependent SAXS data and analysis of $tRNA^{Phe}$ in D_2O in the absence (a) and presence of 15 mM Mg^{2+} (b). Intensity profiles were recorded in a temperature range starting from 5°C (purple) in steps of 5°C up to 90°C (dark red). Solid lines represent fits obtained using the indirect Fourier-transformation method. Concentrations were 0.5 wt% in pure D_2O and 3 wt% with 15 mM Mg^{2+}. Inserts: Kratky plots of the respective data.

Pressure-dependent measurements on tRNA^{Phe}

Further small-angle X-ray scattering SAXS measurements aimed at elucidating changes in shape and size of tRNA^{Phe} under extreme conditions of pressure, including the influence of Mg^{2+}. Fourier-transform infrared and fluorescence spectroscopic studies were carried out in our lab to reveal complementary changes in tertiary and secondary structure.[176] The overall goal of the project was to evaluate the conformational stability of RNA at harsh deep-sea-like conditions, where prebiotic catalytic RNA reactions might have evolved.

Our pressure-dependent measurements revealed a surprisingly high stability of the tRNA^{Phe} at pressures up to 400 MPa. Pressure-dependent SAXS data of tRNA^{Phe} at 20°C in the absence (Figure 5-8 A and B) and presence (Figure 5-8 C and D) of Mg^{2+} ions are displayed. Even in the absence of stabilizing Mg^{2+} ions, no complete unfolding of the tRNA^{Phe}, as monitored in the presence of urea and at elevated temperatures, is observed. According to the calculated $P(r)$ functions, the changes of the shape and size upon compression are very small. This is in good agreement with our FTIR and fluorescence data, which reveal a maximum of only 15 % of unpaired bases up to a pressure of 1000 MPa, indicating only small changes in the secondary and tertiary structure.[176] The biological implications of the high stability of tRNA under high hydrostatic pressure conditions could be that it is possible that the step from an RNA world via tRNA to a protein world proceeded in the deep sea, where pressures up to the 100 MPa level are encountered.

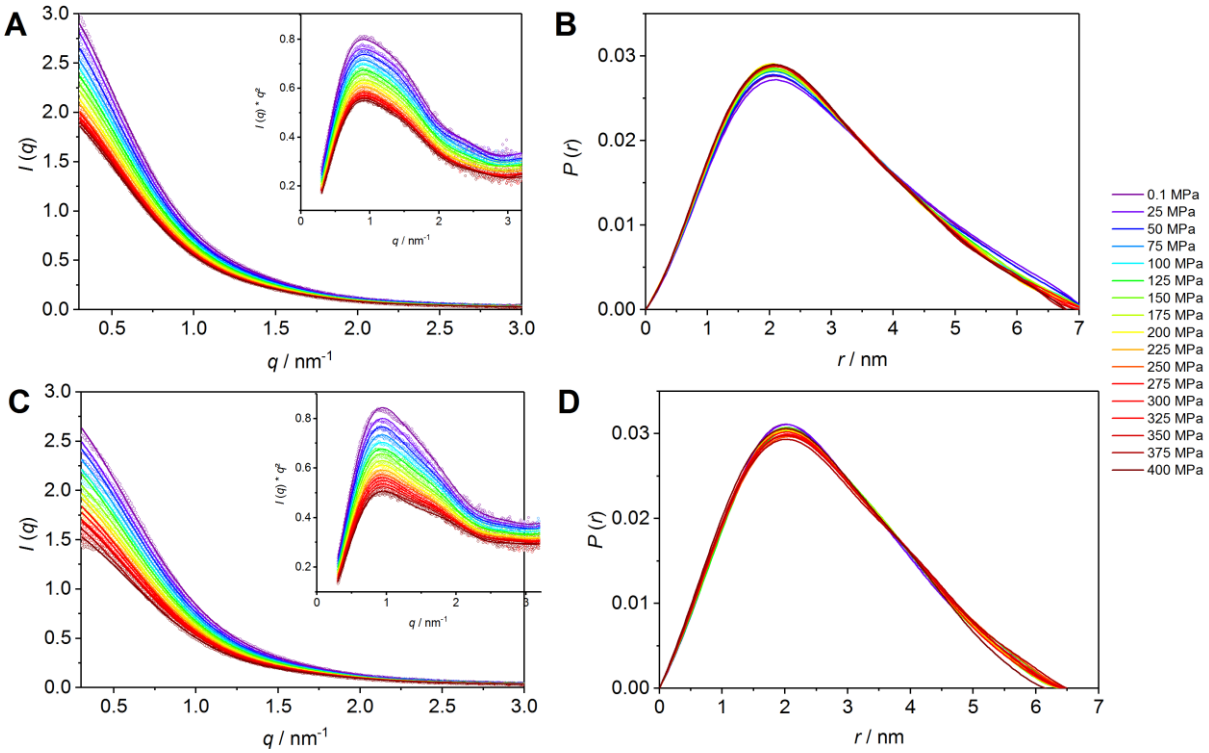

Figure 5-8. Pressure-dependent SAXS data of $tRNA^{Phe}$ at 20°C (3 wt% in 50 mM Tris-HCl buffer, pH 7.5, with 0.1 mM EDTA in the absence of $MgCl_2$ (A, B) and presence of 15 mM $MgCl_2$ (C, D.) Intensity profiles at different pressures (A,C) with Kratky representation of the respective data (inserts). Solid lines represent fits obtained by using the indirect Fourier-transformation method to calculate the pair-distance distribution functions (B,C).

Conclusions

In combination with FTIR and fluorescence measurements,[176] the SAXS results show that the native structure of $tRNA^{Phe}$ is disrupted upon removal of Mg^{2+}, which leads to a markedly different temperature and pressure stability of the RNA. Addition of Mg^{2+} stabilizes the compact structure of the RNA against temperature, which thus increases the melting temperature of the RNA by about 30°C. Concomitantly, cooperativity of the melting transition increases. Mg^{2+} ions stabilize the tertiary structure in such a way that the entire structure melts essentially by a two-state transition, in accordance with literature data.[244]

The increase in the temperature stability can be attributed to an effective screening of the negative charges along the phosphate–sugar backbone of the tRNA. According to the SAXS data, the structural changes that take place upon melting seem to

involve essentially internal structural rearrangements of the tRNA molecule, rather than a complete disruption of the tertiary structure.

The pressure-dependent data indicates that the tertiary structure of $tRNA^{Phe}$ is highly stable up to 400 MPa in both cases, with and without Mg^{2+}. Our observations are in good agreement with the FTIR measurements revealing only small changes in the secondary structure upon pressurization. However, minor changes in the tertiary structure, which could not be resolved so far by our measurements, cannot be excluded. The high stability of $tRNA^{Phe}$ upon pressure may be expected, since HHP is known to stabilize helical forms and support supercoiling of nucleic acids.[245]

6 Investigations of peptides and proteins

This chapter is divided in three subchapters with rising complexity of the protein system under investigation. Starting from the elastin-like peptide (ELP), a small peptide consisting of 18 amino acids only and close to the size limit of SAXS, the much larger phosphoprotein 32 will be explored. Finally, the effect of temperature and pressure on actin bundles, a very important network of proteins providing cellular integrity, is explored taking advantage of the diffraction of the hexagonal arrangement of the filaments within the bundles.

6.1 Elastin-like peptide

6.1.1 Introduction

In this study, the inverse temperature transition of the elastin-like peptide establishing the sequence GVG(VPGVG)$_3$ was analyzed in the absence and presence of different cosolutes. Among those there were cosmotropic cosolutes such as TMAO and chaotropic cosolutes such as urea and a mixture of TMAO and urea. Besides these two naturally occurring cosolutes, the effect of 2,2,2-trifluoroethanol (TFE) was examined. TFE is a nonpolar solvent, which can have two opposed effects. On the one hand it can initiate structure, since it favors hydrophobic interactions.[246] On the other hand, it can also act disruptive on hydrophobic interactions within the core of globular proteins. TFE can form clusters in size of 0.5 to 1 nm at concentrations between 10 to 80% (v/v).[192] In this study, 2 M TFE were used, which corresponds to a concentration of 12% (v/v). This concentration is on the lower end of the range where cluster formation was observed. Thus, some TFE-clusters might form, but are not expected to be very pronounced and stable under these conditions. TFE-clusters could interact with the hydration shell of the peptide by stripping water molecules from the peptide surface and thus promote the intermolecular interaction of valine side chains. Furthermore, the distance between two valine side chains in type II β-turns of the ELPs ranges from about 0.4 nm in the contracted and up to about 0.6 nm in the expanded state.[247] Consequently, one TFE-cluster of the appropriate size could fit between two valine side chains. In this case, TFE would clearly favor hydrophobic interactions.

The following SAXS measurements were performed to complement FTIR (Dr. Marie Kahse) and NMR studies (Dr. Kerstin Kämpf, Susann Weißheit) within the DFG

Forschergruppe FOR 1583. Measurements were carried out in deuterated solvents and a relatively high concentration of 10 wt% of the peptide in order to ensure comparability.

Preliminary small-angle neutron scattering measurements presented on the meeting of the DFG-Forschergruppe 1583 on the 14th of March 2017 by Alexander Matt[248] showed an increase in the radius of gyration in dependence of the peptide concentration up to 2.3 wt%, upon which R_g approaches a plateau value of about 1 nm, which is the lower limit of the size range accessible by SAXS and SANS. At 35°C, the determined values for R_g range from 0.6 nm at a concentration of 0.3 wt% and 1 nm at 2.3 and 6.7 wt%, respectively. Regarding the small size of the peptide containing only 18 amino acids, a concentration above 2.3 wt%, e.g. 10 wt% like used in the experiments presented here, might in fact be necessary to obtain scattering data in sufficient quality.

6.1.2 Materials and methods

The purified elastin-like peptide was kindly provided by the group of Prof. Dr. Christina Thiele, TU Darmstadt, and was used as received. SAXS measurements were performed at a concentration of 10 mg/mL in 50 mM phosphate buffer in D_2O, pD 7.0, to ensure comparability with FTIR and NMR measurements. Deuteriumoxide and TFE were purchased from Fluka, sodium phosphate monobasic dehydrate ($NaH_2PO_4 \cdot 2\ H_2O$), disodium hydrogen phosphate dihydrate ($Na_2HPO_4 \cdot 2\ H_2O$) and ^{13}C-urea from Sigma-Aldrich, and trimethylamine-*N*-oxide (TMAO) from Merck. The conditions chosen for the SAXS measurements are reported in Table 6-1.

Table 6-1. Compositions and conditions for the SAXS measurements on the ELP.

c (ELP) / wt%	***c* (TMAO) / M**	***c* (urea) / M**	***c* (TFE) / M**	***T* /°C**
10	-	-	-	10, 20, 30, 40, 50, 60, 70, 80
10	1	-	-	10, 80
10	-	2	-	10, 20, 30, 40, 50, 60, 70, 80
10	1	2	-	10, 80
10	-	-	1	10, 20, 30, 40, 50, 60, 70, 80

Temperature dependent measurements were performed on a SAXSess mc² instrument (Anton Paar, Graz, Austria) using a monochromatic X-ray beam (λ = 0.154 nm) with line focus and an imaging plate detector (Cyclone, Perkin Elmer, USA). The 2D scattering pattern was integrated into the one-dimensional scattered intensities $I(q)$ as a function of scattering vector, , using the software SAXSquant 3.1 (Anton Paar, provided with the instrument), where 2θ is the total scattering angle. The same software was used for background correction of the data with the scattering profiles of the pure solvent. Scattering patterns were collected with an exposure time of 30 min per image. Desmearing of the data and calculation of the pair-distance distribution functions, $P(r)$, were performed using the software GNOM[249]. For the shape reconstructions, the software DAMMIN Version 5.3[25] was used (keep-mode).

6.1.3 Results and discussion

We performed temperature-dependent SAXS measurements on the ELP in the presence of different cosolutes in order to investigate its size and shape changes in order to complement our FTIR data. The changes in R_g with temperature are displayed in Figure 6-1. R_g slightly increases from about 1 nm at 10°C to about 1.2 nm at 80°C in pure buffer, 1 M TMAO, 2 M urea as well as for the mixture containing 1M TMAO and 2 M urea. The only exception to this behavior is found in the presence of TFE, in which the value found for R_g was about 1.2 nm at 10°C and increases to about 1.45 nm at 80°C. For pure buffer and all other cosolutes, the radius of gyration of about 1 nm at 10°C is in good agreement with MD simulations[191] and the preliminary SANS measurements performed in pure buffer. However, the increase of this value is contradictory to the theoretical investigations predicting a decrease of the R_g at elevated temperatures. In agreement to the data presented here, the preliminary SANS measurements by Alexander Matt[248] also showed a slight increase of R_g with rising temperature.

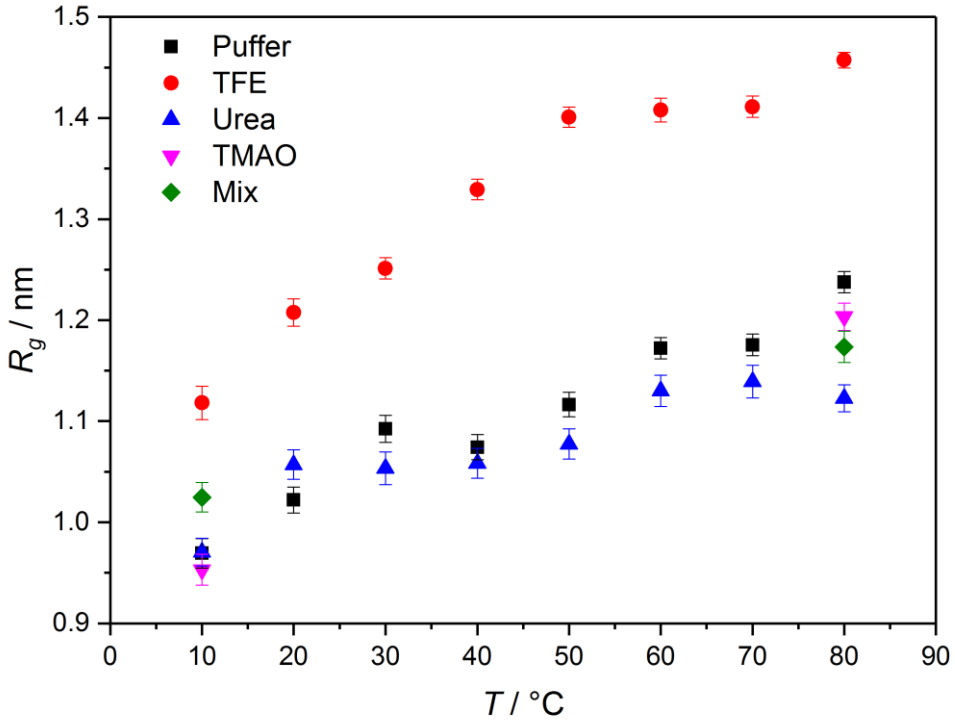

Figure 6-1. Temperature dependent changes in the radius of gyration of the ELP in the absence and presence of different cosolutes.

The scattering intensity profiles and pair distance distribution function, $P(r)$, in pure buffer (Figure 6-2 A), indicate that the changes with increasing temperature are very small. These observations are in good agreement to the slight changes observed by FTIR.[250] The Kratky-plots (Figure 6-2 A, inset) show a bell shape, indicating a compact and folded state at both temperatures, 10°C and 80°C, respectively.

The same was also observed in the presence of 1 M TMAO and a mixture of 1 M TMAO and 2 M urea (Figure A10, A-D). In presence of 2 M urea, the Kratky-Plot reveals slightly more disorder and lower compactness, since, contrary to the Kratky-plots in buffer and in the presence of TMAO, $I\ (q)\ q^2$ approaches a plateau value, as can be expected in the presence of a destabilizing agent like urea (Figure A10, E and F).

$P(r)$ -functions and shape reconstructions in pure buffer indicate a slightly ellipsoidal shape at 10°C (Figure 6-2 C). An increase in temperature leads to a slight elongation explaining the increase in R_g. Though contrary to MD simulations[191], the formation of a β-helix from a random-coil might in fact be consistent with an elongation of the

peptide's shape. Further, they reveal the formation of a slight bend at elevated temperatures in buffer (Figure 6-2 C).

In case of the 2 M TFE, temperature-dependent changes are much more pronounced, as can already be seen from the drastic increase in intensity at low angles after heating to 80°C (Figure 6-2 A). $P(r)$-functions as well as shape reconstruction reveal a significant elongation to a maximum length of about 6.5 nm at 80°C (Figure 6-2 D). However, the bell shape of the corresponding Kratky-plot (Figure 6-2 D) still persists at this temperature suggesting a rather compact state. Thus, the effect of TFE differs significantly from the effect of the other cosolutes, in accordance with the observations in the FTIR study.[250]

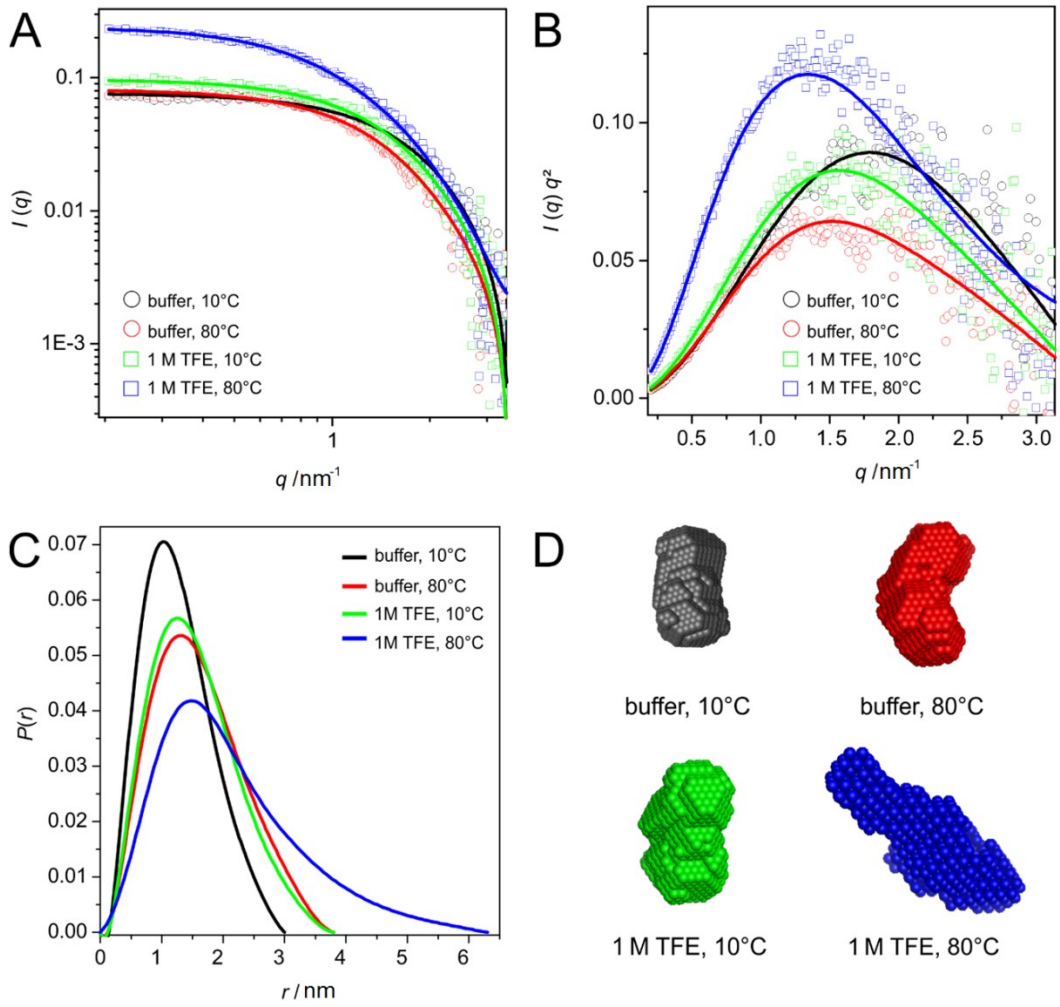

Figure 6-2. Temperature-dependent changes in the structure of the elastin-like peptide in the presence and absence of TFE. (A) Small-angle X-ray scattering profiles in double logarithmic and in Kratky-plot representation (B) in the absence (circles) and presence of TFE (squares) at 10°C and 80°C, (C) pair distance distribution functions, $P(r)$, and (D) corresponding shape reconstructions in the absence and presence of TFE.

Conclusions

The results suggest a direct interaction of the TFE with the peptide explaining the increase in size observed already at cold temperatures. According to our results, the cosolutes TMAO and urea and the mixture of both do not affect the shape and size changes of the ELP with increasing temperature markedly.

With rising temperature, an increase in the radius of gyration is observed under all conditions studied. Though contrary to the predictions of theoretical studies[191], this might be in accordance with the formation of β-helical structures from a random-coil. Indeed, FTIR results performed under identical conditions show that with increasing temperature there is an increase in the absorbance characteristic of type II β-turns and other loop structures, whereas a concomitant decrease of the disordered structures can be observed. This trend is characteristic for the inverse temperature transition of ELPs and continues in the entire measured temperature range up to the highest temperature of about 88°C without reversal.[250]

6.2 Phosphoprotein 32

6.2.1 Introduction

In the study presented here, we focussed on the folding landscape of the tumor suppressor phosphoprotein 32 (PP32). It belongs to a family of proteins establishing leucine-rich repeats (LRR), a structural motif occurring in many functionally different proteins, whose detailed folding/unfolding mechanism needs still to be explored. Because pressure acts locally on protein folded states to eliminate void volume, it provides a unique and powerful means for revealing folding intermediates and dissecting cooperative interaction networks within protein structures. The results of the pressure dependent SAXS studies performed here should complement site specific NMR data in order to explore and map the folding landscape of PP32 in great detail. Investigations performed here involve the wildtype (WT) PP32 as well as two mutants. These mutants were PP32-Δ-NCap, on which the N-Terminal capping motive has been deleted, and PP32-Y131F/D146L, being unable to form the stabilizing structural hydrogen bond. Depending on the stability of the variants, a sufficient amount of urea was added to each sample to make the proteins unfold in the pressure range accessible by high pressure NMR, i.e. below 300 MPa. A manuscript reporting the results is in preparation.[251]

6.2.2 Materials and methods

Sample preparation

The WT-PP32 protein and its mutants PP32-Y131F/D146L and PP32-Δ-Ncap were provided by the group of Prof. Catherine Royer (Troy, NY, USA). The proteins were synthesized as reported by *Dao et al.*[201] Besides the protein sequence, they contained an additional His-tag (-RDDKEWLEHHHHHHH) for purification. They were received as solutions with concentrations between 2.5 and 7.5 mg mL^{-1} in 20 mM Bis-Tris buffer, pH 6.8, with 5 mM DTT (Sigma Aldrich, Munich, Germany). Amicon® Ultra 15 mL Centrifugal Filters (Merck, Darmstadt, Germany) were used to increase the protein concentration to 20 mg mL^{-1}. The required amounts of an 8 M urea (Sigma Aldrich) stock solution in Bis-Tris buffer and the according Bis-Tris buffer were added to the concentrated protein solutions in order to reach the desired concentrations given in Table 6-2. Before filling the samples into the sample container for the SAXS measurements, they were centrifuged for 1 min at 5000 rpm to remove any aggregates which might have formed during the concentrating process or due to the addition of urea.

Table 6-2. Concentrations and conditions of the PP32 samples investigated.

	***c* (PP32) / wt%**	***c* (Urea) / M**	***T* /°C**
WT-PP32	1	1.5	20, 30 40
PP32-YFDL	1	0.5	20
PP32-Δ-NCap	1	0	20

Pressure-dependent SAXS measurements at different temperatures

Pressure dependent SAXS measurements on the wild-type protein, PP32WT, were performed at the Storage Ring SOLEIL, beamline SWING (Saint-Aubin, France). The intensity is recorded as a function of the wave vector transfer, q. The photon energy used was 15 keV (λ = 0.0827 nm). The sample-to-detector distance was 2 m, covering a q-range between 0.2 and 3 nm^{-1}. The samples were exposed to the beam for 1 s per measurement. Pressure was increased in steps of 40 MPa. Integration of the images and normalization to the primary beam intensity were performed with the software Foxtrot 3.3.0 provided by the SWING beamline.

The measurements on the two PP32 mutants PP32-Y131F/D146L and PP32-Δ-NCap were performed at the European Synchrotron Radiation Facility, beamline ID02 (Grenoble, France). The energy used was 16 keV (λ = 0.0775 nm) and the sample to detector distance was 2.4 m covering a q-range between 0.2 and 3 nm^{-1}. The samples were exposed to the beam for 0.25 s for each measurement. Pressure was increased in steps of 20 MPa.

All measurements were performed in a home-built high pressure cell with two flat diamond windows.[32] Pressure was applied with a manual hydraulic spindle pump (SITEC-Sieber Engineering AG, Maur (Zurich), Switzerland) using water as pressurizing medium. The temperature was maintained using a water bath with an accuracy of ± 0.1°C. The sample volume was 10 µL. No radiation damages were detected within the total exposure time of a complete pressure series. The scattering profiles were background corrected using measurements of the corresponding buffer with the software package SAXSutilities[215] provided by the ESRF. Pair-distance distribution functions, $P(r)$, were calculated using the software GNOM of the ATSAS software package.[249] *Ab initio* models of the folded and pressure-denatured states were reconstructed using the GASBOR web interface[237] by fitting the reciprocal data.

6.2.3 Results and discussion

Pressure-dependent measurements of WT-PP32 at different temperatures

The aim of this section is to investigate the pressure-dependent unfolding behaviour of the WT-PP32 at different temperatures by small-angle X-ray scattering. Analysis of the recorded intensity profiles and radius of gyration, R_g, (Figure A11, Figure 6-3), respectively, enabled quantitative evaluation of the changes in the size of WT-PP32 with increasing pressure. The R_g-value at 0.1 MPa, which was determined from the Guinier region, was found to be 1.84 nm at 15°C, 1.69 nm at 20°C and 1.57 nm at 30°C. Thus, the overall size shows a slight decrease with increasing temperature. For all temperatures, the folded state at these conditions is of elliptical shape with a maximum length of about 5 nm, as can be derived from the corresponding $P(r)$-functions (Figure 6-4 A-C).

The overall change in the radius of gyration (Figure 6-3) with pressure is similar for all three temperatures investigated. By applying pressure, we found a duplication in the

radius of gyration, reaching values of about 3.5 nm at 250 MPa at all temperatures. For higher pressures, the calculation of the R_g was omitted, since the pressure-unfolded state was already reached at 250 MPa. The R_g determined at a pressure of 210 MPa of the 20°C-series (open red circle) was considered to be an outlier and has not been included when fitting the sigmoidal curve to the data points.

The midpoint of the unfolding curves is ~125 MPa for 15°C, 140 MPa for 20°C and 160 MPa for 30°C, respectively. This indicates a slight pressure stabilization with increasing temperature. This may be expected, since it is a typical feature of the elliptical p,T-stability diagram of proteins.[180] While SAXS reveals a sigmoidal unfolding curve pointing towards a two-state unfolding behavior, complementary NMR data reveal intermediate structures (conformational substates) at 30°C[251], not being distinguishable by SAXS. Thus, the formation of these intermediate structures probably does not involve significant changes in size and shape.

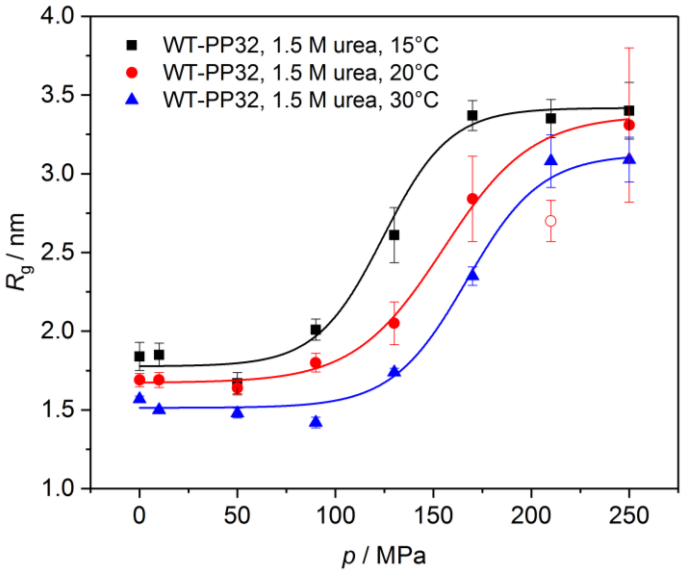

Figure 6-3. Pressure- and temperature-dependent changes in the radius of gyration, R_g, of 1 wt% WT-PP32 in 20 mM Bis-Tris, pH 6.8, +1.5 M urea and 5 mM DTT.

The pressure-unfolded state looks very similar to the urea-unfolded state which was analysed previously using a laboratory instrument.[251] Both, the pressure and the urea unfolded state, represent an elongated shape with a maximum length of about 15 nm as shown by the calculated $P(r)$ functions (Figure 6-4, A-C). In this state, the protein seems to be completely unfolded, which is also confirmed by analysing corresponding Kratky-plots (Figure 6-4, D-F). Additional *ab initio* reconstruction of the

pressure-unfolded WT-PP32 also suggested a fully extended structure at 400 MPa and 20°C (Figure A13).

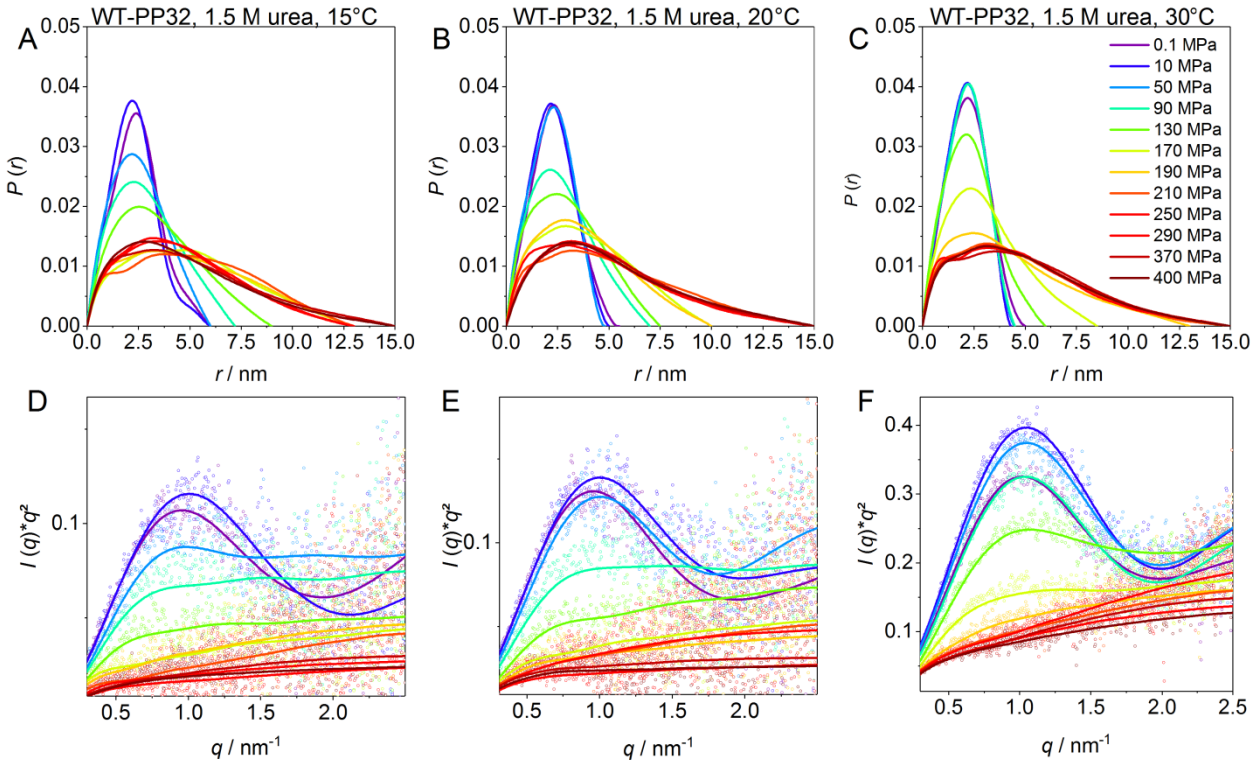

Figure 6-4. High pressure SAXS profiles of the LRR protein WT-PP32. The three panels on the top are the Pair-distance-distribution functions $P(r)$ of WT-PP32 at 15°C (A), 20°C (B), and 30°C (C). Panels D, E, and F represent the Kratky plots of WT-PP32 at 15°C, 20°C and 30°C, respectively.

WT-PT32, PP32-ΔN-Cap and PP32 Y131F/D146L at 20°C

While in the previous section the focus was to compare the pressure-induced unfolding of the WT-PP32 at different temperatures, in this section the pressure unfolding of the WT-PP32 will be compared with that of the two mutants, PP32-ΔN-Cap and PP32 Y131F/D146L. All measurements were performed at 20°C with varying amounts of urea. As described in the previous sections, the pressure dependence of the WT-PP32 at 20°C and a concentration of 1.5 M urea showed a sigmoidal unfolding profile, and a R_g-value at high pressure as well as $P(r)$ and Kratky plots that were consistent with complete unfolding (Figure 6-3, Figure 6-4 A,D).

The SAXS profiles and R_g-values for the double mutant, PP32-Y131F/D146L, at atmospheric pressure were nearly identical to those of WT-PP32 (Figure A12, Figure 6-5 A, C and E). Likewise, the intensity profiles of the pressure-unfolded state of PP32-Y131F/D146L at 250 MPa are similar to those obtained for WT-PP32 (Figure 6-4).

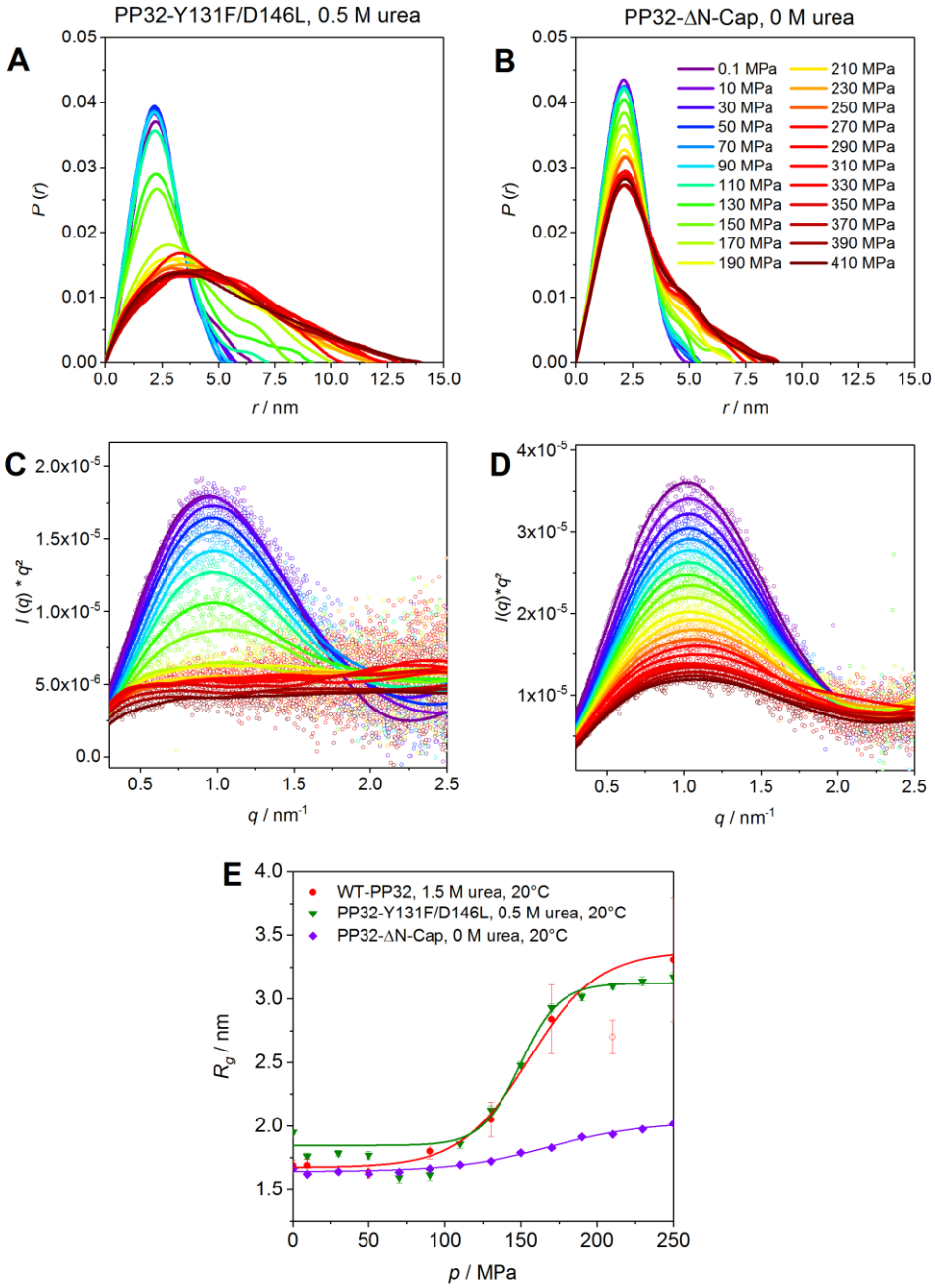

Figure 6-5. High pressure SAXS profiles of the PP32 mutants at 20°C. $P(r)$ of PP32-ΔN-cap (A), and PP32-Y131F/D146L (B). (C) and (D) represent the Kratky plots of PP32-ΔN-cap and PP32-Y131F/D146L, respectively. (E) Changes in the radius of gyration of the two PP32 mutants and, for comparison, of the WT-PP32 at 20°C (same data as in Figure 6-3).

In contrast, the unfolding curve of the PP32-ΔN-cap variant shows a completely different behavior (Figure A12, Figure 6-5 E). The R_g-value of this variant reaches a plateau of 2.48 nm at pressures above 250 MPa. The midpoint of the unfolding curve is at about 175 MPa, at a slightly higher pressure than found for the other variants. This value is much lower than that expected for a random coil. *Ab initio* reconstructions (Figure A13) indicate that the PP32-ΔN-cap remained partially folded even at the highest pressures investigated. Assuming a partially pressure unfolded state of PP32-ΔN-cap with an $R_g(U_{HP})$ of 2.48 nm, and following an apparent two-state equation,

$$R_g^2(p) = F(p) \times R_g^2(F) + U(p) \times R_g^2(U_{HP}) \quad (6.1)$$

$$F(p) + U(p) = 1 \quad (6.2)$$

an unfolded fraction, $U(p)$, of 73% was determined at 250 MPa. This is consistent with the stable C-terminal subdomain remaining partially folded (25% remaining signal for residues in repeat-5 and 30% for C-Cap) as deduced from HP-NMR.[251]

Conclusions

The pressure-dependent SAXS measurements of the WT-PP32 in the presence of 1.5 M urea showed a complete unfolding of the wildtype protein with pressure for all three temperatures studied. This unfolding was accompanied by a dublication in the radius of gyration. The derived unfolding curves showed a slight pressure-stabilization with rising temperature, as may be expected for a protein exhibiting an elliptical p,T-stability diagram. By combining high pressure SAXS with 2D NMR, we have shown that mutations in the capping motifs of a leucine-rich repeat protein strongly effect the folding cooperativity of the PP32. These effects depend on the structural and energetic context of the mutations within the protein. If the N-terminal capping motif is deleted, the folding/unfolding behaviour becomes highly non-cooperative. NMR measurements showed a bimodal manner of the unfolding of the protein, i.e., the N-terminal half unfolds at much lower pressure than the C-terminal half. Indeed, HP SAXS showed that the stable C-terminal half of the protein did not completely unfold at the highest pressures attained. Deletion of the N-cap further destabilizes the N-terminal half of the protein, leading to a larger difference in stability between the stable C-terminal half of the protein and the less stable N-terminal half. As a consequence, a highly non-cooperative un/folding behavior is observed.

6.3 Actin bundles

6.3.1 Introduction

While the last subchapters focused on the form factor of single peptides and proteins, respectively, this subchapter focuses on the diffraction originating from a complex network of proteins. Actin filaments are bundled to form B-actin using two different condensation agents. The first one are divalent magnesium cations found to bundle F-actin *in vitro*, the second one is fascin, a protein cross-linking actin filaments *in vivo*. The temperature and pressure stability of these two types of bundles is investigated. This project was performed in close collaboration with Mimi Gao (TU-Dortmund), who performed corresponding SDS-PAGE and TEM analyses. The results were published in *Angewandte Chemie*[213] and are partially reproduced in this subchapter with permission,

6.3.2 Materials and methods

G-actin and fascin were purchased from Hypermol (Bielefeld, Germany). G-actin dissolved in 2 mM Tris-Cl pH 8.2, 0.4 mM ATP, 0.1 mM DTT, 0.08 mM $CaCl_2$ was polymerized by adding F-buffer (10 mM imidazole pH 7.4, 100 mM KCl, 1 mM ATP) to the solution. After 30 min of incubation at RT, F-actin was further bundled either by adding appropriate amount of fascin (molar ratio of 1:4 fascin to actin) or 50 mM $MgCl_2$ to the solution. The bundles were analyzed within one week after preparation. Meanwhile they were stored a 0°C. For all SAXS experiments performed, the actin concentration was 10 mg/mL.

Temperature-dependent measurements were performed on a SAXSess mc² instrument (Anton Paar, Graz, Austria) using a monochromatic X-ray beam (λ = 0.154 nm) with line focus and an imaging plate detector (Cyclone, Perkin Elmer, USA). 2D scattering patterns were integrated to obtain one-dimensional scattering intensities $I(q)$ as a function of the scattering vector, q, using SAXSquant 3.1 (Anton Paar, provided with the instrument). The same software was used for background correction of the data using the scattering profiles of the pure solvent. Scattering patterns were collected over 30 min per image. Desmearing of the data and calculation of the pair-distance distribution functions, $P(r)$, were performed using the software GNOM[249].

Pressure-dependent measurements were performed using a home-built high pressure cell with diamond windows[252] at Beamline ID02 at the European Synchrotron Radiation Facility in Grenoble, France. The sample volume was 10 µL. The energy used was 16 keV and the sample to detector distance was 1.5 m. The samples were exposed to the beam for 0.2 s for each measurement. No radiation damages were detected within the total exposure time of a complete pressure series. The diffraction data was background corrected and analyzed using the SAXSutilities[215] software package provided by ESRF and the peak maxima were obtained from Gaussian fits using the software Origin (OriginLab, Northampton, MA).

6.3.3 Results and discussion

Temperature-dependent SAXS measurements

Small-angle X-ray intensity profiles were recorded for different temperatures at atmospheric pressure (Figure 6-6). At the temperature of 20°C, for both types of bundles peaks indicating a hexagonal packing of the filaments are visible.[208] For the fascin-induced bundles these are the first one at the position q_{10} = 0.585 nm^{-1} associated with a hexagonal lattice constant $d = 4\pi/\sqrt{3}q_{10}$ of 12.4 nm (Figure 6-6 A) and second peak at the position q_{20} = 1.20 nm^{-1}. The ratio of the peak positions (1:2) indicates a perfect hexagonal packing of the fascin-connected bundles, in accordance to literature data.[208]

The peak intensity decreases drastically between 52.5°C and 55°C, indicating a melting/degradation temperature, T_{M}, of the bundles of about 54°C. With increasing temperature, the peak position and thus the lattice constant, d, does not change markedly. A small (0.3 nm) decrease is observed from 20 to 40°C, only, and the d-value starts to increase again above 50°C when dissociation of the bundles sets in (Figure A14). From 55 to 70°C, the SAXS intensity profiles resemble the scattering pattern of F-actin,[208] in agreement with the scattering pattern of randomly orientated F-actin as displayed in Figure A15. Both SAXS profiles show a slight increase of the intensity in the q-range where broad diffraction peaks associated with the helical structure of F-actin were found in ordered F-actin bundles (at 1.14 and 1.25 nm^{-1}).[208] However, our data indicate that the thermal degradation of bundles proceeds via the dissociation of the filaments.

From 70°C to 80°C, a further change of the SAXS profile can be observed (Figure 6-6 A, Figure A15 A), which is similar to the change in the scattering curve of filamentous actin upon thermal denaturation with a T_M of 75°C.[253] These changes include a drastic increase of scattering at low q-values, which is indicative of protein aggregation. The according pair-distance distribution function, $P(r)$, suggest a transition from a cylindrical, elongated species to slightly elongated aggregates with a radius of gyration of about 10 nm (Figure A15 B).

The SAXS profile of Mg^{2+}-induced bundles at 20°C reveals a first-order peak at q_{10} at 0.85 nm^{-1} and a weak higher-order peak at 1.36 nm^{-1} (Figure 6-6 B). The ratio of the two peaks (1:1.6) differs slightly from the 1:$\sqrt{3}$ ratio expected for a perfect hexagonal packing. The first-order peak is associated with a hexagonal lattice constant of 8.5 nm, which reflects closest packing of the filaments.[254]

No significant shift of the diffraction peaks and hence the d-value is observed with increasing temperature up to 40°C (Figure A14). The peak intensity drastically decreases between 65°C and 67.5°C, indicating a melting temperature of the Mg^{2+}-induced actin bundles of about 66°C, which is in good agreement with FTIR spectroscopic measurements.[253]

In contrast to the fascin-induced bundles, a scattering profile reflecting the characteristics of filamentous actin cannot be observed at any temperature. Instead, the scattering profiles of the Mg^{2+}-induced bundles above 65°C suggests direct formation of amorphous actin aggregates from the bundles. This behavior was confirmed by TEM analysis.[213]

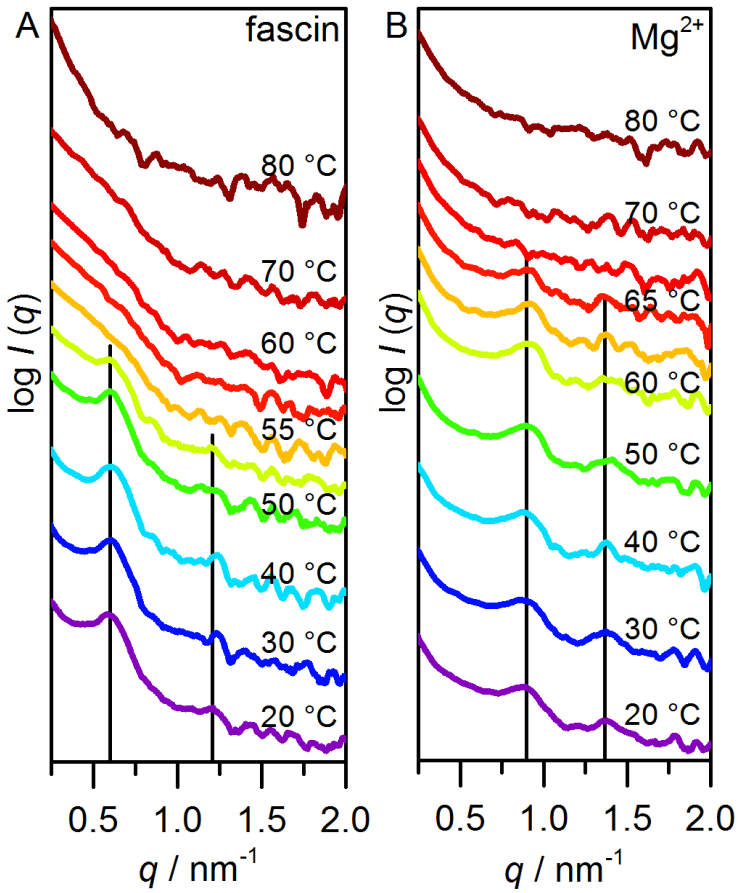

Figure 6-6. Temperature-dependent SAXS intensity profiles of B-actin. Bundling of F-actin was induced with fascin (A) or Mg2+ ions (B). Black solid lines indicate the position of the peak maxima related to hexagonal packing of filaments at 20°C (A and B). Curves were shifted for clarity.

Pressure-dependent SAXS measurements

Studying the response of fascin- and Mg^{2+}-induced actin bundles to high hydrostatic pressure with SAXS reveals that these actin bundles are present up to a pressure of about 250 and 160 MPa, respectively (Figure 6-7). For fascin-induced bundles, the peak position does not change significantly from 0.1 up to a pressure of 125 MPa, while between 125 and 250 MPa a marked shift towards lower q-values is observed (Figure 6-7 A). The calculated lattice constant, $d(p)$, shows a total increase of the intermolecular distance between the filaments of ~0.6 nm between 125 and 250 MPa (Figure 6-7 C). After dissociation, from about 250 MPa up to the maximum pressure of 400 MPa, the observed intensity profile monitored is characteristic for F-actin filaments.

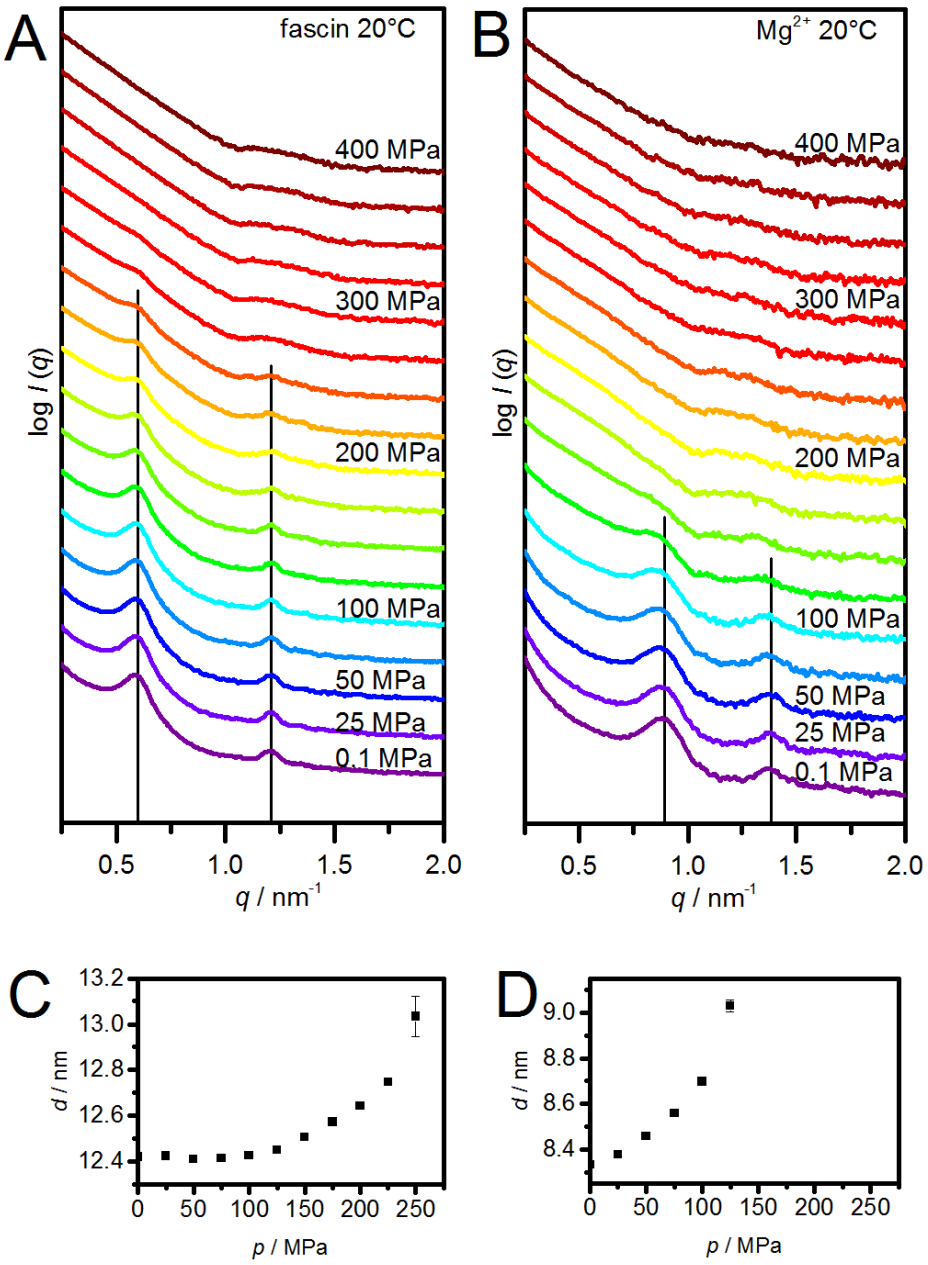

Figure 6-7. Pressure-dependent Synchrotron small-angle X-ray scattering data of B-actin at 20°C. Bundling of the F-actin was induced with fascin (A and C) or Mg^{2+} ions (B and D). (A and B) Intensity profiles are shown with black solid lines indicating the position of the peak maxima related to a hexagonal packing of the filaments at 0.1 MPa. Curves were shifted for clarity. (C and D) Pressure-dependent changes of the lattice constant.

In contrast, the scattering intensity profiles of the Mg^{2+}-induced actin bundles (Figure 6-7 B) and the pressure-dependent changes of the lattice constant (Figure 6-7 D) show a continuous shift of the q_{10}-peak towards lower q-values up to the dissociation pressure. The lattice constant, d, experiences a total increase of about 0.6 nm. The scattering intensity profile at 150 MPa is characteristic of F-actin. Upon further

compression, the overall intensity of the scattering curve decreases, indicating formation of smaller filamentous species. An increase in temperature to 30°C (Figure A16) leads to a drastic decrease in pressure stability of the fascin-induced bundles. In this case, the peaks characteristic for bundles can be monitored up to a pressure of 125-160 MPa, only. For the Mg^{2+}-induced bundles, the effect of temperature on the pressure stability is much weaker. The observed denaturation pressure is around 160 MPa for all temperatures between 20 and 45°C (Figure A16 B and C).

The d-values seem to diverge upon approaching a critical pressure value (Figure 6-7 C and D). This behavior resembles an unbinding transition, which was also reported for other soft elastic manifolds, for example for stacks of lipid bilayer membranes.[232–234] The origin of such a transition is the competition of attractive molecular interactions and an effective repulsion between the filaments reflecting the loss of configurational entropy the filaments experience in the bound state. *Lipowski* and *Leibler* reported the existence of a certain threshold. Below this threshold, the entropically driven undulations are stronger than the attractive forces, resulting in a complete unbinding. Here, the apparent divergence of the d-value approaching a critical pressure value points towards a similar unbinding scenario, that is $\langle d \rangle \propto (p_c - p)^{-\alpha}$ with an exponent α.

Fascin or Mg^{2+} induce an interplay of steric / electrostatic repulsion and attractions, which determines whether the filaments stay in the bundled state or unbind. Pressure induces destabilization of the bridging fascin molecules and weakens the electrostatic interactions in the Mg^{2+}-induced bundles, respectively. If this scaling behavior applies, this leads to a critical exponent, α, of about 0.06 and to critical unbinding pressures, p_c, of about 310 MPa for the fascin- and 160 MPa for the Mg^{2+}-induced actin bundles, respectively. These values agree with our experimental data. Interestingly, theoretical studies predicted such an unbinding scenario for bundles of semiflexible polymers such as actin filaments. The formation of bundles of parallel filaments needs a threshold concentration of cross-linkers and the bundles unbind in a single, discontinuous transition, as shown by *Kierfeld et al.*.[255,256] In this work, pressure modulates the critical concentration of active linker molecules. Theoretical studies predicted the criticality observed here.[255,256]

Interestingly, *in situ* HP-SAXS measurements show the presence of highly ordered Mg^{2+}-induced bundles up to a pressure of ~125 MPa, only. In contrast, *ex situ* TEM images show no morphological changes up to 150 MPa. This observation might be explained by a reversible pressure dissociation and therefore reassembly of the filaments when the pressure is released.[213] Pressure effects on electrostatic interactions might be responsible for this observation. The disruption of internal salt bridges reduces the overall volume of the bundles. When pressure is increased, water molecules form a dense hydration shell around the solvent-exposed ions (electrostrictive effect).[87–89]Thus, the attenuation of electrostatic interactions leads to an increase of the distance between the filaments as observed in SAXS.

Conclusions

All in all, the results show that fascin- and Mg^{2+}-induced bundles of F-actin establish different temperature and pressure stabilities. The two types of bundle structures are stabilized by different intermolecular interactions. Below T_M, neither the fascin-actin interaction nor counterion organization are very sensitive to thermal fluctuations. However, electrostatic interactions are weakened by high hydrostatic pressures.[87–89] For Mg^{2+}-induced bundles, the lateral condensation of F-actin is dominated by electrostatic interactions, which are weakened by pressure, resulting in the dissociation of the bundle structure. Thereby, packing defects are likely to be a minor factor, due to closest packing of the filaments in the Mg^{2+}-bundles and a small pressure-induced volume change upon disintegration.[253]

However, the distance between the filaments of the fascin-induced bundles is not affected upon pressurization up to ~100 MPa. Only above ~250 MPa, dissociation of the bundles is observed, indicating that additional, non-electrostatic interactions occur between the fascin and actin. It was shown that F-actin is stable up to the pressure range of 350 MPa.[253] Therefore, destabilization of the tertiary structure of fascin and its local interaction site with F-actin is likely to be responsible for the dissociation of the fascin-stabilized bundles occurring at a pressure much lower than 350 MPa. In comparison with the divalent Mg^{2+}-stabilized bundles, the pressure stability fascin-induced bundles is drastically higher. Both proteins, actin and fascin, are evolutionary highly conserved.[257,258] Thus, bundles formed by them might fit better the requirements inside cells of organisms living under extreme environmental conditions, as found in the deep sea, where pressures up to ~110 MPa are

encountered.[38] The evolutionary evolved actin-binding proteins, such as fascin, are required to ensure sufficient stability and mechanical resistance of the cytoskeleton under such harsh environmental conditions.

Summary

The measurements presented in this thesis provided many new insights and contributed significantly to various projects. Scattering methods were applied to study various systems of biomolecules. These measurements do not require any labeling or modification of the molecules and can be performed in a wide range of temperatures and pressures. Thus, they are ideal tools to gain interesting insights into the structural changes of the molecules under investigation at various conditions of temperature and pressure. Many of these conditions aimed to mimicking deep sea habitats, which might have been the place where life emerged. These scattering methods also enabled to study the influence of cosolutes like TMAO, urea and divalent ions on the temperature and pressure stability of the systems, which might have been present in the primordial soup.

The first class of biomolecules under investigation was lipids. SAXS measurements on a mixture containing different prebiotic lipids provided insights on how the first membrane envelopes of protocells might have evolved. They enabled to investigate the micelle-vesicle equilibrium of this system. It showed that the vesicular structures are not only highly temperature stable, but also that pressure fosters the formation of vesicles from micelles. XRR and SAXS measurements on a bicontinuous microemulsion showed that this emulsion forms a lamellar layer in proximity to a Si-wafer. Right on the surface, 2-3 layers of water molecules were found. These measurements further showed that pressure compresses the lamellar phase. In the bicontinuous phase, pressure increases the order, but this ordering is not sufficient to induce a transition to a lamellar phase up to 400 MPa, which would be associated with a high loss in entropy.

Next, the behavior of nucleic acids was explored. Measurements on guanosine monophosphate sodium salt showed that even single nucleotides can have a very complex phase behavior, which strongly depends on temperature, pressure and the presence of cosolutes. Interestingly, the stabilizing cosolute TMAO was found to induce hexagonal association of the stacks even in the absence of stabilizing cations. Measurements on a labeled small RNA hairpin motive showed how drastically fluorophores can impact the temperature and pressure stability of small molecules. The SAXS measurements were able to resolve the stacking interaction between the fluorophore and the nucleobases. SAXS measurements also showed that the radius

of gyration of the hairpin ribozyme decreases with pressure, which indicates an increased population of the docked state. This shows that pressure could be favorable for enzymatic reaction involving ribozymes, which might have been precursors to modern enzymes. The time-dependent cleavage could not be resolved due to problems with aggregation at the relatively high concentrations required for this small-angle X-ray scattering measurements. SAXS measurements on the phenylalanine transfer RNA showed that magnesium ions enhance the cooperativity in temperature induced unfolding. Further, these measurements revealed high pressure stability of $tRNA^{Phe}$, both, in the absence and presence of magnesium.

Finally, SAXS measurements on peptides and proteins were conducted. For the elastin-like peptide, the experiments showed that the cosolute TFE seems to bind to the surface of the ELP. The measurements on WT-PP32 and its mutants showed that mutations in the capping motives decrease the cooperativity of the unfolding in the whole protein. They showed that the C-terminal of the PP32-ΔN-cap remains at least partially folded even at the highest pressure investigated. Diffraction measurements on the hexagonally arranged filaments within actin bundles showed that using fascin as a crosslinker instead of divalent ions significantly enhances the pressure stability of the bundles. Further, the analysis of the hexagonal lattice constant in dependence of pressure showed that the filaments undergo an unbinding transition.

References

1. Trevors, J. T. Early assembly of cellular life. *Prog. Biophys. Mol. Biol.* **81,** 201–217 (2003).
2. Winter, R. & Jeworrek, C. Effect of pressure on membranes. *Soft Matter* **5,** 3157–3173 (2009).
3. Cech, T. R. The RNA Worlds in Context. *Cold Spring Harb. Perspect. Biol.* **4,** a006742–a006742 (2012).
4. Winter, R. & Noll, F. *Methoden der Biophysikalischen Chemie*. (Vieweg+Teubner Verlag, 1998).
5. Guinier, A. & Fournet, G. *Small-angle scattering of X-rays*. (Wiley, 1955).
6. Glatter, O. & Kratky, O. *Small Angle X-ray Scattering*. (Academic Press, 1982).
7. Feigin, L. A. & Svergun, D. I. *Structure Analysis by Small-Angle X-Ray and Neutron Scattering*. (Plenum Press, 1987).
8. Lindner, P. & Zemb, T. *Neutron, X-rays and Light. Scattering Methods Applied to Soft Condensed Matter*. (North Holland, 2002).
9. Svergun, D. I. & Koch, M. H. J. Small-angle scattering studies of biological macromolecules in solution. *Reports Prog. Phys.* **66,** 1735–1782 (2003).
10. Putnam, C. D., Hammel, M., Hura, G. L. & Tainer, J. A. X-ray solution scattering (SAXS) combined with crystallography and computation: defining accurate macromolecular structures, conformations and assemblies in solution. *Q. Rev. Biophys.* **40,** 191–285 (2007).
11. Stribeck, N. *X-Ray Scattering of Soft Matter*. (Springer-Verlag, 2007).
12. Daillant, J. & Gibaud, A. *X-ray and Neutron Reflectivity*. (Springer-Verlag, 2009).
13. Als-Nielsen, J. & McMorrow, D. *Elements of Modern X-ray Physics*. (John Wiley & Sons, 2011).
14. Svergun, D. I., Koch, M. H. J., Timmins, P. A. & May, R. P. *Small Angle X-Ray and Neutron Scattering from Solutions of Biological Macromolecules*. (Oxford University Press, 2013).
15. Koch, M. H., Vachette, P. & Svergun, D. I. Small-angle scattering: a view on the properties, structures and structural changes of biological macromolecules in solution. *Q. Rev. Biophys.* **36,** 147–227 (2003).
16. Lipfert, J. & Doniach, S. Small-Angle X-Ray Scattering from RNA, Proteins, and Protein Complexes. *Annu. Rev. Biophys. Biomol. Struct.* **36,** 307–327 (2007).
17. Dainese, E., Sabatucci, A. & Cozzani, I. Small Angle X-Ray Scattering: A Powerful Tool to Analyze Protein Conformation in Solution. *Curr. Org. Chem.* **9,** 1781–1800 (2005).
18. Dingley, A.J., Pascal, S. M. *Biomolecular NMR spectroscopy*. (IOS Press, 2011).

19. Debye, P. Zerstreuung von Röntgenstrahlen. *Ann. Phys.* **351,** 809–823 (1915).

20. Porod, G. Die Röntgenkleinwinkelstreuung von dichtgepackten kolloiden Systemen. *Kolloid-Zeitschrift* **124,** 83–114 (1951).

21. Guinier, A. La Diffraction des rayons x aux très petits angles: application à l'étude des phénomènes ultramicroscopiques. *Ann. Phys.* **12,** 161–237 (1939).

22. Debye, P. & Bueche, A. M. Scattering by an Inhomogeneous Solid. *J. Appl. Phys.* **20,** 518–525 (1949).

23. Feigin, L. A. & Svergun, D. I. *Structure Analysis by Small-Angle X-Ray and Neutron Scattering*. (Springer US, 1987).

24. Chacón, P., Morán, F., Díaz, J. F., Pantos, E. & Andreu, J. M. Low-Resolution Structures of Proteins in Solution Retrieved from X-Ray Scattering with a Genetic Algorithm. *Biophys. J.* **74,** 2760–2775 (1998).

25. Svergun, D. I. Restoring low resolution structure of biological macromolecules from solution scattering using simulated annealing. *Biophys. J.* **76,** 2879–2886 (1999).

26. Svergun, D. I., Petoukhov, M. V. & Koch, M. H. J. Determination of Domain Structure of Proteins from X-Ray Solution Scattering. *Biophys. J.* **80,** 2946–2953 (2001).

27. Lipfert, J., Chu, V. B., Bai, Y., Herschlag, D. & Doniach, S. Low-resolution models for nucleic acids from small-angle X-ray scattering with applications to electrostatic modeling. *J. Appl. Crystallogr.* **40,** s229–s234 (2007).

28. Teubner, M. & Strey, R. Origin of the scattering peak in microemulsions. *J. Chem. Phys.* **87,** 3195–3200 (1987).

29. Parratt, L. G. Surface Studies of Solids by Total Reflection of X-Rays. *Phys. Rev.* **95,** 359–369 (1954).

30. Tolan, M. *X-Ray Scattering from Soft-Matter Thin Films*. (Springer-Verlag, 1999).

31. Berghaus, M. *et al.* Near-Surface and Bulk Behavior of Bicontinuous Microemulsions under High-Pressure Conditions. *J. Phys. Chem. B* **120,** 7148–7153 (2016).

32. Krywka, C. *et al.* Effect of Osmolytes on Pressure-Induced Unfolding of Proteins: A High-Pressure SAXS Study. *ChemPhysChem* **9,** 2809–2815 (2008).

33. Wirkert, F. J. *et al.* X-ray reflectivity measurements of liquid/solid interfaces under high hydrostatic pressure conditions. *J. Synchrotron Radiat.* **21,** 76–81 (2014).

34. Woenckhaus, J., Köhling, R., Winter, R., Thiyagarajan, P. & Finet, S. High pressure-jump apparatus for kinetic studies of protein folding reactions using the small-angle synchrotron x-ray scattering technique. *Rev. Sci. Instrum.* **71,** 3895–3899 (2000).

35. Kraineva, J., Narayanan, R. A., Kondrashkina, E., Thiyagarajan, P. & Winter, R. Kinetics of lamellar-to-cubic and intercubic phase transitions of pure and

cytochrome c containing monoolein dispersions monitored by time-resolved small-angle X-ray diffraction. *Langmuir* **21,** 3559–3571 (2005).

36. Krywka, C. *et al.* The new diffractometer for surface X-ray diffraction at beamline BL9 of DELTA. *J. Synchrotron Radiat.* **13,** 8–13 (2006).

37. Paulus, M. *et al.* An access to buried interfaces: the X-ray reflectivity set-up of BL9 at DELTA. *J. Synchrotron Radiat.* **15,** 600–605 (2008).

38. Daniel, I., Oger, P. & Winter, R. Origins of life and biochemistry under high-pressure conditions. *Chem. Soc. Rev.* **35,** 858–875 (2006).

39. Simoneit, B. R. T. Prebiotic organic synthesis under hydrothermal conditions: an overview. *Adv. Sp. Res.* **33,** 88–94 (2004).

40. Leslie E., O. Prebiotic Chemistry and the Origin of the RNA World. *Crit. Rev. Biochem. Mol. Biol.* **39,** 99–123 (2004).

41. Deamer, D., Dworkin, J. P., Sandford, S. a, Bernstein, M. P. & Allamandola, L. J. The First Cell Membranes. *Astrobiology* **2,** 371–381 (2002).

42. Schrum, J. P., Zhu, T. F. & Szostak, J. W. The Origins of Cellular Life. *Cold Spring Harb. Perspect. Biol.* **2,** a002212–a002212 (2010).

43. Yancey, P. H., Blake, W. R. & Conley, J. Unusual organic osmolytes in deep-sea animals: adaptations to hydrostatic pressure and other perturbants. *Comp. Biochem. Physiol. Part A Mol. Integr. Physiol.* **133,** 667–676 (2002).

44. Timasheff, S. N. Protein-solvent preferential interactions, protein hydration, and the modulation of biochemical reactions by solvent components. *Proc. Natl. Acad. Sci.* **99,** 9721–9726 (2002).

45. Yancey, P. H. Organic osmolytes as compatible, metabolic and counteracting cytoprotectants in high osmolarity and other stresses. *J. Exp. Biol.* **208,** 2819–2830 (2005).

46. Minton, A. P. The Influence of Macromolecular Crowding and Macromolecular Confinement on Biochemical Reactions in Physiological Media. *J. Biol. Chem.* **276,** 10577–10580 (2001).

47. Kadam, P. S., Jadhav, B. A., Salve, R. V & Machewad, G. M. Review on the High Pressure Technology (HPT) for Food Preservation. *Food Process. Technol.* **3,** 1–5 (2012).

48. Alberts, B. *et al. Molecular Biology of the Cell*. (Garland Science, 2002).

49. McCollom, T. M., Ritter, G. & Simoneit, B. R. Lipid synthesis under hydrothermal conditions by Fischer-Tropsch-type reactions. *Orig. Life Evol. Biosph.* **29,** 153–166 (1999).

50. Hanczyc, M. M., Fujikawa, S. M. & Szostak, J. W. Experimental models of primitive cellular compartments: encapsulation, growth, and division. *Science (80-.).* **302,** 618–622 (2003).

51. Szostak, J. W., Bartel, D. P. & Luisi, P. L. Synthesizing life. *Nature* **409,** 387–390 (2001).

52. Yuen, G. U. & Kvenhold, K. A. Monocarboxylic Acids in Murray and Murchison

Carbonaceous Meteorites. *Nature* **246,** 301–303 (1973).

53. Deamer, D. W. Boundary structures are formed by organic components of the Murchison carbonaceous chondrite. *Nature* **317,** 792–794 (1985).

54. Budin, I., Debnath, A. & Szostak, J. W. Concentration-Driven Growth of Model Protocell Membranes. *J. Am. Chem. Soc.* **134,** 20812–20819 (2012).

55. Kulkarni, C. V, Wachter, W., Iglesias-Salto, G., Engelskirchen, S. & Ahualli, S. Monoolein: a magic lipid? *Phys. Chem. Chem. Phys.* **13,** 3004–3021 (2011).

56. Winter, R. & Köhling, R. Static and time-resolved synchrotron small-angle x-ray scattering studies of lyotropic lipid mesophases, model biomembranes and proteins in solution. *J. Phys. Condens. Matter* **16,** S327–S352 (2004).

57. Winter, R. & Czeslik, C. Pressure effects on the structure of lyotropic lipid mesophases and model biomembrane systems. *Zeitschrift für Krist. - Cryst. Mater.* **215,** 454–474 (2000).

58. Seddon, J. M. Structure of the inverted hexagonal (HII) phase, and non-lamellar phase transitions of lipids. *Biochim. Biophys. Acta - Rev. Biomembr.* **1031,** 1–69 (1990).

59. Gruner, S. M., Cullis, P. R., Hope, M. J. & Tilcock, C. P. Lipid polymorphism: the molecular basis of nonbilayer phases. *Annu. Rev. Biophys. Biophys. Chem.* **14,** 211–238 (1985).

60. Lipowsky, R. & Sackmann, E. *Structure and Dynamics of Membranes*. (Elsevier Science, 1995).

61. Czeslik, C., Reis, O., Winter, R. & Rapp, G. Effect of high pressure on the structure of dipalmitoylphosphatidylcholine bilayer membranes: a synchrotron-X-ray diffraction and FT-IR spectroscopy study using the diamond anvil technique. *Chem. Phys. Lipids* **91,** 135–144 (1998).

62. Hyde, S. *et al. The Language of Shape*. (Elsevier, 1997).

63. Almsherqi, Z. a, Kohlwein, S. D. & Deng, Y. Cubic membranes: a legend beyond the Flatland of cell membrane organization. *J. Cell Biol.* **173,** 839–844 (2006).

64. Tenchov, B. & Koynova, R. Cubic phases in membrane lipids. *Eur. Biophys. J.* **41,** 841–850 (2012).

65. Kapoor, S. *et al.* Prebiotic cell membranes that survive extreme environmental pressure conditions. *Angew. Chem. Int. Ed. Engl.* **53,** 8397–8401 (2014).

66. Cossins, A. R. & Macdonald, A. G. The adaptation of biological membranes to temperature and pressure: Fish from the deep and cold. *J. Bioenerg. Biomembr.* **21,** 115–135 (1989).

67. Yayanos, A. A. Evolutional and ecological implications of the properties of deep-sea barophilic bacteria. *Proc. Natl. Acad. Sci.* **83,** 9542–9546 (1986).

68. Behan, M. K., Macdonald, A. G., Jones, G. R. & Cossins, A. R. Homeoviscous adaptation under pressure: the pressure dependence of membrane order in brain myelin membranes of deep-sea fish. *Biochim. Biophys. Acta* **1103,** 317–323 (1992).

69. Monnard, P.-A. & Deamer, D. W. *Preparation of Vesicles from Nonphospholipid Amphiphiles*. *Methods in enzymology* (Elsevier, 2003).

70. Monnard, P.-A., Apel, C. L., Kanavarioti, A. & Deamer, D. W. Influence of Ionic Inorganic Solutes on Self-Assembly and Polymerization Processes Related to Early Forms of Life: Implications for a Prebiotic Aqueous Medium. *Astrobiology* **2,** 139–152 (2002).

71. Apel, C. L., Deamer, D. W. & Mautner, M. N. Self-assembled vesicles of monocarboxylic acids and alcohols: conditions for stability and for the encapsulation of biopolymers. *Biochim. Biophys. Acta - Biomembr.* **1559,** 1–9 (2002).

72. Hargreaves, W. R. & Deamer, D. W. Liposomes from ionic, single-chain amphiphiles. *Biochemistry* **17,** 3759–3768 (1978).

73. Anneken, D. J. *et al. Fatty Acids*. *Ullmann's Encyclopedia of Industrial Chemistry* (Wiley, 2006).

74. Conn, C. E. *et al.* Dynamics of Structural Transformations between Lamellar and Inverse Bicontinuous Cubic Lyotropic Phases. *Phys. Rev. Lett.* **96,** 108102–108104 (2006).

75. Cherezov, V., Siegel, D. P., Shaw, W., Burgess, S. W. & Caffrey, M. The Kinetics of Non-Lamellar Phase Formation in DOPE-Me: Relevance to Biomembrane Fusion. *J. Membr. Biol.* **195,** 165–182 (2003).

76. Lendermann, J. & Winter, R. Interaction of cytochrome c with cubic monoolein mesophases at limited hydration conditions: The effects of concentration, temperature and pressure. *Phys. Chem. Chem. Phys.* **5,** 1440–1450 (2003).

77. Chen, S. H., Chang, S. L., Strey, R., Samseth, J. & Mortensen, K. Structural evolution of bicontinuous microemulsions. *J. Phys. Chem.* **95,** 7427–7432 (1991).

78. Kerscher, M. *et al.* Near-surface structure of a bicontinuous microemulsion with a transition region. *Phys. Rev. E. Stat. Nonlin. Soft Matter Phys.* **83,** 30401 (2011).

79. Zhou, X.-L., Lee, L.-T., Chen, S.-H. & Strey, R. Observation of surface-induced layering in bicontinuous microemulsions. *Phys. Rev. A* **46,** 6479–6489 (1992).

80. Frielinghaus, H. *et al.* Scattering depth correction of evanescent waves in inelastic neutron scattering using a neutron prism. *Nucl. Instruments Methods Phys. Res. Sect. A Accel. Spectrometers, Detect. Assoc. Equip.* **686,** 71–74 (2012).

81. Frielinghaus, H., Kerscher, M., Holderer, O., Monkenbusch, M. & Richter, D. Acceleration of membrane dynamics adjacent to a wall. *Phys. Rev. E - Stat. Nonlinear, Soft Matter Phys.* **85,** 1–7 (2012).

82. Köhling, R., Woenckhaus, J., Klyachko, N. L. & Winter, R. Small-Angle Neutron Scattering Study of the Effect of Pressure on AOT− n -Octane−Water Mesophases and the Effect of α-Chymotrypsin Incorporation. *Langmuir* **18,** 8626–8632 (2002).

83. Swami, A. *et al.* Confinement of DNA in water-in-oil microemulsions. *Langmuir*

24, 11828–11833 (2008).

84. Lawrence, M. J. & Rees, G. D. Microemulsion-based media as novel drug delivery systems. *Adv. Drug Deliv. Rev.* **45,** 89–121 (2000).

85. Mathews, D. H. *et al.* Incorporating chemical modification constraints into a dynamic programming algorithm for prediction of RNA secondary structure. *Proc. Natl. Acad. Sci.* **101,** 7287–7292 (2004).

86. Tan, Z.-J. & Chen, S.-J. Salt dependence of nucleic acid hairpin stability. *Biophys. J.* **95,** 738–752 (2008).

87. Silva, J. L., Foguel, D. & Royer, C. a. Pressure provides new insights into protein folding, dynamics and structure. *Trends Biochem. Sci.* **26,** 612–618 (2001).

88. Mishra, R. & Winter, R. Cold- and Pressure-Induced Dissociation of Protein Aggregates and Amyloid Fibrils. *Angew. Chemie Int. Ed.* **47,** 6518–6521 (2008).

89. Akasaka, K. Probing Conformational Fluctuation of Proteins by Pressure Perturbation. *Chem. Rev.* **106,** 1814–1835 (2006).

90. Chong, P. L.-G., Ravindra, R., Khurana, M., English, V. & Winter, R. Pressure perturbation and differential scanning calorimetric studies of bipolar tetraether liposomes derived from the thermoacidophilic archaeon *Sulfolobus acidocaldarius*. *Biophys. J.* **89,** 1841–1849 (2005).

91. Chong, P. L.-G., Zein, M., Khan, T. K. & Winter, R. Structure and Conformation of Bipolar Tetraether Lipid Membranes Derived from Thermoacidophilic Archaeon Sulfolobus acidocaldarius as Revealed by Small-Angle X-ray Scattering and High-Pressure FT-IR Spectroscopy. *J. Phys. Chem. B* **107,** 8694–8700 (2003).

92. Kruger, K. *et al.* Self-splicing RNA: autoexcision and autocyclization of the ribosomal RNA intervening sequence of Tetrahymena. *Cell* **31,** 147–57 (1982).

93. Schimmel, P. & Kelley, S. O. Exiting an RNA world. *Nat. Struct. Biol.* **7,** 5–7 (2000).

94. Dubins, D. N., Lee, A., Macgregor, R. B. & Chalikian, T. V. On the Stability of Double Stranded Nucleic Acids. *J. Am. Chem. Soc.* **123,** 9254–9259 (2001).

95. Takahashi, S. & Sugimoto, N. Effect of Pressure on Thermal Stability of G-Quadruplex DNA and Double-Stranded DNA Structures. *Molecules* **18,** 13297–13319 (2013).

96. Girard, E. *et al.* Adaptation of the base-paired double-helix molecular architecture to extreme pressure. *Nucleic Acids Res.* **35,** 4800–4808 (2007).

97. Lin, M.-C., Eid, P., Wong, P. T. T. & Macgregor, R. B. High pressure fourier transform infrared spectroscopy of poly(dA)poly(dT), poly(dA) and poly(dT). *Biophys. Chem.* **76,** 87–94 (1999).

98. Roche, J. *et al.* Cavities determine the pressure unfolding of proteins. *Proc. Natl. Acad. Sci.* **109,** 6945–6950 (2012).

99. Takahashi, S. & Sugimoto, N. Effect of Pressure on the Stability of G-

Quadruplex DNA: Thermodynamics under Crowding Conditions. *Angew. Chemie* **125,** 14019–14023 (2013).

100. Wilton, D. J., Ghosh, M., Chary, K. V. A., Akasaka, K. & Williamson, M. P. Structural change in a B-DNA helix with hydrostatic pressure. *Nucleic Acids Res.* **36,** 4032–4037 (2008).

101. Giel-Pietraszuk, M. & Barciszewski, J. A nature of conformational changes of yeast tRNAPhe. *Int. J. Biol. Macromol.* **37,** 109–114 (2005).

102. Giel-Pietraszuk, M. & Barciszewski, J. Hydrostatic and osmotic pressure study of the RNA hydration. *Mol. Biol. Rep.* **39,** 6309–6318 (2012).

103. Hughes, F. & Steiner, R. F. Effects of pressure on the helix-coil transitions of the poly A-poly U system. *Biopolymers* **4,** 1081–1090 (1966).

104. Garcia, A. E. & Paschek, D. Simulation of the Pressure and Temperature Folding/Unfolding Equilibrium of a Small RNA Hairpin. *J. Am. Chem. Soc.* **130,** 815–817 (2008).

105. Downey, C. D., Crisman, R. L., Randolph, T. W. & Pardi, A. Influence of Hydrostatic Pressure and Cosolutes on RNA Tertiary Structure. *J. Am. Chem. Soc.* **129,** 9290–9291 (2007).

106. Hervé, G., Tobé, S., Heams, T., Vergne, J. & Maurel, M.-C. Hydrostatic and osmotic pressure study of the hairpin ribozyme. *Biochim. Biophys. Acta - Proteins Proteomics* **1764,** 573–577 (2006).

107. Kaddour, H., Vergne, J., Hervé, G. & Maurel, M.-C. High-pressure analysis of a hammerhead ribozyme from Chrysanthemum chlorotic mottle viroid reveals two different populations of self-cleaving molecule. *FEBS J.* **278,** 3739–3747 (2011).

108. Lane, A. N., Chaires, J. B., Gray, R. D. & Trent, J. O. Stability and kinetics of G-quadruplex structures. *Nucleic acids research* **36,** 5482–5515 (2008).

109. Chan, S. R. W. L. & Blackburn, E. H. Telomeres and telomerase. *Philos. Trans. R. Soc. B Biol. Sci.* **359,** 109–122 (2004).

110. Cech, T. R. Beginning to understand the end of the chromosome. *Cell* **116,** 273–279 (2004).

111. Lipps, H. J. & Rhodes, D. G-quadruplex structures: in vivo evidence and function. *Trends Cell Biol.* **19,** 414–422 (2009).

112. Simonsson, T. G-Quadruplex DNA Structures Variations on a Theme. *Biol. Chem.* **382,** 621–628 (2001).

113. Mergny, J. L. *et al.* The development of telomerase inhibitors: the G-quartet approach. *Anticancer. Drug Des.* **14,** 327–339 (1999).

114. Mariani, P., Ciuchi, F. & Saturni, L. Helix-Specific Interactions Induce Condensation of Guanosine Four-Stranded Helices in Concentrated Salt Solutions. *Biophys. J.* **74,** 430–435 (1998).

115. Ausili, P. *et al.* Pressure Effects on Columnar Lyotropics: Anisotropic Compressibilities in Guanosine Monophosphate Four-Stranded Helices. *J. Phys. Chem. B* **108,** 1783–1789 (2004).

116. Mariani, P. *et al.* Guanosine Quadruplexes in Solution: A Small-Angle X-Ray Scattering Analysis of Temperature Effects on Self-Assembling of Deoxyguanosine Monophosphate. *J. Nucleic Acids* **2010,** 1–10 (2010).

117. Mariani, P. & Saturni, L. Measurement of intercolumnar forces between parallel guanosine four-stranded helices. *Biophys. J.* **70,** 2867–2874 (1996).

118. Wong, A. & Wu, G. Selective Binding of Monovalent Cations to the Stacking G-Quartet Structure Formed by Guanosine 5'-Monophosphate: A Solid-State NMR Study. *J. Am. Chem. Soc.* **125,** 13895–13905 (2003).

119. Tuerk, C. *et al.* CUUCGG hairpins: extraordinarily stable RNA secondary structures associated with various biochemical processes. *Proc. Natl. Acad. Sci.* **85,** 1364–1368 (1988).

120. Uhlenbeck, O. C. Tetraloops and RNA folding. *Nature* **346,** 613–614 (1990).

121. Woese, C. R., Winker, S. & Gutell, R. R. Architecture of ribosomal RNA: constraints on the sequence of 'tetra-loops'. *Proc. Natl. Acad. Sci.* **87,** 8467–8471 (1990).

122. Wolters, J. The nature of preferred hairpin structures in 16S-like rRNA variable regions. *Nucleic Acids Res.* **20,** 1843–1850 (1992).

123. Varani, G. Exceptionally Stable Nucleic Acid Hairpins. *Annu. Rev. Biophys. Biomol. Struct.* **24,** 379–404 (1995).

124. Tinoco, I. & Bustamante, C. How RNA folds. *J. Mol. Biol.* **293,** 271–281 (1999).

125. Molinaro, M. & Tinoco, I. Use of ultra stable UNCG tetraloop hairpins to fold RNA structures: thermodynamic and spectroscopic applications. *Nucleic Acids Res.* **23,** 3056–3063 (1995).

126. Woese, C. R., Gutell, R., Gupta, R. & Noller, H. F. Detailed analysis of the higher-order structure of 16S-like ribosomal ribonucleic acids. *Microbiol. Rev.* **47,** 621–669 (1983).

127. Sheehy, J. P., Davis, A. R. & Znosko, B. M. Thermodynamic characterization of naturally occurring RNA tetraloops. *RNA* **16,** 417–429 (2010).

128. Chakraborty, D., Collepardo-Guevara, R. & Wales, D. J. Energy Landscapes, Folding Mechanisms, and Kinetics of RNA Tetraloop Hairpins. *J. Am. Chem. Soc.* **136,** 18052–18061 (2014).

129. Ma, H. *et al.* Exploring the Energy Landscape of a Small RNA Hairpin. *J. Am. Chem. Soc.* **128,** 1523–1530 (2006).

130. Ma, H., Wan, C., Wu, A. & Zewail, A. H. DNA folding and melting observed in real time redefine the energy landscape. *Proc. Natl. Acad. Sci. U. S. A.* **104,** 712–716 (2007).

131. Jung, J. & Van Orden, A. Folding and Unfolding Kinetics of DNA Hairpins in Flowing Solution by Multiparameter Fluorescence Correlation Spectroscopy. *J. Phys. Chem. B* **109,** 3648–3657 (2005).

132. Chen, A. A. & Garcia, A. E. High-resolution reversible folding of hyperstable RNA tetraloops using molecular dynamics simulations. *Proc. Natl. Acad. Sci.* **110,** 16820–16825 (2013).

133. Miner, J. C., Chen, A. A. & García, A. E. Free-energy landscape of a hyperstable RNA tetraloop. *Proc. Natl. Acad. Sci.* **113,** 6665–6670 (2016).

134. Cech, T. R. The Ribosome Is a Ribozyme. *Science* **289,** 878–879 (2000).

135. Fedor, M. J. & Williamson, J. R. The catalytic diversity of RNAs. *Nat. Rev. Mol. Cell Biol.* **6,** 399–412 (2005).

136. Kapoor, S. *et al.* Revealing conformational substates of lipidated N-Ras protein by pressure modulation. *Proc. Natl. Acad. Sci.* **109,** 460–465 (2012).

137. Silva, J. L. *et al.* High-Pressure Chemical Biology and Biotechnology. *Chem. Rev.* **114,** 7239–7267 (2014).

138. Eisenmenger, M. J. & Reyes-De-Corcuera, J. I. High pressure enhancement of enzymes: A review. *Enzyme Microb. Technol.* **45,** 331–347 (2009).

139. Akasaka, K., Nagahata, H., Maeno, A. & Sasaki, K. Pressure acceleration of proteolysis: A general mechanism. *Biophysics (Oxf).* **4,** 29–32 (2008).

140. Decaneto, E. *et al.* Pressure and Temperature Effects on the Activity and Structure of the Catalytic Domain of Human MT1-MMP. *Biophys. J.* **109,** 2371–2381 (2015).

141. Luong, T. Q., Kapoor, S. & Winter, R. Pressure-A Gateway to Fundamental Insights into Protein Solvation, Dynamics, and Function. *ChemPhysChem* **16,** 3555–3571 (2015).

142. Chinnusamy, V., Jagendorf, A. & Zhu, J.-K. Understanding and Improving Salt Tolerance in Plants. *Crop Sci.* **45,** 437–448 (2005).

143. Suladze, S., Cinar, S., Sperlich, B. & Winter, R. Pressure Modulation of the Enzymatic Activity of Phospholipase A2, A Putative Membrane-Associated Pressure Sensor. *J. Am. Chem. Soc.* **137,** 12588–12596 (2015).

144. Tobe, S. The catalytic mechanism of hairpin ribozyme studied by hydrostatic pressure. *Nucleic Acids Res.* **33,** 2557–2564 (2005).

145. Ztouti, M. *et al.* Adenine, a hairpin ribozyme cofactor - high-pressure and competition studies. *FEBS J.* **276,** 2574–2588 (2009).

146. Buzayan, J. M., Gerlach, W. L. & Bruening, G. Satellite tobacco ringspot virus RNA: A subset of the RNA sequence is sufficient for autolytic processing. *Proc. Natl. Acad. Sci.* **83,** 8859–8862 (1986).

147. Feldstein, P. A., Buzayan, J. M. & Bruening, G. Two sequences participating in the autolytic processing of satellite tobacco ringspot virus comple- mentary RNA. *Gene* **82,** 53–61 (1989).

148. Hampel, A. & Tritz, R. RNA catalytic properties of the minimum (-)sTRSV sequence. *Biochemistry* **28,** 4929–4933 (1989).

149. Symons, R. Plant pathogenic RNAs and RNA catalysis. *Nucleic Acids Res.* **25,** 2683–2689 (1997).

150. Meli, M. In Vitro Selection of Adenine-dependent Hairpin Ribozymes. *J. Biol. Chem.* **278,** 9835–9842 (2003).

151. Walter, N. G. Tertiary structure formation in the hairpin ribozyme monitored by fluorescence resonance energy transfer. *EMBO J.* **17,** 2378–2391 (1998).

152. Hegg, L. A. & Fedor, M. J. Kinetics and thermodynamics of intermolecular catalysis by hairpin ribozymes. *Biochemistry* **34,** 15813–15828 (1995).

153. Walter, N. G. & Burke, J. M. Real-time monitoring of hairpin ribozyme kinetics through base-specific quenching of fluorescein-labeled substrates. *RNA* **3,** 392–404 (1997).

154. DeYoung, M. B., Siwkowski, A. & Hampel, A. in *Ribozyme Protocols* (ed. Turner, P. C.) 209–220 (Humana Press, 1997).

155. Fedor, M. J. Tertiary Structure Stabilization Promotes Hairpin Ribozyme Ligation. *Biochemistry* **38,** 11040–11050 (1999).

156. Muth, G. W., Ortoleva-Donnelly, L. & Strobel, S. A. A single adenosine with a neutral pKa in the ribosomal peptidyl transferase center. *Science* **289,** 947–950 (2000).

157. Donahue, C. P., Yadava, R. S., Nesbitt, S. M. & Fedor, M. J. The kinetic mechanism of the hairpin ribozyme in vivo: influence of RNA helix stability on intracellular cleavage kinetics. *J. Mol. Biol.* **295,** 693–707 (2000).

158. Nissen, P., Hansen, J., Ban, N., Moore, P. B. & Steitz, T. A. The structural basis of ribosome activity in peptide bond synthesis. *Science* **289,** 920–930 (2000).

159. Zhuang, X. Correlating Structural Dynamics and Function in Single Ribozyme Molecules. *Science (80-.).* **296,** 1473–1476 (2002).

160. Bokinsky, G. *et al.* Single-molecule transition-state analysis of RNA folding. *Proc. Natl. Acad. Sci.* **100,** 9302–9307 (2003).

161. Millar, D. P., Walter, N. G. & Burke, J. M. No Title. *Nat. Struct. Biol.* **6,** 544–549 (1999).

162. Lilley, D. M. The ribosome functions as a ribozyme. *Chembiochem* **2,** 31–35 (2001).

163. Rupert, P. B., Ferré-D'Amaré, A. R. & Ferre-D'Amare, A. R. Crystal structure of a hairpin ribozyme-inhibitor complex with implications for catalysis. *Nature* **410,** 780–786 (2001).

164. Kuzmin, Y. I., Da Costa, C. P. & Fedor, M. J. Role of an Active Site Guanine in Hairpin Ribozyme Catalysis Probed by Exogenous Nucleobase Rescue. *J. Mol. Biol.* **340,** 233–251 (2004).

165. Kuzmin, Y. I., Da Costa, C. P., Cottrell, J. W. & Fedor, M. J. Role of an active site adenine in hairpin ribozyme catalysis. *J. Mol. Biol.* **349,** 989–1010 (2005).

166. Salter, J., Krucinska, J., Alam, S., Grum-Tokars, V. & Wedekind, J. E. Water in the Active Site of an All-RNA Hairpin Ribozyme and Effects of Gua8 Base Variants on the Geometry of Phosphoryl Transfer. *Biochemistry* **45,** 686–700 (2006).

167. Nam, K., Gao, J. & York, D. M. Quantum Mechanical/Molecular Mechanical Simulation Study of the Mechanism of Hairpin Ribozyme Catalysis. *J. Am. Chem. Soc.* **130,** 4680–4691 (2008).

168. Liu, L., Cottrell, J. W., Scott, L. G. & Fedor, M. J. Direct measurement of the ionization state of an essential guanine in the hairpin ribozyme. *Nat. Chem. Biol.* **5,** 351–357 (2009).

169. Guo, M. *et al.* Direct Raman Measurement of an Elevated Base p K a in the Active Site of a Small Ribozyme in a Precatalytic Conformation. *J. Am. Chem. Soc.* **131,** 12908–12909 (2009).

170. Mlýnský, V. *et al.* Extensive Molecular Dynamics Simulations Showing That Canonical G8 and Protonated A38H + Forms Are Most Consistent with Crystal Structures of Hairpin Ribozyme. *J. Phys. Chem. B* **114,** 6642–6652 (2010).

171. De Farias, S. T., Rêgo, T. G. & José, M. V. tRNA Core Hypothesis for the Transition from the RNA World to the Ribonucleoprotein World. *Life* **6,** 15 (2016).

172. Shi, H. & Moore, P. B. The crystal structure of yeast phenylalanine tRNA at 1.93 A resolution: a classic structure revisited. *RNA* **6,** 1091–1105 (2000).

173. Takamoto, K. *et al.* Principles of RNA Compaction: Insights from the Equilibrium Folding Pathway of the P4-P6 RNA Domain in Monovalent Cations. *J. Mol. Biol.* **343,** 1195–1206 (2004).

174. Bloomfield, V. A., Crothers, D. M. & Tinoco, I. *Nucleic Acids: Structures, Properties, and Functions*. (University Science Books, 2000).

175. Turner, D. H. Fundamental interactions in RNA: Questions answered and remaining. *Biopolymers* **99,** 1097–104 (2013).

176. Schuabb, C., Berghaus, M., Rosin, C. & Winter, R. Exploring the free energy and conformational landscape of tRNA at high temperature and pressure. *ChemPhysChem* **16,** 138–146 (2015).

177. Balny, C., Masson, P. & Heremans, K. High pressure effects on biological macromolecules: from structural changes to alteration of cellular processes. *Biochim. Biophys. Acta - Protein Struct. Mol. Enzymol.* **1595,** 3–10 (2002).

178. Winter, R. *Advances in High Pressure Bioscience and Biotechnology II*. (Springer-Verlag, 2003).

179. Winter, R. in *Chemistry at Extreme Conditions* 29–82 (Elsevier, 2005).

180. Ravindra, R. & Winter, R. On the Temperature-Pressure Free-Energy Landscape of Proteins. *ChemPhysChem* **4,** 359–365 (2003).

181. Almine, J. F. *et al.* Elastin-based materials. *Chem. Soc. Rev.* **39,** 3371–3379 (2010).

182. Vrhovski, B. & Weiss, A. S. Biochemistry of tropoelastin. *European Journal of Biochemistry* **258,** 1–18 (1998).

183. Hoeve, C. A. J. & Flory, P. J. The elastic properties of elastin. *Biopolymers* **13,** 677–686 (1974).

184. Debelle, L. & Tamburro, A. M. Elastin: molecular description and function. *Int. J. Biochem. Cell Biol.* **31,** 261–272 (1999).

185. Urry, D. W. Molecular Machines: How Motion and Other Functions of Living Organisms Can Result from Reversible Chemical Changes. *Angew. Chemie Int. Ed.* **32,** 819–841 (1993).

186. Wasserman, Z. R. & Salemme, F. R. A molecular dynamics investigation of the elastomeric restoring force in elastin. *Biopolymers* **29,** 1613–1631 (1990).

187. Debelle, L. & Alix, A. J. The structures of elastins and their function. *Biochimie* **81,** 981–994 (1999).

188. Li, B., Alonso, D. O. & Daggett, V. The molecular basis for the inverse temperature transition of elastin. *J. Mol. Biol.* **305,** 581–592 (2001).

189. Urry, D. W. & Long, M. M. Conformations of the repeat peptides of elastin in solution: an application of proton and carbon-13 magnetic resonance to the determination of polypeptide secondary structure. *CRC Crit. Rev. Biochem.* **4,** 1–45 (1976).

190. Vogtt, K. NMR-spektroskopische Untersuchungen des Einflusses von Cosolventien auf die Kältedenaturierung von Lysozym sowie des inversen Temperaturübergangs des elastin-mimetischen Polypeptids GVG $(VPGVG)_3$. (Universität Dortmund, 2006).

191. Krukau, A., Brovchenko, I. & Geiger, A. Temperature-Induced Conformational Transition of a Model Elastin-like Peptide $GVG(VPGVG)_3$ in Water. *Biomacromolecules* **8,** 2196–2202 (2007).

192. Reiersen, H. & Rees, A. R. Trifluoroethanol may form a solvent matrix for assisted hydrophobic interactions between peptide side chains. *Protein Eng. Des. Sel.* **13,** 739–743 (2000).

193. Urry, D. W. & Ohnishi, T. Studies on the conformations and interactions of elastin. Proton magnetic resonance of the repeating tetramer. *Biopolymers* **13,** 1223–1242 (1974).

194. Matilla, A. & Radrizzani, M. The Anp32 family of proteins containing leucine-rich repeats. *The Cerebellum* **4,** 7–18 (2005).

195. Bai, J., Brody, J. R., Kadkol, S. S. & Pasternack, G. R. Tumor suppression and potentiation by manipulation of pp32 expression. *Oncogene* **20,** 2153–2160 (2001).

196. Kajava, A. V. Structural diversity of leucine-rich repeat proteins. *J. Mol. Biol.* **277,** 519–527 (1998).

197. Kloss, E., Courtemanche, N. & Barrick, D. Repeat-protein folding: New insights into origins of cooperativity, stability, and topology. *Arch. Biochem. Biophys.* **469,** 83–99 (2008).

198. Schrodinger LLC. The PyMOL Molecular Graphics System, Version 1.8. (2015).

199. Ho, B. K. & Gruswitz, F. HOLLOW: Generating Accurate Representations of Channel and Interior Surfaces in Molecular Structures. *BMC Struct. Biol.* **8,** 49 (2008).

200. Richardson, J. S. & Richardson, D. C. Natural β-sheet proteins use negative design to avoid edge-to-edge aggregation. *Proc. Natl. Acad. Sci.* **99,** 2754–2759 (2002).

201. Dao, T. P., Majumdar, A. & Barrick, D. Capping motifs stabilize the leucine-Rich repeat protein PP32 and rigidify adjacent repeats. *Protein Sci.* **23,** 801–811 (2014).

202. Sheterline, P., Clayton, J. & Sparrow, J. Actin. *Protein Profile* **2,** 1–103 (1995).

203. Xian, W., Tang, J. X., Janmey, P. A. & Braunlin, W. H. The Polyelectrolyte Behavior of Actin Filaments:? A ^{25}Mg NMR Study ? *Biochemistry* **38,** 7219–7226 (1999).

204. Jacob N. Israelachvili. *Intermolecular and Surface Forces*. (Elsevier, 2011).

205. Kureishy, N., Sapountzi, V., Prag, S., Anilkumar, N. & Adams, J. C. Fascins, and their roles in cell structure and function. *BioEssays* **24,** 350–361 (2002).

206. Jansen, S. *et al.* Mechanism of Actin Filament Bundling by Fascin. *J. Biol. Chem.* **286,** 30087–30096 (2011).

207. Yang, S. *et al.* Molecular Mechanism of Fascin Function in Filopodial Formation. *J. Biol. Chem.* **288,** 274–284 (2013).

208. Claessens, M. M. a E., Semmrich, C., Ramos, L. & Bausch, a R. Helical twist controls the thickness of F-actin bundles. *Proc. Natl. Acad. Sci.* **105,** 8819–8822 (2008).

209. Bornschlögl, T. How filopodia pull: What we know about the mechanics and dynamics of filopodia. *Cytoskeleton* **70,** 590–603 (2013).

210. Mattila, P. K. & Lappalainen, P. Filopodia: molecular architecture and cellular functions. *Nat. Rev. Mol. Cell Biol.* **9,** 446–454 (2008).

211. Stevenson, R. P., Veltman, D. & Machesky, L. M. Actin-bundling proteins in cancer progression at a glance. *J. Cell Sci.* **125,** 1073–1079 (2012).

212. Shin, H., Drew, K. R. P., Bartles, J. R., Wong, G. C. L. & Grason, G. M. Cooperativity and Frustration in Protein-Mediated Parallel Actin Bundles. *Phys. Rev. Lett.* **103,** 238102 (2009).

213. Gao, M., Berghaus, M., von der Ecken, J., Raunser, S. & Winter, R. Condensation agents determine the temperature-pressure stability of F-actin bundles. *Angew. Chemie Int. Ed.* **54,** 11088–11092 (2015).

214. Zhu, T. F., Budin, I. & Szostak, J. W. in *Methods in enzymology, Vol. 533,* 275–282 (2013).

215. Sztucki, M. & Narayanan, T. Development of an ultra-small-angle X-ray scattering instrument for probing the microstructure and the dynamics of soft matter. *J. Appl. Crystallogr.* **40,** s459–s462 (2006).

216. Petoukhov, M. V *et al.* New developments in the ATSAS program package for small-angle scattering data analysis. *J. Appl. Crystallogr.* **45,** 342–350 (2012).

217. Good, N. E. *et al.* Hydrogen Ion Buffers for Biological Research. *Biochemistry* **5,** 467–477 (1966).

218. Winter, R. *et al.* Inverse bicontinuous cubic phases in fatty acid/phosphatidylcholine mixtures: the effects of pressure and lipid composition. *Phys. Chem. Chem. Phys.* **1,** 887–893 (1999).

219. Squires, A. M. *et al.* Kinetics and mechanism of the interconversion of inverse bicontinuous cubic mesophases. *Phys. Rev. E* **72,** 11502 (2005).

220. S. A. Safran. *Statistical Thermodynamics Of Surfaces, Interfaces, And Membranes*. (Addison-Wesley, 1994).

221. Helfrich, W. Effect of thermal undulations on the rigidity of fluid membranes and interfaces. *J. Phys.* **46,** 1263–1268 (1985).

222. Kern, W, Puotinen, D. Cleaning Solution Based on Hydrogen Peroxide for use in semiconductor technology. *RCA Rev.* **31,** 187–207 (1970).

223. Breßler, I., Kohlbrecher, J. & Thünemann, A. F. SASfit : a tool for small-angle scattering data analysis using a library of analytical expressions. *J. Appl. Crystallogr.* **48,** 1587–1598 (2015).

224. Lee, D. D., Chen, S. H., Majkrzak, C. F. & Satija, S. K. Bulk and surface correlations in a microemulsion. *Phys. Rev. E* **52,** R29–R32 (1995).

225. Kell, G. S. Density, thermal expansivity, and compressibility of liquid water from 0°C to 150°C: Correlations and tables for atmospheric pressure and saturation reviewed and expressed on 1968 temperature scale. *J. Chem. Eng. Data* **20,** 97–105 (1975).

226. Díaz Peña, M. & Tardajos, G. Isothermal compressibilities of n-alkanes and benzene. *J. Chem. Thermodyn.* **10,** 19–24 (1978).

227. Ludwig, R. Water: From clusters to the bulk. *Angewandte Chemie - International Edition* **40,** 1808–1827 (2001).

228. Chen, S. H., Chang, S. L. & Strey, R. Simulation of bicontinuous microemulsions: comparison of simulated real-space microstructures with scattering experiments. *J. Appl. Crystallogr.* **24,** 721–731 (1991).

229. Seto, H., Nagao, M. & Kawabata, Y. Pressure-dependence of the bending modulus of surfactant monolayers in ternary microemulsion systems observed by neutron spin echo. *Colloids Surfaces A Physicochem. Eng. Asp.* **284–285,** 430–433 (2006).

230. Gao, M. *et al.* Self-assembly of guanosine monophosphate – a potential prebiotic precursor of today's nucleic acids? *Submitted* (2017).

231. Jurga-nowak, H., Banachowicz, E., Dobek, A. & Patkowski, A. Supramolecular Guanosine 5' -Monophosphate Structures in Solution. Light Scattering Study Study. *J. Phys. Chem. B* **108,** 2744–2750 (2004).

232. Benhamou, M., El Kinani, R. & Kaidi, H. Rigorous Study of the Unbinding Transition of Biomembranes and Strings from Morse Potentials. *Conf. Pap. Math.* **2013,** 1–7 (2013).

233. Benhamou, M. & Kaidi, H. Unbinding transition from fluid membranes with associated polymers. *Eur. Phys. J. E* **36,** 125 (2013).

234. Lipowsky, R., Leibler, S., Lipowsky & Leibler. Unbinding transitions of interacting membranes. *Phys. Rev. Lett.* **56,** 2541–2544 (1986).

235. Ellis, R. J. Macromolecular crowding: obvious but underappreciated. *Trends Biochem. Sci.* **26,** 597–604 (2001).

236. Schuabb, C., Pataraia, S., Berghaus, M. & Winter, R. Exploring the effects of temperature and pressure on the structure and stability of a small RNA hairpin. *Biophys. Chem.* (2016). Advance online publication, doi:10.1016/j.bpc.2016.10.006

237. Schuabb, C., Kumar, N., Pataraia, S., Marx, D. & Winter, R. Pressure modulates the self-cleavage step of the hairpin ribozyme. *Nat. Commun.* **8,** 14661 (2017).

238. Patkowski, a., Gulari, E. & Chu, B. Long range tRNA?tRNA electrostatic interactions in salt?free and low?salt tRNA solutions. *J. Chem. Phys.* **73,** 4178–4184 (1980).

239. Thirumalai, D. & Hyeon, C. *Non-Protein Coding RNAs*. **13,** (Springer-Verlag, 2009).

240. Giel-Pietraszuk, M. & Barciszewski, J. A nature of conformational changes of yeast tRNA(Phe). High hydrostatic pressure effects. *Int. J. Biol. Macromol.* **37,** 109–114 (2005).

241. Pilz, I. *et al.* On the Conformation of Phenylalanine Specific Transfer RNA Studies on Size and Shape of the Molecule by X-Ray Small Angle Scattering. *Eur. J. Biochem.* **15,** 401–409 (1970).

242. Fang, X. *et al.* Mg 2+ -Dependent Compaction and Folding of Yeast tRNA Phe and the Catalytic Domain of the B. subtilis RNase P RNA Determined by Small-Angle X-ray Scattering ? *Biochemistry* **39,** 11107–11113 (2000).

243. Panick, G. *et al.* Structural characterization of the pressure-denatured state and unfolding/refolding kinetics of staphylococcal nuclease by synchrotron small-angle X-ray scattering and Fourier-transform infrared spectroscopy. *J. Mol. Biol.* **275,** 389–402 (1998).

244. Serebrov, V. Mg2+ binding and structural stability of mature and in vitro synthesized unmodified Escherichia coli tRNAPhe. *Nucleic Acids Res.* **26,** 2723–2728 (1998).

245. Macgregor, R. Effect of hydrostatic pressure on nucleic acids. *Biopolymers* **48,** 253–262 (1998).

246. Tintar, D. *et al.* Human tropoelastin sequence: Dynamics of polypeptide coded by exon 6 in solution. *Biopolymers* **91,** 943–952 (2009).

247. Reiersen, H., Clarke, A. R. & Rees, A. R. Short elastin-like peptides exhibit the same temperature-induced structural transitions as elastin polymers: implications for protein engineering. *J. Mol. Biol.* **283,** 255–264 (1998).

248. Matt, A., Kuttich, B. & Stühn, B. Talk: Dynamik von Polymer/Wasser Mischungen im weichen Confinement. *Treffen der DFG-Forschergruppe 1583 - Confine Dynamics* (Rückersbach, 2017).

249. Svergun, D. I. Determination of the regularization parameter in indirect-transform methods using perceptual criteria. *J. Appl. Crystallogr.* **25,** 495–503 (1992).

250. Kahse, M. Struktur und Stabilität von Biomolekülen in räumlich einschränkenden Geometrien. (TU-Dortmund, 2016).

251. Zhang, Y. *et al.* Capping and Cooperativity in a Leucine Rich Repeat Protein. *In preparation* (2017).

252. Krywka, C. Ein Aufbau für Röntgenkleinwinkelstreuung an Protein-Lösungen an der Synchrotronstrahlungsquelle DELTA. (TU-Dortmund, 2008).

253. Rosin, C., Erlkamp, M., Ecken, J. von der, Raunser, S. & Winter, R. Exploring the Stability Limits of Actin and Its Suprastructures. *Biophys. J.* **107,** 2982–2992 (2014).

254. Angelini, T. E., Liang, H., Wriggers, W. & Wong, G. C. L. Direct observation of counterion organization in F-actin polyelectrolyte bundles. *Eur. Phys. J. E* **16,** 389–400 (2005).

255. Kierfeld, J., Kühne, T. & Lipowsky, R. Discontinuous Unbinding Transitions of Filament Bundles. *Phys. Rev. Lett.* **95,** 38102 (2005).

256. Kierfeld, J. & Lipowsky, R. Duality mapping and unbinding transitions of semiflexible and directed polymers. *J. Phys. A. Math. Gen.* **38,** L155–L161 (2005).

257. Sedeh, R. S. *et al.* Structure, Evolutionary Conservation, and Conformational Dynamics of Homo sapiens Fascin-1, an F-actin Crosslinking Protein. *J. Mol. Biol.* **400,** 589–604 (2010).

258. Gunning, P. W., Ghoshdastider, U., Whitaker, S., Popp, D. & Robinson, R. C. The evolution of compositionally and functionally distinct actin filaments. *J. Cell Sci.* **128,** 2009–2019 (2015).

Curriculum Vitae

Personal Information

Name	Melanie Berghaus
Date of Birth	11th of April 987
Place of Birth	Dortmund, Germany

Education

2013-present	**PhD Programm in Chemistry, TU-Dortmund University** PhD thesis: „Structural Investigations of Biomolecules under Extreme Conditions“
2008-2012	**Studies in Chemical Biology, TU-Dortmund University**
10/2012	Master of Science (M.Sc.) Master thesis: „Synthesis and Selection of Imprinted Nanoparticles Using Multifunctional Templates“
09/2010	Bachelor of Science (B.Sc.) Bachelor thesis : „Das Reaktionsverhalten von (2,2‘-bpy)-$PtCl_2$ mit der Modell-Nukleobase 1-Methylcytosin“
10/2011-01/2012	**Research Internship (Erasmus), National University of Ireland, Galway** Topic: „Antitumour Active Pt(IV) Complexes with Receptor-Specific Carrier Ligands“
2006-2008	**Studies in Bioengineering at TU-Dortmund University**
06/2006	**Graduation from secondary school** Helene-Lange-Gymnasium, Dortmund

Professional Experience

01/2017-present	**Research Associate at the Federal Institute for Occupational Safety and Health (BAuA)**
11/2012-12/2016	**Research Associate at TU-Dortmund University**

Publications

Scientific Papers

1. Gao, M., Harish, B., Berghaus, M., Seymen, R., Arns, L., Royer, C. A., Winter, R. Self-assembly of guanosine monophosphate – a potential prebiotic precursor of today's nucleic acids?. *Submitted* (2017).

2. Zhang, Y., Berghaus, M., Klein, S., Morgan, J., Winter, R., Barrick,D., Royer, C.A. Capping and Cooperativity in a Leucine Rich Repeat Protein. *In preparation* (2017).

3. Schuabb, C., Pataraia, S., Berghaus, M., and Winter, R. Exploring the effects of temperature and pressure on the structure and stability of a small RNA hairpin. *Biophys. Chem.,* Advance online publication, DOI: 10.1016/j.bpc.2016.10.006 (2016).

4. Berghaus, M., Paulus, M., Salmen, P., Al-Ayoubi, S., Tolan, M., and Winter, R. Near-Surface and Bulk Behavior of Bicontinuous Microemulsions under High-Pressure Conditions. *J. Phys. Chem. B* **120**, 7148–7153 (2016).

5. Yin-Bandur, L., Sanz Miguel, P. J., Rodríguez-Santiago, L., Sodupe, M., Berghaus, M., and Lippert, B. Multiple Condensation Reactions Involving Pt II / Pd II−OH_2, Pt−NH_3, and Cytosine−NH_2 Groups: New Twists in Cisplatin−Nucleobase Chemistry. *Chem. - A Eur. J.* **22**, 13653–13668 (2016).

6. Gao, M., Berghaus, M., von der Ecken, J., Raunser, S., Winter, R., Von der Ecken, J., Raunser, S., and Winter, R. Condensation Agents Determine the Temperature-Pressure Stability of F-actin Bundles. *Angew. Chem. Int. Ed.* **54**, 11088–11092 (2015).

7. Schuabb, C., Berghaus, M., Rosin, C., and Winter, R. Exploring the free energy and conformational landscape of tRNA at high temperature and pressure. *ChemPhysChem* **16**, 138–146 (2015).

8. Kapoor, S., Berghaus, M., Suladze, S., Prumbaum, D., Grobelny, S., Degen, P., Raunser, S., and Winter, R. Prebiotic Cell Membranes that Survive Extreme Environmental Pressure Conditions. *Angew. Chemie Int. Ed.* **53**, 8397–8401 (2014).

9. Berghaus, M., Mohammadi, R., and Sellergren, B. Productive encounter: molecularly imprinted nanoparticles prepared using magnetic templates. *Chem. Commun.* **50**, 8993-8996 (2014).

Posters

1. Berghaus, M., Gao, M., Seymen, R., and Winter, R. Effect of temperature, pressure, and cosolutes on the self-assembly of guanosine monophosphate, 9th International Conference on High Pressure Bioscience and Biotechnology, Toronto, Canada (2016).

2. Berghaus, M., Paulus, M.,Salmen, P. Al-Ayoubi, S., Tolan, M., and Winter, R. Near-surface behavior of a bicontinuous microemulsion under high hydrostatic pressure conditions, 8th International Meeting on Biomolecules under Pressure (IMBP), Dortmund, Germany (2016).

3. Berghaus, M., Gao, M., and Winter, R. Packing efficiency controls the temperature-pressure stability of F-actin bundles, 114 th General Assembly of the German Bunsen Society for Physical Chemistry, Bochum, Germany (2015).

4. Kapoor, S., Berghaus, M., Suladze, S, Prumbaum, D., Grobelny, S., Degen, P., Raunser, S. , and Winter, R. Growing up: High temperature and pressure foster micelle-to-vesicle transition in prebiotic amphiphilic mixtures, 113th General Assembly of the German Bunsen Society for Physical Chemistry, Hamburg, Germany (2014).

5. Mohammadi R., Nematollahzadeh A., Wei S, Halhalli, M.R., Lindemann, P., Tenboll A., Chandrasekaran D., Wang Z., Berghaus M., Schillinger E., and Sellergren, B. MIPs for antibody capture, 7th International conference on Molecularly Imprinted Polymers-Science and technology, Paris, France (2012).

Talks

1. Berghaus, M., Paulus, M., Salmen, P., Al-Ayoubi, S., Tolan, M., and Winter, R. Near-Surface and Bulk Behavior of Bicontinuous Microemulsions under High-Pressure Conditions. 11th DELTA user Meeting, Dortmund, Germany (2016).

Acknowledgements

At the end of my thesis, I would like to thank all the people who contributed to this work. Firstly, I would like to express my sincere gratitude to my advisor Prof. Dr. Roland Winter for giving me the opportunity to work on various interesting topics, many fruitful discussions and for his constant support during my doctorate. In addition, I thank Prof. Dr. Rehage for his work as second examiner of this thesis.

Further, I want to thank Prof. Dr. Claus Czeslik for lots of help and advice regarding the X-ray instruments. I would have been lost without the help of Andrea Kreusel, who always knew how to fix administrative issues. Thanks to her, I could order whatever I needed, my proteins got out of the customs in time and my samples and equipment arrived smoothly at the beamlines. I also want to thank Simone Möbitz for introducing me into protein expression and purification. I highly appreciate that you shared your knowledge and experience with me and it was a pleasure to work with you in the S1 lab. Whenever I needed access to not easily available literature or needed help in drawing images, I could always rely on Bertina “Berti” Schuppan. Thank you for your help and encouragement!

Of cause I also want to thank all my fellow PhD students and PostDocs, who made working in the lab a nice and unforgettable experience. First of all, I would like to thank Dr. Marie Kahse and Loana Arns for their friendship, their support, and lots of helpful advice. Also the help and enjoyable collaboration with Mimi Gao and Nelli Erwin is highly appreciated. I will never forget our trip to Toronto! Dr. Janine Seeliger and Dr. Shobhna Kapoor I want to thank for their advice and enjoyable times inside and outside the lab. Though we only met for a short time before I left, it was a special pleasure for me to work with Dr. Irena Kiesel. I want to thank Dr. Caroline Schuabb and Dr. Salome Pataraia for the good collaboration on the RNA projects. I also want to thank Samy Al-Ayoubi for his constant support on many beamtimes. Dr. Vitor Schuabb is especially acknowledged for his help to move the high pressure equipment to the new chemistry building and getting it more organized. I am grateful to Dr. Mirko Erlkamp and Dr. Sebastian Grobelny and Dr. Katrin Weise for helping me to get started with SAXS. It was also a pleasure for me to work with my two bachelor students, Lukas Eberlein and Shari Meichsner.

All the other people, in no particular order, I thank for a nice and enjoyable working atmosphere: Dr. Mridula Dwivedi, Dr. Trung Quan Luong, Dr. Satyajit Patra, Süleyman Cinar, Sudeshna Banerjee, Christian Anders, Paul Hendrik Schummel, Steffen Bornemann, Artem Levin, Lei Li., Dr. Saba Suladze, Dr. Benjamin Sperlich, and Dr. Christopher Rosin. Furthermore, I want to thank Britta Aurich for her help in the practical course.

This work would not have been possible with lots of help from many different people on the beamtimes. Though there are too many to name all of them individually here, I want to express my special gratitude to some of them. First of all, I want to thank Dr. Johannes Möller, who made working at ID02 of the ESRF a good experience. His support, his patience and lots of helpful discussions, which significantly contributed to the success of my experiments, are invaluable. Also Javier Perez from the SWING beamline at the SOLEIL is kindly acknowledged. Thanks to all the staff at the X-ray sources who keep them running and enable us to do experiments there!

Many experiments were performed in collaboration with the Tolan-group from the physics department of TU-Dortmund. I want to thank especially Julian Schulze and Karin Julius for the enjoyable atmosphere at the beamtimes. Further, I want to thank Michael Paulus and Paul Salmen for their help on the project with the microemulsion at the DELTA in Dortmund. Last but not least, I want to thank again all of the people from the Winter-group who helped on the beamtimes!

This work would not have been possible without funding. I thank the ESRF, the SOLEIL and the DELTA for providing beamtime, accommodation and reimbursement of the traveling costs. Furthermore, I would like to acknowledge the DFG Forschergruppe 1583 for funding. In addition, I want to thank all members of this group for good collaboration on projects and for many enjoyable meetings and workshops.

Finally, I want to express my immense gratitude to my family. Without your constant support, your patience and understanding and your love I would never have succeeded in my studies!

Appendix

Additional figures

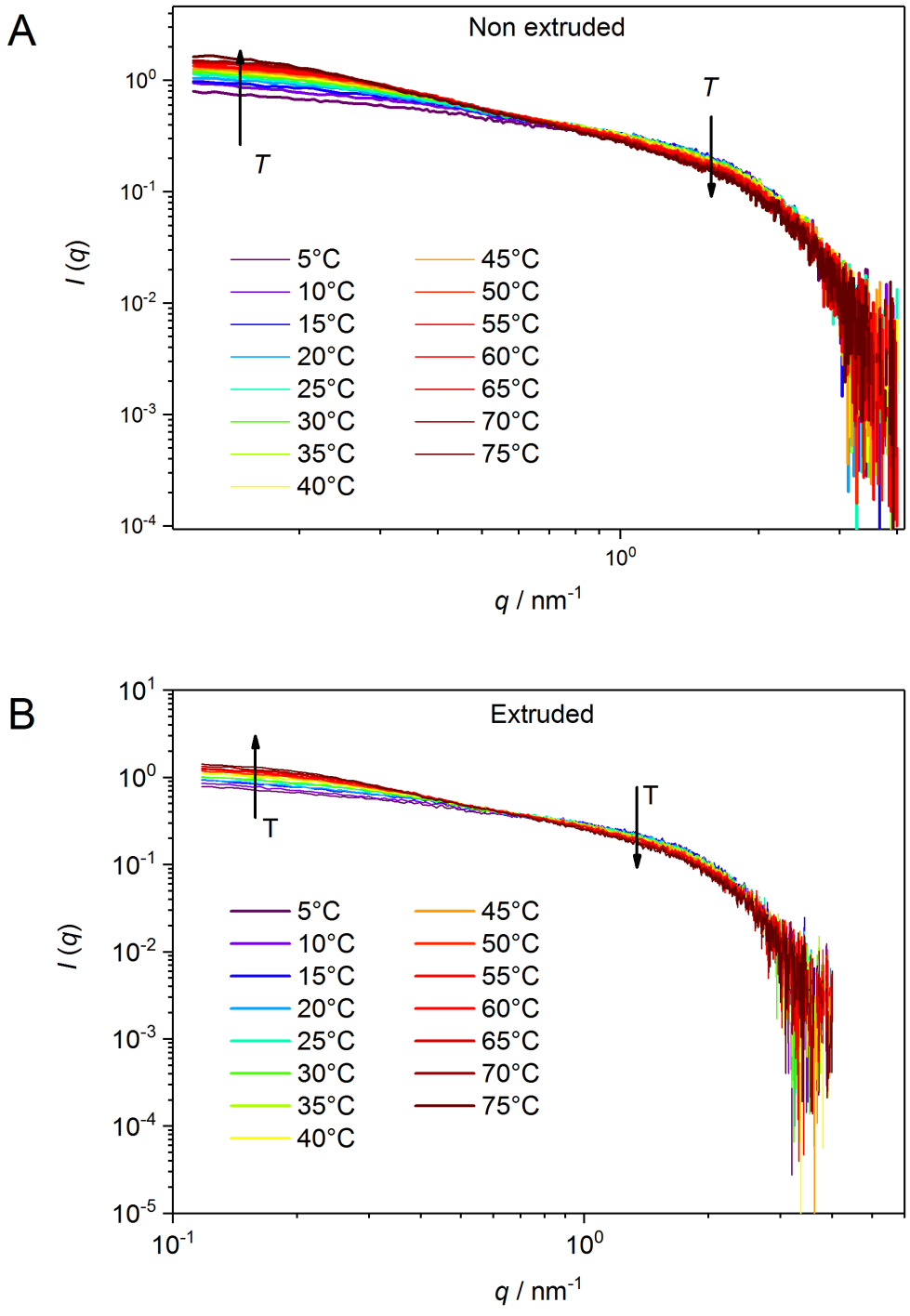

Figure A1. Effect of extrusion on the prebiotic lipid mixture comprising decanoic acid : decanol (2:1 molar ratio, pH 8.5).

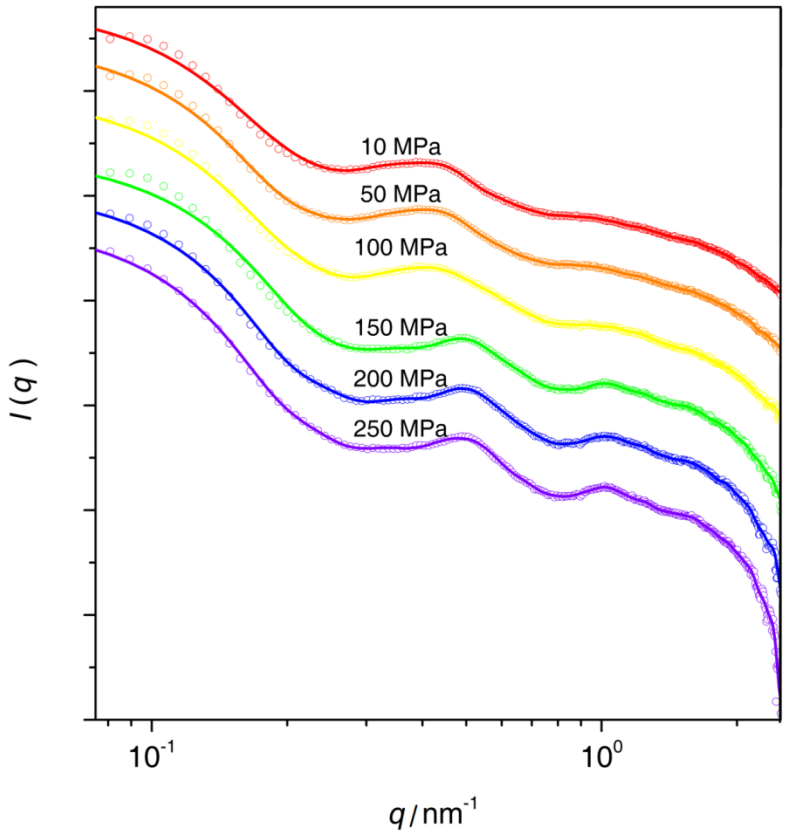

Figure A2. Structural characteristics of the prebiotic lipid mixture upon compression. Selected pressure dependent SAXS profiles (open circles) for the prebiotic lipid mixture comprising decanoic acid : decanol (2:1 molar ratio, pH 8.5) and corresponding fits for the calculation of the $P(r)$-functions (solid lines) at 25°C. The curves are vertically shifted for clarity.

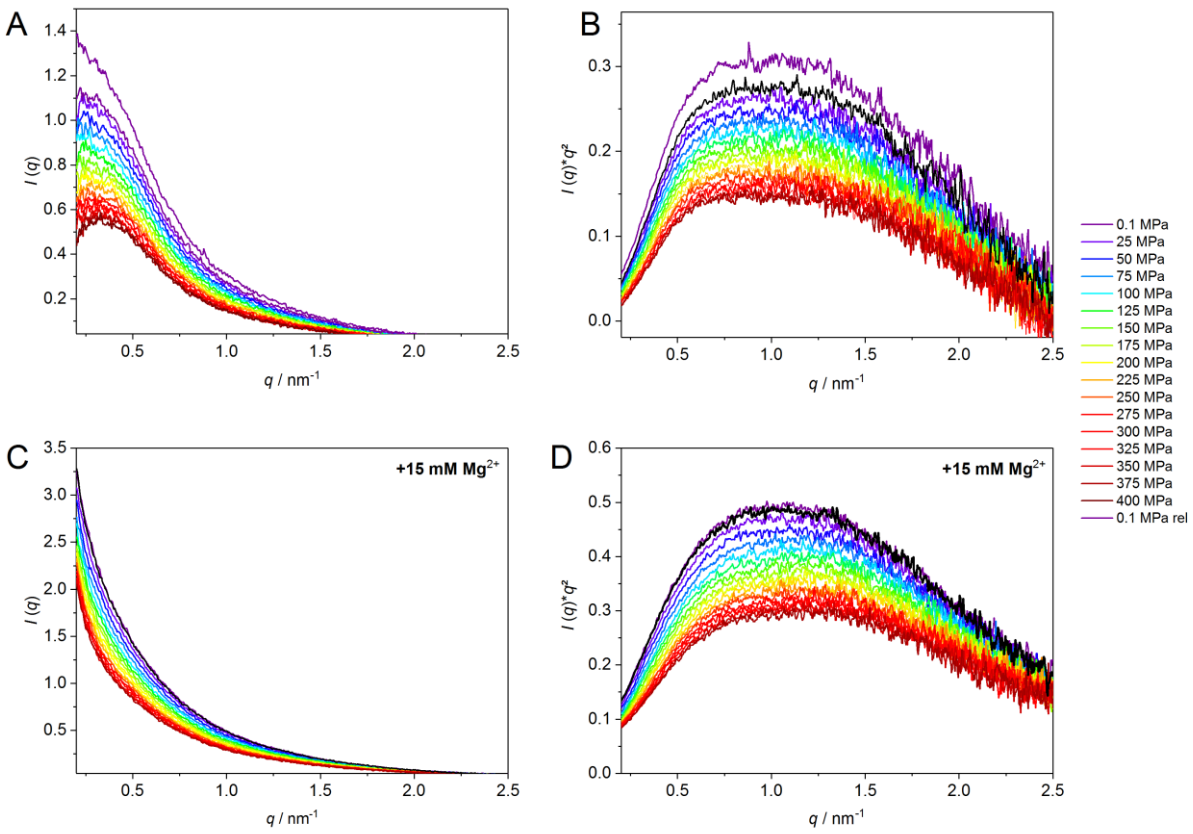

Figure A3. Scattering profiles of 10 mg/mL hairpin ribozyme at different pressures in the absence (A,B) and presence of 15 mM Mg^{2+} (C,D). Plots are represented in linear (A,C) and Kratky-plot representation (B,D). The correlation peak in (A) indicates repulsion between the RNA molecules at a concentration of 10 mg/mL. The high intensity at very low q-values in the presence of 15 mM Mg^{2+} (B) points towards aggregations of the ribozyme. The persistent bell-shape of the Kratky-plots indicates a compact form of the ribozyme at all conditions of pressure investigated.

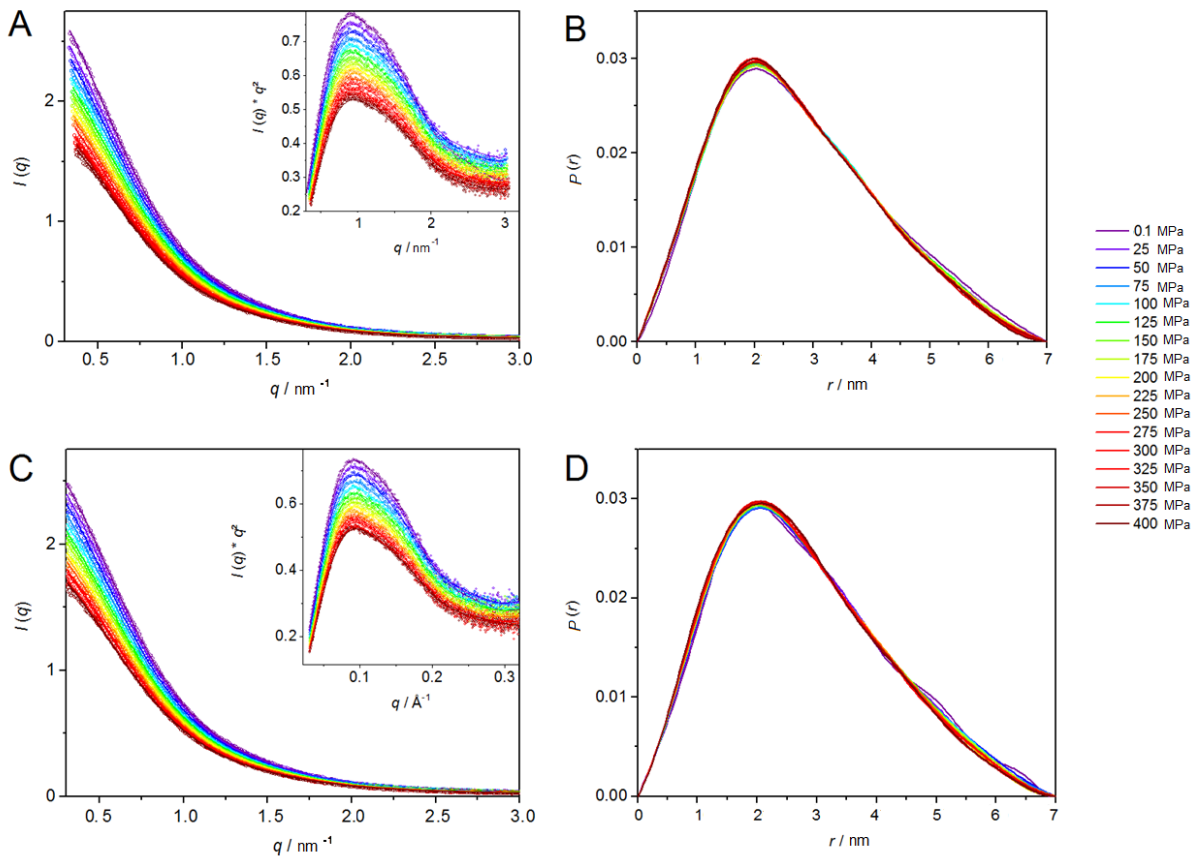

Figure A4. Pressure-dependent SAXS data of $tRNA^{Phe}$ at 40°C (3 wt% in 50 mM Tris-HCl buffer, pH 7.5, with 0.1 mM EDTA in the absence of $MgCl_2$ (A, B) and presence of 15 mM $MgCl_2$ (C, D) Intensity profiles at different pressures (A,C) with Kratky representation of the respective data (inserts). Solid lines represent fits obtained by using the indirect Fourier-transformation method to calculate the pair-distance distribution functions (B,C).

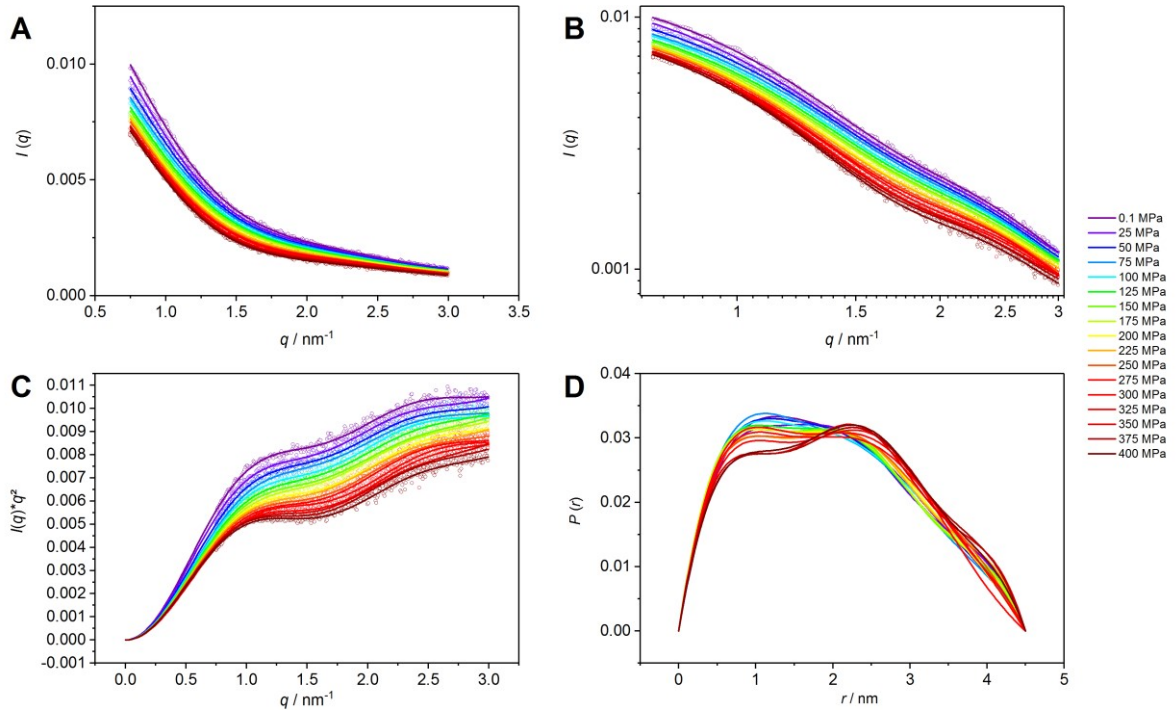

Figure A5. Scattering data of the sRNAh 20°C. Scattering data is represented as linear plot (A), double logarithmic plot (B) and Kratky-plot (C). Corresponding $P(r)$ functions are represented in (E). Pressures are color coded according to the legend.

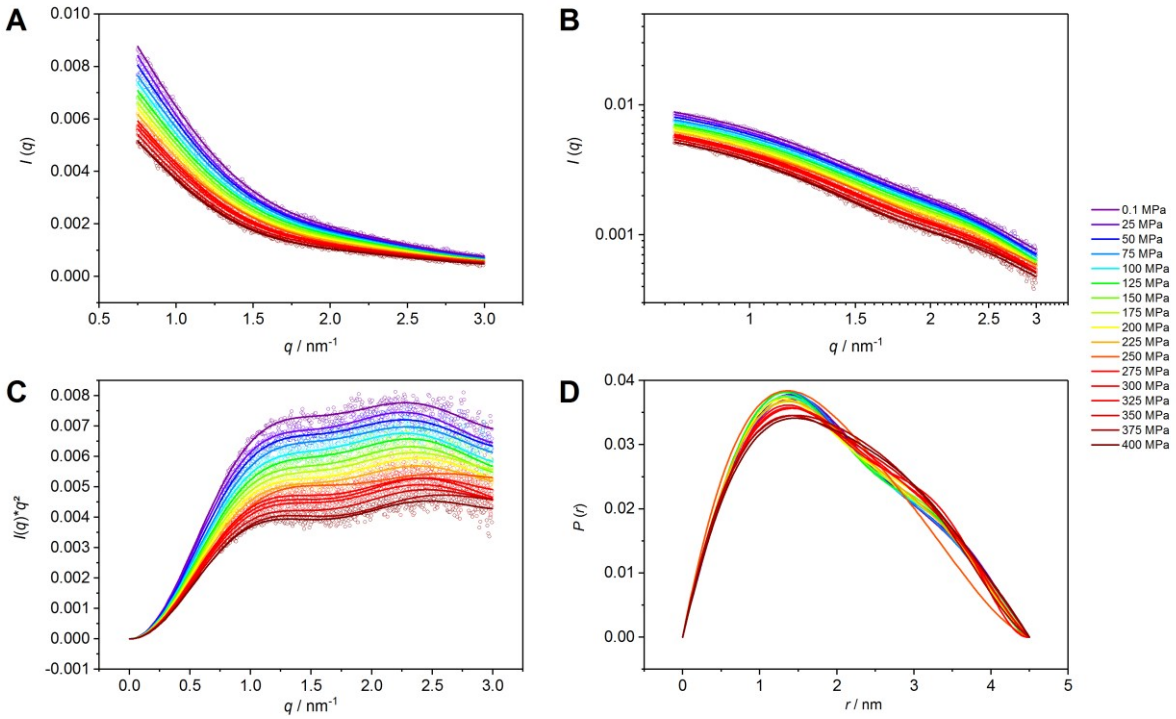

Figure A6. Scattering data of the sRNAh 40°C. Scattering data is represented as linear plot (A), double logarithmic plot (B) and Kratky-plot (C). Corresponding $P(r)$ functions are represented in (E). Pressures are color coded according to the legend.

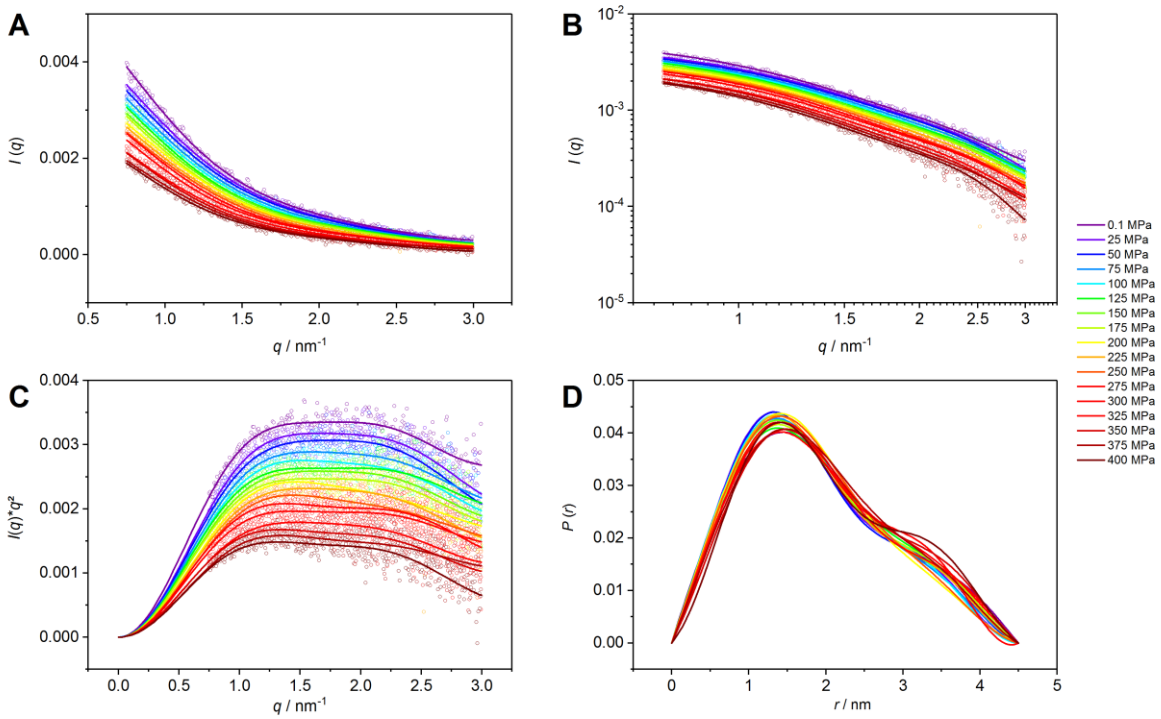

Figure A7. Scattering data of the sRNAh 60°C. Scattering data is represented as linear plot (A), double logarithmic plot (B) and Kratky-plot (C). Corresponding $P(r)$ functions are represented in (E). Pressures are color coded according to the legend.

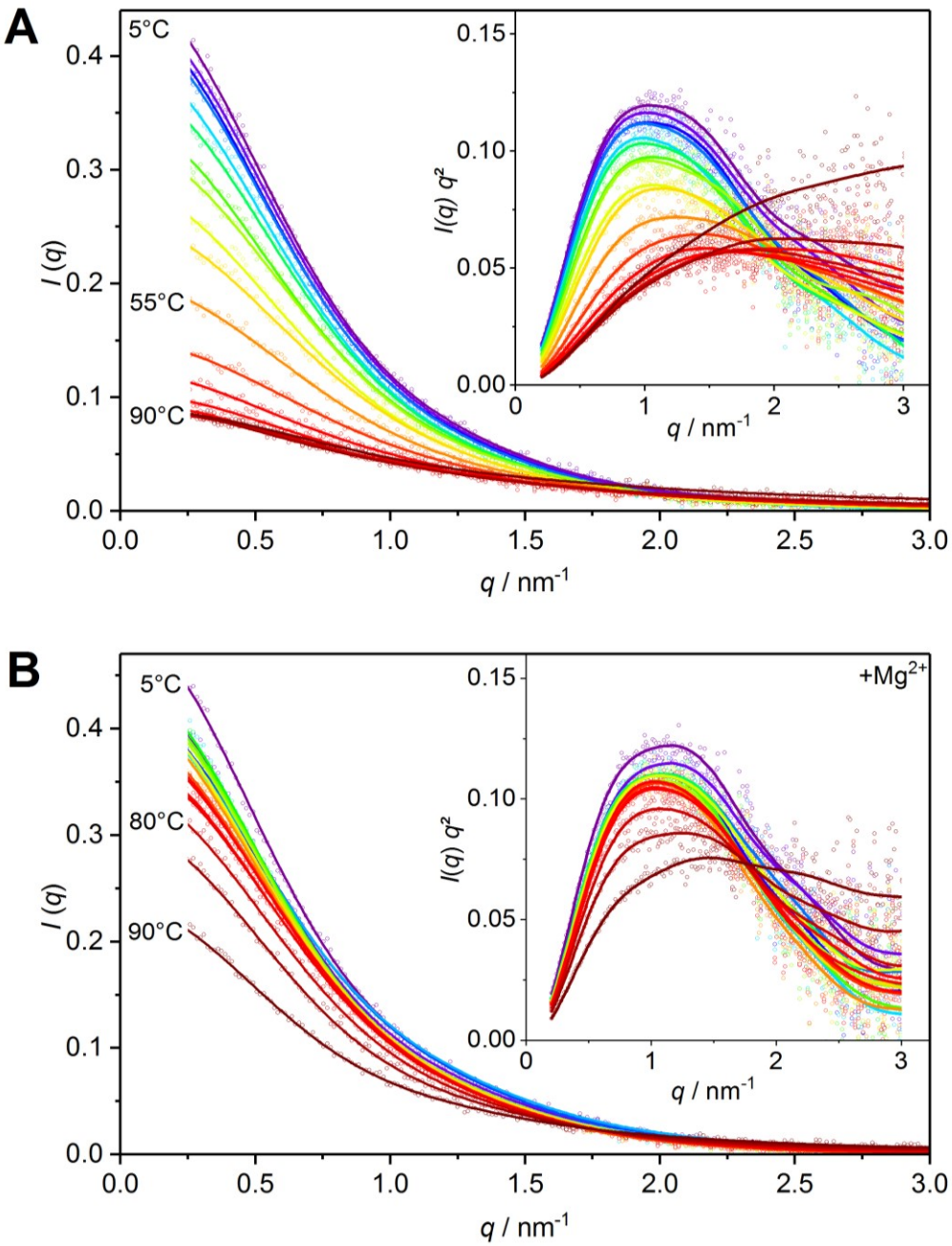

Figure A8. Temperature dependent SAXS analysis of $tRNA^{Phe}$ in Tris-HCl Buffer in the absence (A) and presence of Mg^{2+} (B). Intensity profiles were recorded in a temperature range starting from 5°C (purple) in steps of 5°C up to 90°C (dark red). Open circles represent the corrected original data, the solid lines represent fits obtained using the indirect Fourier transformation method. Concentrations were 0.5 wt% $tRNA^{Phe}$. Inserts: Kratky plots of the respective data.

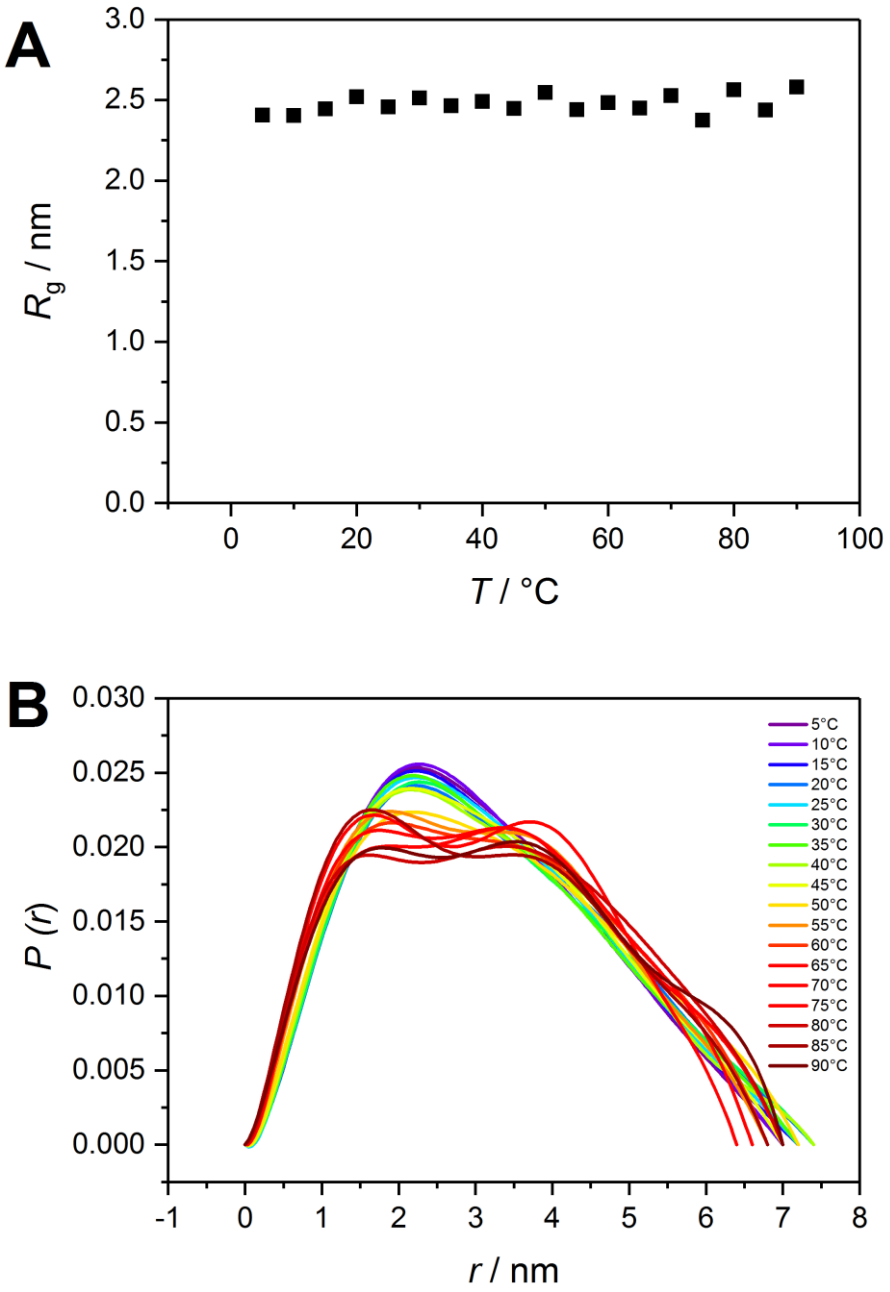

Figure A9. Temperature dependent radius of gyration (A) and $P(r)$ functions (B) of 0.5 wt% $tRNA^{Phe}$ in Tris-HCl Buffer in the absence of Mg^{2+}.

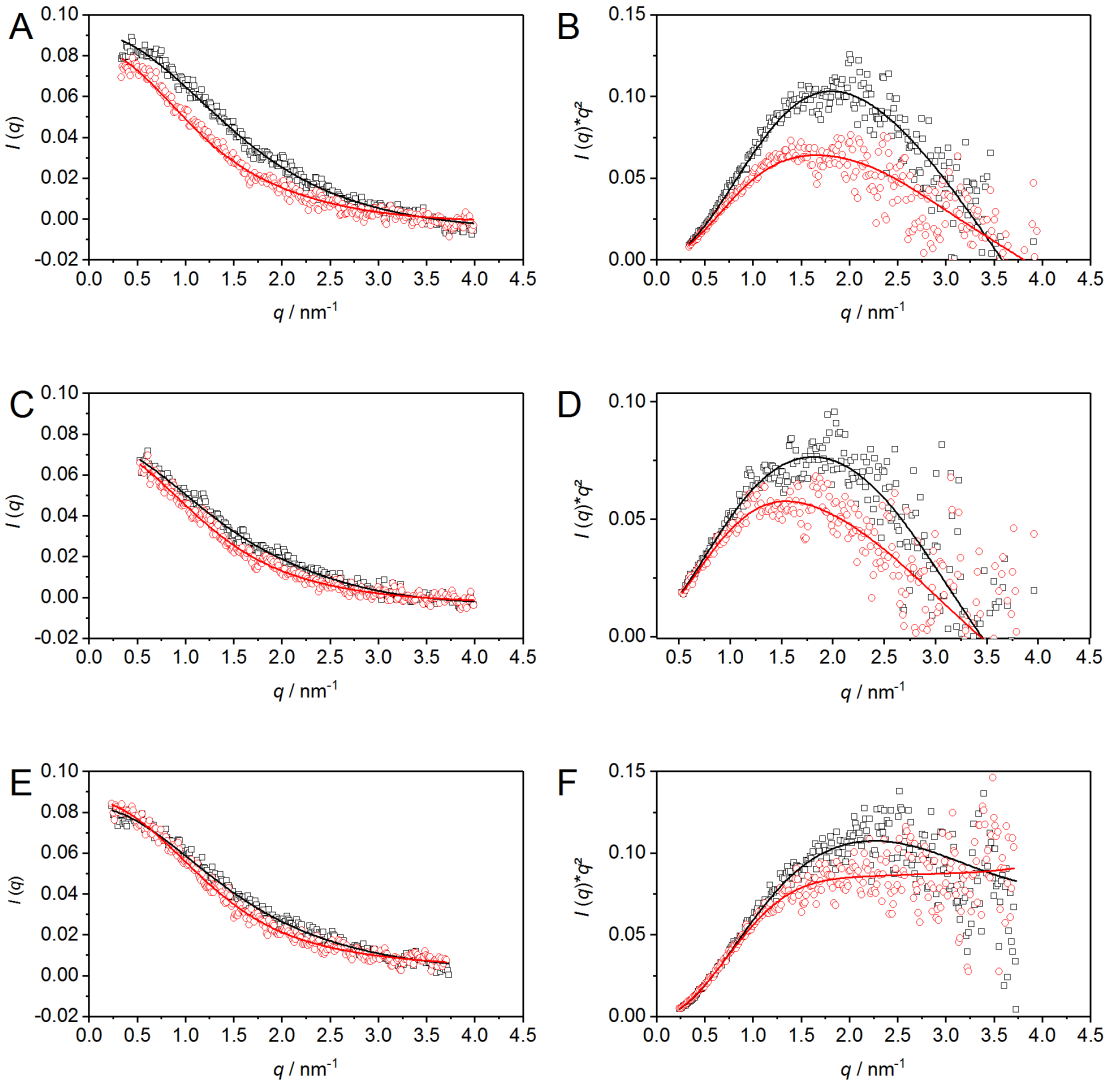

Figure A10. Scattering data of the ELP in 1 M TMAO (A,B), a mixture containing 1 M TMAO and 2 M urea (C,D) and 2 M urea (E,F). Scattering curves were recorded at 10°C (black open squares) and 80°C (red open circles) and are represented as linear scattering curves (A,C,E) and Kratky plots (B, D,F).

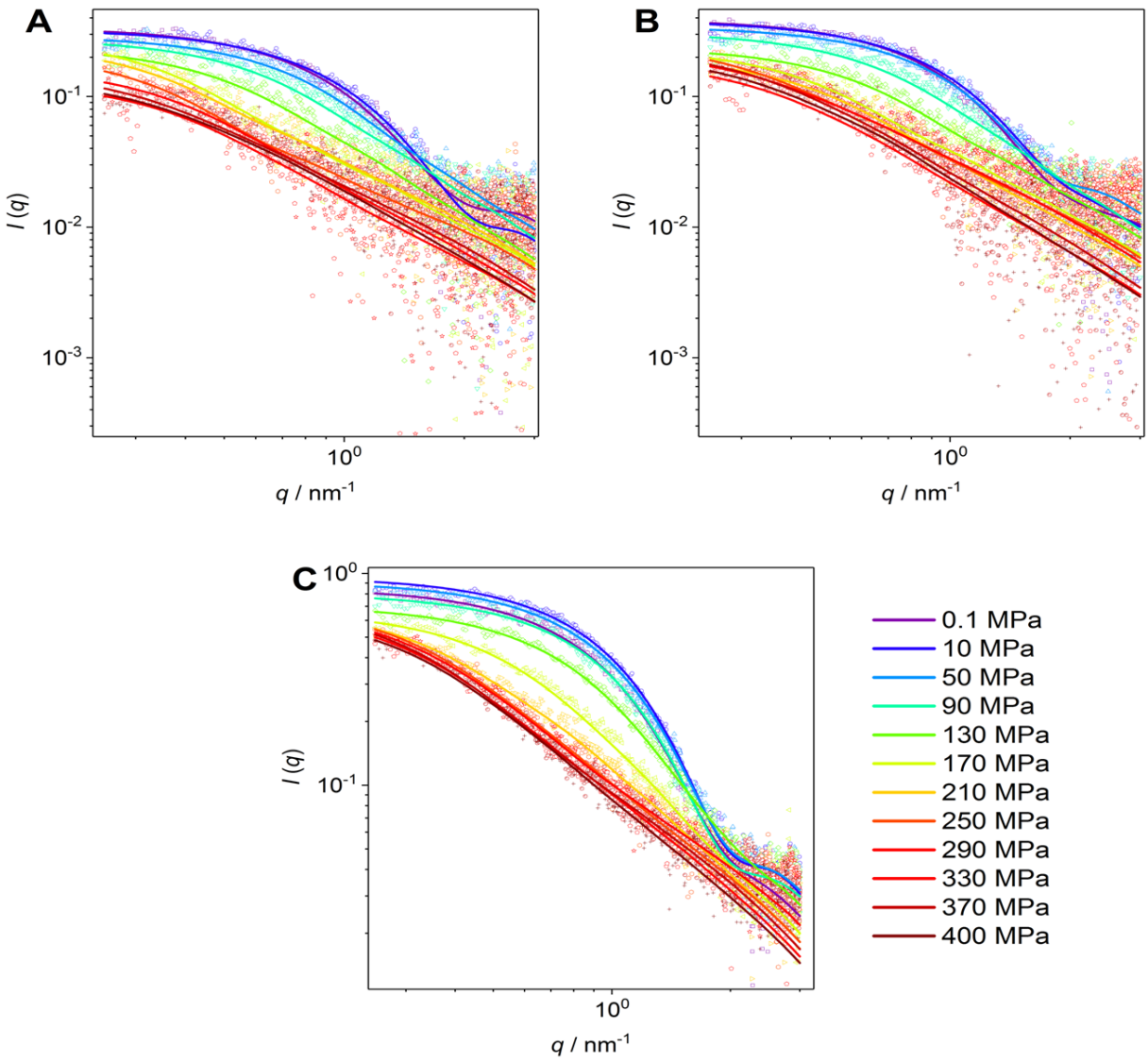

Figure A11. Scattering profiles in double logarithmic representations of 1wt% WT-PP32 in 20 mM Bis-Tris, pH 6.8, 5 mM DTT, 1.5 M urea, at 15°C (A) 20°C(B) and 30°C (C).

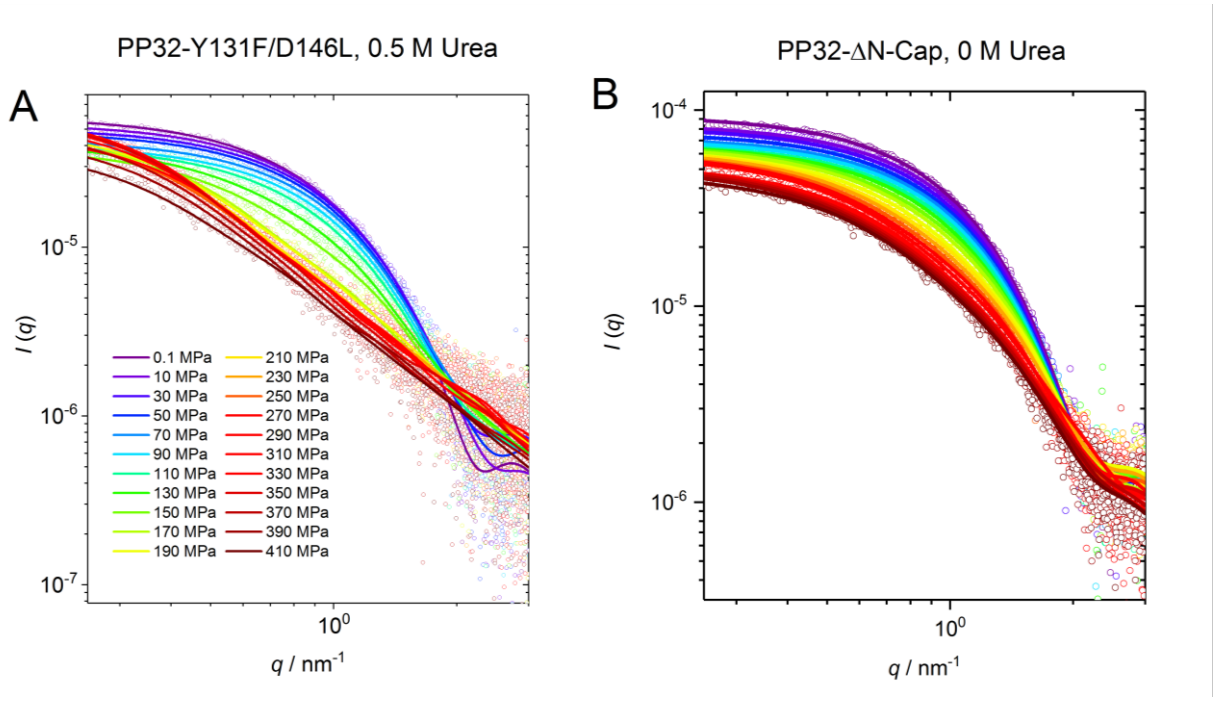

Figure A12. Scattering profiles in double logarithmic representations of PP32-Δ-NCap with 0 M urea (A) and PP32-Y131F/D146L with 0.5 M urea (B) at 20°C.

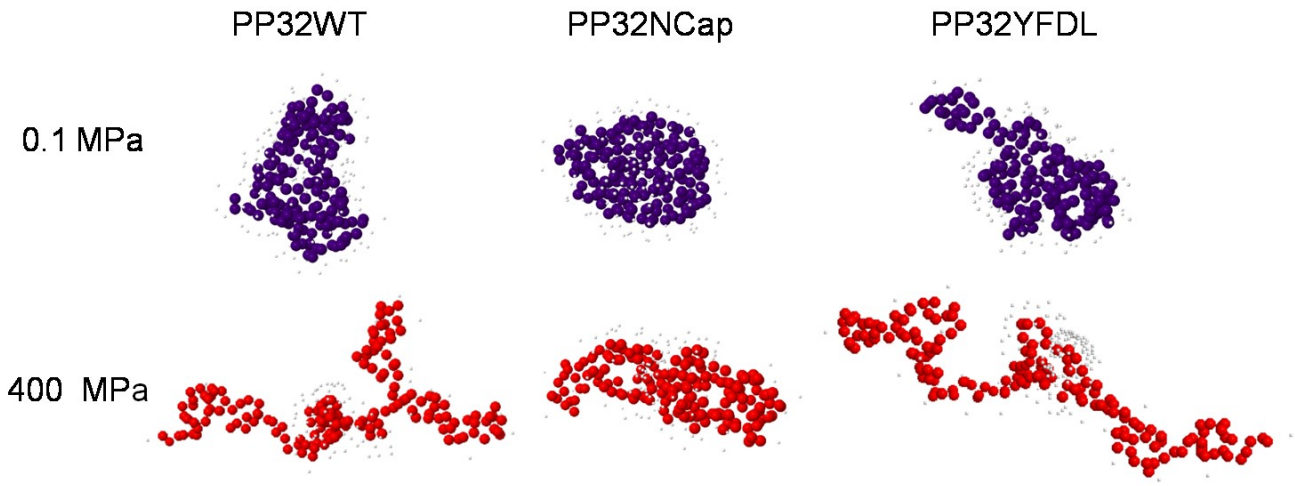

Figure A13. *Ab initio* reconstruction of the folded (top) and pressure-unfolded (bottom) PP32 variants.

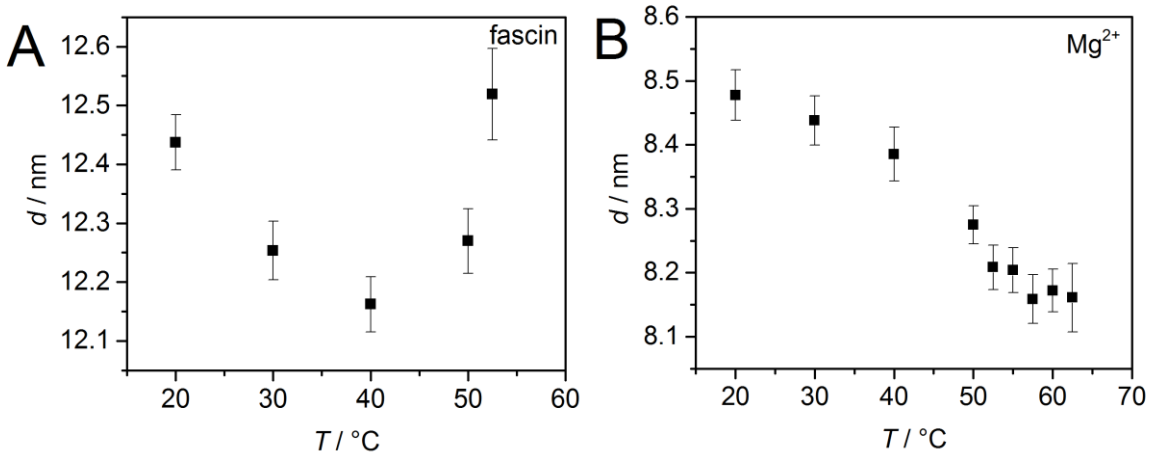

Figure A14. Temperature-dependent changes in the lattice constant, d, of B-actin. Bundling of F-actin was induced with fascin (A) or Mg^{2+} ions (B). Error bars are derived from the error in determining the peak maximum by Gaussian fits.

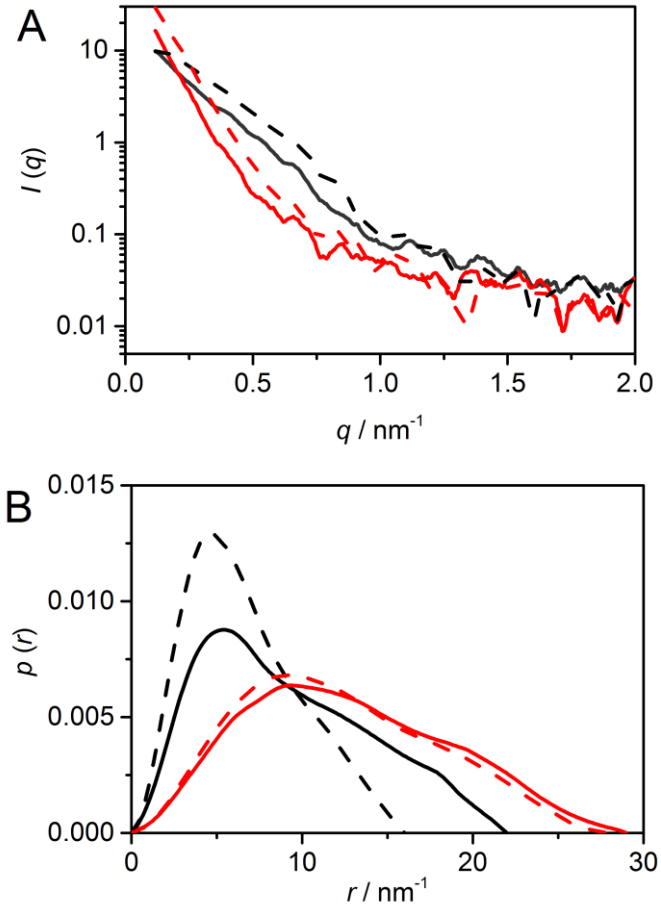

Figure A15. Comparison of the scattering intensity profiles (A) and pair-distance distribution functions, $P(r)$, (B) of fascin-induced F-actin bundles (solid line) and F-actin (dashed line) at 70°C (black curves) and 80°C (red curves).

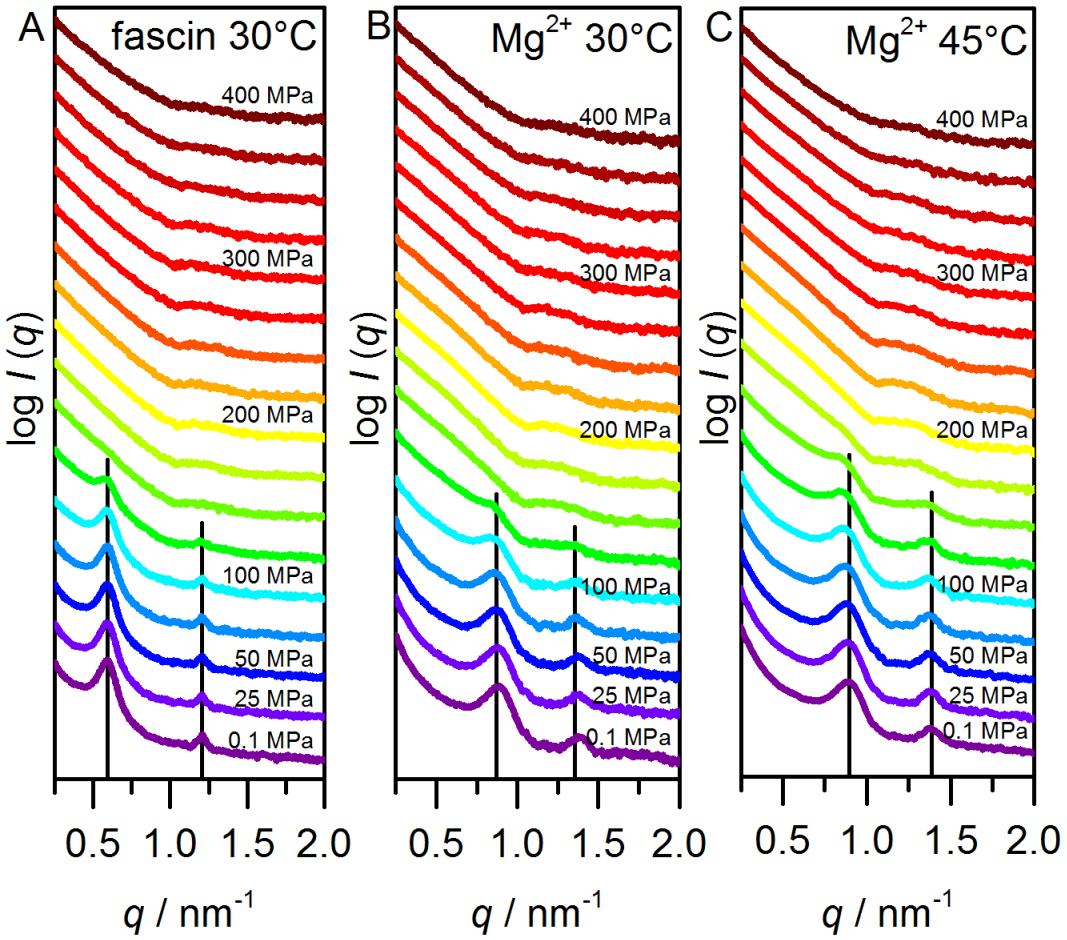

Figure A16. Pressure-dependent Synchrotron small angle x-ray scattering intensity profiles of B-actin at different temperatures. Bundling of F-actin was induced with fascin (A) or Mg^{2+} ions (B,C). The profiles were recorded at temperatures of 30°C (A,B) and 45°C (C). Black solid lines indicate the position of the peak maxima related to hexagonal packing of filaments at 0.1 MPa. Curves were shifted for clarity.

List of abbreviations

BL	*Beamline*
BME	*Bicontinuous microemulsion*
CCP	*Critical packaging parameter*
DA	*Decanoic Acid*
DELTA	*Dortmunder Elektronen-Speicherring-Anlage*
DLS	*Dynamic light scattering*
D_{max}	*Maximum dimension*
DNA	*Desoxyribonucleic acid*
DOH	*Decanol*
DPPC	*1,2-dipalmitoylphosphatidylcholine*
DSC	*Differential Scanning Calorimetry*
DTT	*Dithiothreitol*
EDP	*Electron density profiles*
ELP	Elastin-like peptide
ESRF	*European Synchrotron Radiation Facility*
FRET	*Förster resonance energy transfer*
FTIR	*Fourier Transform Infrared Spectroscopy*
GMP	*Guanosine monophosphate*
HHP	*High hydrostatic pressure*
HpRz	*Hairpin ribozyme*
IFT	*Indirect Fourier transformation*
ITT	*Inverse temperature transition*
LRR	*Leucine-rich repeats*
MD	*Molecular dynamic*
mRNA	*Messenger RNA*
NMR	*Nuclear Magnetic Resonance*
$P(r)$	*pair distance distribution function*
PAGE	*Polyacrylamide gel electrophoresis*
PEG	*Polyethylene glycol*
PP32	*Phosphoprotein 32*
Protein Data Bank	*Protein Data Bank*
PTFE	*Polytetrafluoroethylene (Teflon)*
R_g	*Radius of gyration*
RNA	*Ribonucleic acid*
rRNA	*Ribosomale RNA*
SANS	*Small-Angle Neutron Scattering*
SAXS	*Small-angle X-ray scattering*
sRNAh	*Small RNA hairpin*
TEM	*Transmission electron microscopy*
TFE	*Trifluoroethanol*
TMAO	*Trimethylamine oxide*
tRNA	*Transfer RNA*, *transfer ribonucleic acid*
WT	*wildtype*
XRR	*X-Ray Reflectivity*

List of figures

List of tables

Eidesstattliche Versicherung (Affidavit)

Name, Vorname
(Surname, first name)

Matrikel-Nr.
(Enrolment number)

Belehrung:

Wer vorsätzlich gegen eine die Täuschung über Prüfungsleistungen betreffende Regelung einer Hochschulprüfungsordnung verstößt, handelt ordnungswidrig. Die Ordnungswidrigkeit kann mit einer Geldbuße von bis zu 50.000,00 € geahndet werden. Zuständige Verwaltungsbehörde für die Verfolgung und Ahndung von Ordnungswidrigkeiten ist der Kanzler/die Kanzlerin der Technischen Universität Dortmund. Im Falle eines mehrfachen oder sonstigen schwerwiegenden Täuschungsversuches kann der Prüfling zudem exmatrikuliert werden, § 63 Abs. 5 Hochschulgesetz NRW.

Die Abgabe einer falschen Versicherung an Eides statt ist strafbar.

Wer vorsätzlich eine falsche Versicherung an Eides statt abgibt, kann mit einer Freiheitsstrafe bis zu drei Jahren oder mit Geldstrafe bestraft werden, § 156 StGB. Die fahrlässige Abgabe einer falschen Versicherung an Eides statt kann mit einer Freiheitsstrafe bis zu einem Jahr oder Geldstrafe bestraft werden, § 161 StGB.

Die oben stehende Belehrung habe ich zur Kenntnis genommen:

Official notification:

Any person who intentionally breaches any regulation of university examination regulations relating to deception in examination performance is acting improperly. This offence can be punished with a fine of up to EUR 50,000.00. The competent administrative authority for the pursuit and prosecution of offences of this type is the chancellor of the TU Dortmund University. In the case of multiple or other serious attempts at deception, the candidate can also be unenrolled, Section 63, paragraph 5 of the Universities Act of North Rhine-Westphalia.

The submission of a false affidavit is punishable.

Any person who intentionally submits a false affidavit can be punished with a prison sentence of up to three years or a fine, Section 156 of the Criminal Code. The negligent submission of a false affidavit can be punished with a prison sentence of up to one year or a fine, Section 161 of the Criminal Code.

I have taken note of the above official notification.

Ort, Datum
(Place, date)

Unterschrift
(Signature)

Titel der Dissertation:
(Title of the thesis):

Ich versichere hiermit an Eides statt, dass ich die vorliegende Dissertation mit dem Titel selbstständig und ohne unzulässige fremde Hilfe angefertigt habe. Ich habe keine anderen als die angegebenen Quellen und Hilfsmittel benutzt sowie wörtliche und sinngemäße Zitate kenntlich gemacht.
Die Arbeit hat in gegenwärtiger oder in einer anderen Fassung weder der TU Dortmund noch einer anderen Hochschule im Zusammenhang mit einer staatlichen oder akademischen Prüfung vorgelegen.

I hereby swear that I have completed the present dissertation independently and without inadmissible external support. I have not used any sources or tools other than those indicated and have identified literal and analogous quotations.

The thesis in its current version or another version has not been presented to the TU Dortmund University or another university in connection with a state or academic examination.*

*Please be aware that solely the German version of the affidavit ("Eidesstattliche Versicherung") for the PhD thesis is the official and legally binding version.

Ort, Datum
(Place, date)

Unterschrift
(Signature)